Reduced Complexity Detection for Massive MIMO-OFDM Wireless Communication Systems

Ali Al-Askery

Newcastle University

Newcastle upon Tyne, UK.

A thesis submitted for the degree of

Doctor of Philosophy

July 2017

To the memory of my beloved parents.

"Seek the knowledge from cradle to grave."

-Prophet Muhammad

"Life consists of two days, one for you and one against you. So when it is for you do not be proud or reckless, and when it is against you be patient, both days are test for you."

-Ali Ibn Abi Talib

Acknowledgements

In the name of Allah, the most Beneficent and the most Merciful.

I would like to start my acknowledgement by thanking the almighty Allah for giving me the strength and the courage to continue and to be on the right way. I would like to thank my parents for all the love and support they gave me during their life, I will never forget them.

I would like to thank my first supervisor Dr. Charalampos Tsimenidis, you were my role-model and mentor for the last four years. I have received from you all the required support and encouragement that build up my personality and shaped my views, thank you. I would like to thank my second supervisor Dr. Said Boussakta for his support. I would also like to thank my panel, Dr. Martin Johnston and Dr. Kianoush Nazarpour for all the support and the constructive advices.

I would like to express my appreciation to the Iraqi Government and the Iraqi Ministry of Higher Education and Scientific research for sponsoring my study in Newcastle University. I would also like to thank the School of Electrical and Electronic Engineering / Newcastle University for their assistance and support during my study and especially for Professor Jonathon Chambers the head of ComS2IP Group, Gill Webber the PGR coordinator and Deborah Alexander the reception & office systems coordinator.

I would also like to thank my brother Amer, and my sisters for all the support and love they gave me for the last 37 years of my life and especially during the last four years. I would like to thank my wife and my children for being the joy of my life. And finally, I would like to express my gratitude to all my friends and school mates.

Abstract

The aim of this thesis is to analyze the uplink massive multiple-input multiple-output with orthogonal frequency-division multiplexing (MIMO-OFDM) communication systems and to design a receiver that has improved performance with reduced complexity. First, a novel receiver is proposed for coded massive MIMO-OFDM systems utilizing log-likelihood ratios (LLRs) derived from complex ratio distributions to model the approximate effective noise (AEN) probability density function (PDF) at the output of a zero-forcing equalizer (ZFE). These LLRs are subsequently used to improve the performance of the decoding of low-density parity-check (LDPC) codes and turbo codes. The Neumann large matrix approximation is employed to simplify the matrix inversion in deriving the PDF.

To verify the PDF of the AEN, Monte-Carlo simulations are used to demonstrate the close-match fitting between the derived PDF and the experimentally obtained histogram of the noise in addition to the statistical tests and the independence verification. In addition, complexity analysis of the LLR obtained using the newly derived noise PDF is considered. The derived LLR can be time consuming when the number of receive antennas is very large in massive MIMO-OFDM systems. Thus, a reduced complexity approximation is introduced to this LLR using Newton's interpolation with different orders and the results are compared to exact simulations. Further simulation results over time-flat frequency selective multipath fading channels demonstrated improved performance over equivalent systems using the Gaussian approximation for the PDF of the noise.

By utilizing the PDF of the AEN, the PDF of the signal-to-noise ratio (SNR) is obtained. Then, the outage probability, the closed-form capacity and three approximate expressions for the channel capacity are derived based on that PDF. The system performance is further investigated by exploiting the PDF of the AEN to derive the bit error rate (BER) for the massive MIMO-OFDM

system with different M-ary modulations. Then, the pairwise error probability (PEP) is derived to obtain the upper-bounds for the convolutionally coded and turbo coded massive MIMO-OFDM systems for different code generators and receive antennas.

Furthermore, the effect of the fixed point data representation on the performance of the massive MIMO-OFDM systems is investigated using reduced detection implementations for MIMO detectors. The motivation for the fixed point analysis is the need for a reduced complexity detector to be implemented as an optimum massive MIMO detector with low precision. Different decomposition schemes are used to build the linear detector based on the IEEE 754 standard in addition to a user-defined precision for selected detectors. Simulations are used to demonstrate the behaviour of several matrix inversion schemes under reduced bit resolution. The numerical results demonstrate improved performance when using QR-factorization and pivoted LDLT decomposition schemes at reduced precision.

Contents

List of Figures

List of Tables

Nomenclature

Acronyms

AEN   Approximate Effective Noise

AWGN Additive White Gaussian Noise

BCJR Bahl, Cock, Jelenik, and Raviv

BER   Bit Error Rate

BI-STCM Bit-Interleaved Space-Time Coded Modulation

BICM Bit-Interleaved Coded Modulation

BPSK Binary Phase Shift-Keying

BS   Bas Station

CLT   Central Limit Theorem

CP   Cyclic Prefix

CSIT Channel State Information at the Transmitter

CWEF Conditional Weight Enumerating Function

DAC   Digital-to-Analog Converter

ECCs Error Correcting Codes

eIRA Extended Irregular Repeat-Accumulate

ELR   Element-Based Lattice Reduction

FEC   Forward Error Correcting

FFT   Fast Fourier Transform

FLOP   Floating Point Operation

FPGA   Field-Programmable Gate Array

GS   Gram-Schmidt

GSM   Global System for Mobile

HDL   Hardware Description Language

HWI   Hardware Impairment

IBI   Inter-Block Interference

IBP   Iterative Belief Propagation

IDFT   Inverse Discrete Fourier Transform

IFFT   Inverse Fast Fourier Transform

i.i.d   Independent and Identical distributed

IMD   Inter-modulation distortion

IMT-2000 Interference Mobile Telecommunication Standard 2000

IRWEF Input-Redundancy Weight Enumerating Function

KS   Kolmogorov-Smirnov

LAS   Local Ascent Search

LD   Linear Detector

LDPC   Low-Density Parity-Check

LLC   Link-Level Capacity

LLL   Lenstra,Lenstra and Lovasz

LLR   Log Likelihood Ratio

LML   Local Maximum Likelihood

LP   Linear Programming

LR   Lattice-Reduction

LTS   Layered Tabu Search

LTE   Long-Term Evolution

MAP   Maximum a Posteriori

MCMC Markov Chain Monte-Carlo

MGF   Moment Generating Function

MGS   Modified Gram-Schmidt

MIMO Multiple-Input Multiple-Output

MLD   Maximum Likelihood Detector

MMSE Minimum Mean Square Error

MSE   Mean Square Error

MU-MIMO Multi-User MIMO

NRNSC Non-Recursive Non-Systematic Code

NRSC Non-Recursive Systematic Code

OFDM Orthogonal Frequency-Division Multiplexing

PAPR Peak-to-Average Power Ratio

PAM   Pulse Amplitude Modulation

PCCC Parallel Concatenating Convolutional Code

PCEP Pilot Contamination Eliminating Procedure

PEP   Pairwise Error Probability

PDF   Probability Density Function

QAM   Quadrature Amplitude Modulation

QRD   QR-Decomposition

QRD-SIC QR Detector with Successive Interference Cancellation

RSC   Recursive Systematic Code

SC-FDMA Single-Carrier Frequency-Division Multiple Access

SD   Sphere Decoding

SER   Symbol Error Rate

SIC   Successive Interference Cancellation

SINR   Signal-to-Interference plus Noise Ratio

SM-MIMO Spatially Multiplexed MIMO

SNR   Signal to Noise Ratio

SOVA Soft Output Viterbi Algorithm

S/P   Serial to Parallel

SPA   Sum-Product Algorithm

TDL   Tapped Delay Line

V-BLAST Vertical-Bell Laboratories Layered Space-Time

VLSI Very Large Scale Integration

WiFi   Wireless Fidelity

WiMAX Worldwide Interoperability for Microwave Access

ZFE   Zero-Forcing Equalizer

List of Symbols

$c(\tau, t)$ The Impulse Response of the Tapped Delay Channel Model

$c_n(t)$ The Tab Weights of the Tapped Delay Channel Model

$C(f, t)$ The Transfer Function of the Tapped Delay Channel Model

$\delta(n)$ The Dirac Delta Function

W The Bandwidth of the Band Pass signal

$\mathbf{x}(t)$ The Received Signal in the Time Domain

ρ The Number of Multipath Taps

$\mathbf{s}(t)$ The Transmitted Signal in the Time Domain

$\mathbf{w}(t)$ The AWGN Signal in the Time Domain

T_c The Channel Coherence Time

f_d The Doppler Frequency

T_s The Symbol Duration Time

Δf_c The Channel Coherence Bandwidth

τ_{max} The Maximum Delay Spread of the channel

$p(x)$ The probability of x

σ_H^2 The Channel Variance

σ_w^2 The AWGN Variance

$\mathbf{H}$ The Channel Matrix

K The FFT Block Length

N_t The Number of Transmitting Antennas

N_r The Number of Receiving Antennas

$\hat{\mathbf{s}}$ The Estimation of $\mathbf{s}$

M The Modulation Index

I	In-phase
Q	Quadrature
$\mathbf{W}$	The MIMO Linear Equalizer of $\mathbf{H}$
$\mathbf{H}^H$	The Hermitian of Matrix $\mathbf{H}$
$\mathbf{H}^{-1}$	The Inverse of Matrix $\mathbf{H}$
$\mathbf{H}^\dagger$	The Pseudo-Inverse of Matrix $\mathbf{H}$
E_s	The Symbol Energy
E_b	The Bit Energy
$\mathbf{H}_{ex}$	The Extended Matrix of $\mathbf{H}$
N_0	The Noise Energy
$f(\mathbf{r}|\mathbf{a})$	The Likelihood Function of the Received Signal
$M_t(q)$	The Path Metric of the Trellis at Time t
$\mu_t(\mathbf{r}_t, \hat{\mathbf{a}}_t)$	The Branch Metric of the Trellis at Time t
$L(a_t|\mathbf{r})$	The A Priori LLRs of the Equalized Received Signal
$\beta_t(s)$	The Probability that the Trellis is in State s at Time t
$\gamma_t(s', s)$	The Probability of the State Transition from s' to s at Time t
$\alpha_{t-1}(s')$	The Probability that the Trellis is in state s' at Time $t-1$
v_t	The Decision on the Decoded Bits
$\log_e(x)$	The Natural Logarithm of x
R	The Coding Rate
Λ_t^x	The A Priori Information to the x Decoder, and $x = 1, 2$
E_t^x	The Extrinsic Information for the x Decoder, and $x = 1, 2$
$\Pi(\mathbf{x})$	The Interleaving of Vector $\mathbf{x}$
$\mathbf{H}_p$	The Parity Check Matrix of the LDPC codes
$\mathbf{G}_p$	The Generator Matrix of the LDPC codes
K_{cp}	The Length of the Cyclic Prefix
$\mathbf{G}_k$	The Symmetric Gram Matrix
$\psi_\zeta(w)$	The Characteristic Function of ζ
$\{\cdot\}^\nu$	Superscript that Indicates the In-phase I or the Quadrature Q Part
α^ν	The Noise After the ZFE

N_x The Order of the Newton's Polynomial

P_e^{BPSK} The BER for the BPSK Modulation

P_e^{M-QAM} The BER for the $M-QAM$ Scheme

$P_s^{\sqrt{M}-PAM}$ The SER for the $\sqrt{M}-PAM$ Scheme

P_s^{M-QAM} The SER for the $M-QAM$ Scheme

$\gamma_{l,k}$ The instantaneous SNR of the Received Signal

P_{out} The Outage Probability

$\Gamma(N)$ The Complete Gamma Function of N

C The Channel Capacity

$\psi(N)$ The Psi Function ($\frac{d}{dx}\log_e(\Gamma(N))$)

$P_{s_1 \to s_2}$ The Pairwise Error Probability

P_b The Upper-Bound of the Coded Systems

N_π The Interleaver Length

c_d The Sum of the Error Events for the Convolutional Codes

$\binom{N}{w}$ The Binomial Distribution of N and w

Chapter 1

Introduction

Over the recent decades, the demands for high data throughput and transmission reliability are increased rapidly to keep up with the growth in the technology inventions. The 3G, 4G and the later generations of wireless communication systems are examples of the development in this direction. One of the main challenges for the mobile communication systems is to provide the required technology that supports multimedia transmission with high data rate. Multiple-input multiple-output (MIMO) wireless communication technology can provide an increase in the data transmission and signal reliability depending on the mode of transmission and the number of receive and transmit antennas. This technique has the ability to provide spatial diversity gain, interference reduction, array gain and multiplexing gain [1].

In addition, orthogonal frequency-division multiplexing (OFDM) is a multi-carrier technology with immunity to the channel's frequency selectivity, which can transmit data over a large number of sub-carriers rather than a single carrier transmission [2, 3]. By combining these techniques into the MIMO-OFDM system, the resulted system is known for its improved data throughput and its immunity to the multi-path channel fading. In this system, a sequence of data blocks is first modulated using OFDM technology, divided into parallel sub-blocks, transmitted and received via multiple antenna systems [4].

The early generations of mobile systems were able to provide acceptable quality voice calls in addition to text messaging. While the 3G/4G wireless communication systems offer a wide range of recent applications such as high-quality voice and video calls, surfing the web, downloading large files at high speed and much more applications. To achieve the requirements for the latest wireless communication generations, more advanced technologies are required to support the increase in the speed and the capacity of transmission.

Massive MIMO-OFDM systems are known for its improved performance compared to the conventional MIMO systems. The term massive MIMO-OFDM is used to describe the high number of transmitting/receiving antennas in order to provide the required transmission performance. By increasing the number of received/transmitted elements, the stated gains will be improved significantly as the number of the elements increased.

This implies an additional complexity for the receiver to detect the transmitted signals. The complexity and the performance of the MIMO detector vary from one detector to another. The linear detectors such as the zero-forcing equalizer (ZFE) and the minimum mean-square error (MMSE) detectors have a reduced complexity detection compared to the non-linear maximum likelihood detector (MLD), which has a complexity that increases exponentially with the number of transmitters and the modulation index. However, the performance of the linear detectors are limited and much less than the non-linear MLDs. Other detection schemes such as successive-interference cancellation (SIC), sphere decoding (SD) and the likelihood ascent search (LAS) based detectors, are proposed to achieve better performance detection with reduced complexity [5, 6].

In the next section, a literature review is provided to cover the main challenges and applications of the massive MIMO-OFDM systems.

Notation Matrices and vectors are denoted by upper-case and lower-case boldface characters, respectively. The Hermitian transpose of a matrix $\mathbf{A}$ and its pseudo-inverse are denoted by $\mathbf{A}^H$ and $\mathbf{A}^\dagger$, respectively. $\Gamma(a)$ and $\Gamma(a, b)$ are the complete and the incomplete gamma function of the variables a and b. Finally, σ_w^2 and σ_H^2 are the noise and the channel variances, respectively.

1.1 Literature Review

Recently, the limitations in the performance of the traditional communication systems have encouraged the researchers to go massively in the design of the modern wireless communication systems. Several challenges have emerged as a result of the size increase such as the receiver complexity, channel correlation, pilot contamination and hardware impairments [7]. This section is subdivided to cover some of the challenges in literature researches.

1.1.1 Receiver Design and Performance Evaluation

In [8], two SDs have been proposed to achieve the optimal performance of the MLD with a reduced complexity design. The accurate selection of the initial sphere radius has proven to achieve the MLD performance. In addition, the mathematical analysis for the designed receiver is obtained and compared to Monte-Carlo simulations. A reduced complexity approach is proposed in [9] that are based on the local search algorithm. This approach utilized the layered local neighborhood search to design low complexity layered Tabu search (LTS) MIMO detector. The performance of the proposed system approaches the MLDs and it is designed to work with the massive MIMO systems. In addition, the authors have proposed a reduced complexity lower bound on the performance of the MLDs which tends to be very tight at a moderate to high SNR.

A LAS detector has been proposed in [10] as a low complexity massive MIMO detector by generating multiple solutions to the output and selecting one of them that has the best performance. The generation of the solutions has two possibilities, either randomly selected to have the lowest local maximum likelihood (LML) point with the lowest metric, or by using the linear detector to generate the first string of data then generate multiple solutions using MMSE-LAS algorithm. The simulations suggest that the proposed detector has better performance compared to the conventional LAS algorithms. A soft Heuristic detectors are proposed in [11] for large-MIMO detection to obtain the optimal performance with reduced complexity in three stages. The first stage is to use the ML decision on specific bits, followed by soft calculations for the rest of the bits and finally, the soft calculations are used in a heuristic algorithm to detect these bits. Two heuristic algorithms are introduced in this paper that has different complexity and performance.

Reducing the complexity of detection can also be obtained by utilizing the lattice-reduction (LR) algorithms in the MIMO detectors for higher quadrature amplitude modulation (QAM) constellations. In [12], an element-based LR (ELR) algorithm is proposed to enhance the asymptotic performance of the linear detectors which reduces the diagonal elements of the noise covariance matrix. This sub-optimal detector is claimed to achieve better performance compared to other reduced complexity approaches while maintaining lower complexity. The K-Best detector is combined with the ELR in [13] to improve the BER performance and to reduce the complexity. This algorithm claims to achieve 2 dB improvement for the massive MIMO system that has an equal dimension of 200 antennas at BER $= 10^{-5}$ compared to the Lenstra, Lenstra, and Lovasz (LLL) algorithm. In [14],

a transceiver has been designed for the massive MIMO communication systems based on Krylov sub-space receiver with a linear precoder. The precoder is designed to improve the performance of the Krylov subspace detector at high SNR. This transceiver has shown to have better performance compared to other precoded massive MIMO communication systems.

A reduced complexity detection receiver is proposed in [15] based on Richardson method to replace the matrix inversion required using MMSE channel equalization. The new detector claims to reduce the complexity of detection from $O(K^3)$ to $O(K^2)$, where K represents the number of users. Two sub-optimal reduced complexity massive MIMO detectors are proposed in [16] in which, the first detector was based on Markov chain Monte-Carlo (MCMC) algorithm and the second algorithm was based on random local neighborhood search. Both detectors are tested on massive MIMO communication systems with size 16×16, 32×32, 64×64 and 4-QAM scheme. The simulation results have shown to have improved performance compared to other sub-optimal detectors.

1.1.2 Hardware Implementation and Hardware Impairments

Based on Neumann matrix inversion method, the authors in [17] have proposed sub-optimal implementation to the matrix inversion that is used to detect the data at the receiver using Virtex-7 field-programmable gate array (FPGA). These results are further analyzed in [18] and based on Cholesky decomposition, an exact matrix inversion is proposed and implemented using Virtex-7 FPGA. The performance and complexity of the selected system are compared to [17] and the results have shown that the proposed implementation have better performance and lower implementation complexity. In [19], another massive MIMO single-carrier frequency-division multiple access (SC-FDMA) is proposed based on Neumann matrix inversion. The corresponding very-large-scale integration (VLSI) is presented using Virtex-7 FPGA that utilizes the exact and the approximate soft detection with different MIMO sizes.

The impact of the hardware impairments is considered in [20] such that, a multi-user massive MIMO (MU-MIMO) system is analyzed in simulation and theory. The effect of the mutual coupling on the power amplifier distortion has been analyzed and simulated. In addition, a novel dithering method that improves the link quality and reduces the bit representation per transmitter is proposed utilizing the null-space of the channel in the massive MIMO systems. On the hardware impairment in full-duplex relaying massive

MIMO systems is considered in [21] with a distorted noise model for the transmitter and the receiver. A reduced complexity transceiver is proposed to avoid the hardware impairments utilizing the antenna arrays and the channel statistical knowledge to reduce the noise distortion.

In addition to the performance investigation of the massive MIMO communication systems, the hardware impairment is also investigated in [22] with relationships that connect the performance to the number of antennas/users, transmit power and the hardware impairments. The effect of hardware impairment on the distributed massive MIMO cellular system is investigated in [23] with maximum ratio transmission and downlink mode of transmission. The authors have discussed the asymptotic behavior of the derived closed-form expressions for the spectral efficiency with respect to the increase in the number of antennas.

The effect of imperfect channel information on the performance of the multi-user massive MIMO systems is considered in [24] with downlink mode. First, the authors have compared the performance of different precoded systems assuming perfect channel state information at the transmitter (CSIT) with the performance of imperfect CSIT. Second, the effect of hardware impairment and the erroneous channel estimation are studied with different linear precoding techniques. Based on the residual hardware impairment (HWIs) at the transmitter and the receiver, an HWI aware MMSE precoder is proposed in [25] for the uplink/downlink single-cell massive MIMO system. In addition, an asymptotic expression for the power allocation has been derived in the downlink mode that depends on the CSI only. Simulation results revealed that when the base station (BS) is equipped with a massive number of antenna elements, the proposed MMSE precoder achieves better performance than the ZF precoded system.

1.1.3 Pilot Contamination

As being part of the massive MIMO communication system challenges, channel estimation and pilot contamination are considered as a hot topic for the researchers to analyze and propose solutions for these challenges. An uplink training to downlink pilot contamination eliminating procedure (PCEP) is designed in [26] for the multi-cell massive MIMO systems. During the training uplink duration, the users that share the same cell use the same pilots which are orthogonal to other cell users. The downlink channels are estimated in the BS utilizing the uplink pilots and time-division duplex operation. In addition, the

performance of the proposed system is analyzed and tested with a selected BS size.

A location-aided method is proposed in [27] to reduce the impact of pilot contamination on the performance of the massive MIMO systems in the uplink mode of transmission. This method achieves good estimation to the channel parameters by utilizing the location of the BS, the users, and the scatters without the necessity of estimating large covariance matrices. In [28], an efficient and reduced complexity MMSE algorithm is proposed to estimate the channel parameters utilizing the correlation between the antennas. Stochastic geometry is used to estimate the pilot contamination and to examine the impact of the pilot contamination on the channel estimation.

In [29], to reduce the effect of pilot contamination on the signal-to-interference and noise ratio (SINR) in the multi-cell massive MIMO system, a simple space-time block code is used with a formulated optimization that maximizes the downlink SINR for the specified user. Simulation and results have confirmed that the proposed scheme can reduce the SINR degradation in the downlink mode. Pilot contamination mitigation techniques are investigated in [30] for multi-user massive MIMO communication systems with inter-user-interference and non-ideal hardware.

1.2 Contributions

The aim of this thesis is to investigate the performance of the massive MIMO-OFDM systems and to design a reduced complexity receiver for coded systems. Different detectors can be used to equalize the received signals of the massive MIMO systems. However, the complexity and the performance of each detector are unique and varies based on the system size and the application required. Both coded and uncoded massive MIMO-OFDM systems are investigated here and the contributions can be summarized as,

1. The noise PDF for the ZF equalized Massive MIMO-OFDM systems is derived using Neumann matrix approximation method. The derived PDF is subsequently utilized in the LLR calculations to improve the performance of different coded systems such as LDPC coded and turbo coded massive MIMO-OFDM systems. In addition, Estimating the complexity required for using the LLR equation based on the approximate effective noise PDF, and a reduced complexity approximation is introduced for this LLR using Newton polynomial interpolation. The performance of turbo coded and LDPC coded massive MIMO-OFDM systems using the Gaussian

LLR is compared to the approximate effective noise PDF based LLR, and different approximations that are obtained based on Newton interpolation method.

2. Obtaining the PDF of the SNR after the ZFE, which is utilized to derive the outage probability, the average capacity, and three bounds for the capacity at low and high SNR, respectively. In addition, deriving the BER for the massive MIMO-OFDM systems with frequency-selective Rayleigh fading channels and ZFE for different M-ary modulations. The pairwise error probability (PEP) is derived for the massive MIMO-OFDM systems, which is used to evaluate the upper-bounds of the convolutionally coded and turbo coded systems.

3. Different decomposition schemes are used in the detection of the massive MIMO-OFDM systems with fixed-point arithmetic to simulate the hardware implementation. The standard IEEE 754 double and half precision with word length of 64 and 16 bits are used in the simulations in addition to a user-defined precision of 12 and 10 bits to verify the ability of each detector, and the complexity required by each detector is estimated and tabulated.

1.3   Publications Arising From This Research

1. **Ali J. Al-Askery**, Charalampos C. Tsimenidis, Said Boussakta and Jonathon A. Chambers, "Performance Analysis of Coded Massive MIMO-OFDM Systems Using Effective Matrix Inversion," submitted to IEEE Trans. Commun. 2017.

2. **Ali J. Al-Askery**, Charalampos C. Tsimenidis, Said Boussakta and Jonathon A. Chambers, "Improved coded massive MIMO OFDM detection using LLRs derived from complex ratio distributions," in *Proc. IEEE 20th Int. Workshop Comput. -Aided Modelling. Design of commun. Links Netw. (CAMAD)*, Guildford, 2015, pp. 64-68.

3. **Ali J. Al-Askery**, Charalampos C. Tsimenidis and Said Boussakta, "Fixed-point arithmetic detectors for massive MIMO-OFDM systems," in *Proc. 23rd Europ. Signal Process. Conf. (EUSIPCO)*, Nice, 2015, pp. 919-923.

4. **Ali J. Al-Askery**, Charalampos C. Tsimenidis and Said Boussakta, "Shannon Capacity and Outage Probability for Massive MIMO-OFDM systems," submitted to IEEE Commun. Letters 2017.

1.4 Thesis Outline

This thesis is organized as follows:

Chapter 2 presents general preliminaries including, channel model, OFDM and different MIMO detectors. It also outlines the forward error correcting codes and describes different types of channel coding techniques such as the convolutional codes, turbo codes and LDPC codes.

Chapter 3 is the first contribution chapter that includes the derivation of the effective noise PDF after the ZFE, comparing the performance of different coded systems using the new LLR and the Gaussian based LLR, estimating the complexity of the new PDF and its LLR and proposing a reduced complexity formula for this LLR.

Chapter 4 provides analysis to the system performance such that the outage probability, the channel capacity and the PDF of the SNR after the ZFE are derived utilizing the noise PDF presented in Chapter 3. In addition, the theoretical BER for different M-QAM scheme are derived and compared to the Monte-Carlo simulations for different MIMO configurations. Furthermore, an upper bound on the performance of the convolutionally coded and turbo coded massive MIMO-OFDM systems are derived and verified with the simulations of different code generators and MIMO configurations.

Chapter 5 focuses on the effect of the fixed-point representation on the performance of different massive MIMO detectors. The performance of iterative ZFE, Gram matrix based detector utilizing different decomposition techniques and the QR detector with successive interference cancellation (QRD-SIC) are investigated at different IEEE 754 fixed point representations. In addition, Neumann based detectors are investigated under similar circumstances and the results are presented in comparison to the other detectors.

The conclusions are drawn in Chapter 6 and this thesis ends with a possible line of future work.

Chapter 2

Preliminaries: Channel Model, Orthogonal Frequency-Division Multiplexing, MIMO Equalization and Forward Error Correcting Codes

2.1 Introduction

The aim of this chapter is to review briefly the main parts of the communication system that is involved in this work. The frequency-selective Rayleigh fading channel model is illustrated in Section 2.2. While Section 2.3 describes the multicarrier OFDM technique that is utilized to eliminate the frequency selectivity of the channel. The focus of Section 2.4 is to demonstrate the linear and nonlinear MIMO equalization techniques that are used to equalize the channel effect. Finally, the FECCs are described in Section 2.5 for different coding techniques including the convolutional codes, turbo codes and LDPC codes.

2.2 Channel Model

The channel model of the system under consideration here is assumed to be a time-flat, uncorrelated, frequency-selective, Rayleigh fading channels. This channel can be described using the tapped delay line (TDL) model as shown in Fig. 2.2. The tap weights $c_n(t)$ of the model are complex random variables with Rayleigh distributed magnitudes, while the tap spacing is normally distributed [31]. The impulse response of this channel can be written as

$$c(\tau, t) = \sum_{n=-\infty}^{\infty} c_n(t)\delta(\tau - \frac{n}{W}), \tag{2.1}$$

and its transfer function can be written as

$$C(f, t) = \sum_{n=-\infty}^{\infty} c_n(t)\exp(-j2\pi fn/W), \tag{2.2}$$

where W is the bandwidth of the band-pass signal. Consequently, the signal that is received from a frequency-selective channel in the presence of the noise can be written as

$$x(t) = \sum_{n=0}^{\rho} c_n(t)s(t - \frac{n}{W}) + w(t), \tag{2.3}$$

where, ρ, $s(t)$ and $w(t)$ are the number of multipath taps of the channel, the low-pass signal and the additive white Gaussian noise (AWGN), respectively.

During the signal transmission, the channel impulse response remains constant for a specific time interval that is known as the channel coherence time $T_c \propto \frac{1}{f_d}$, where T_c is the channel coherence time and f_d is Doppler frequency [32]. The channel is considered
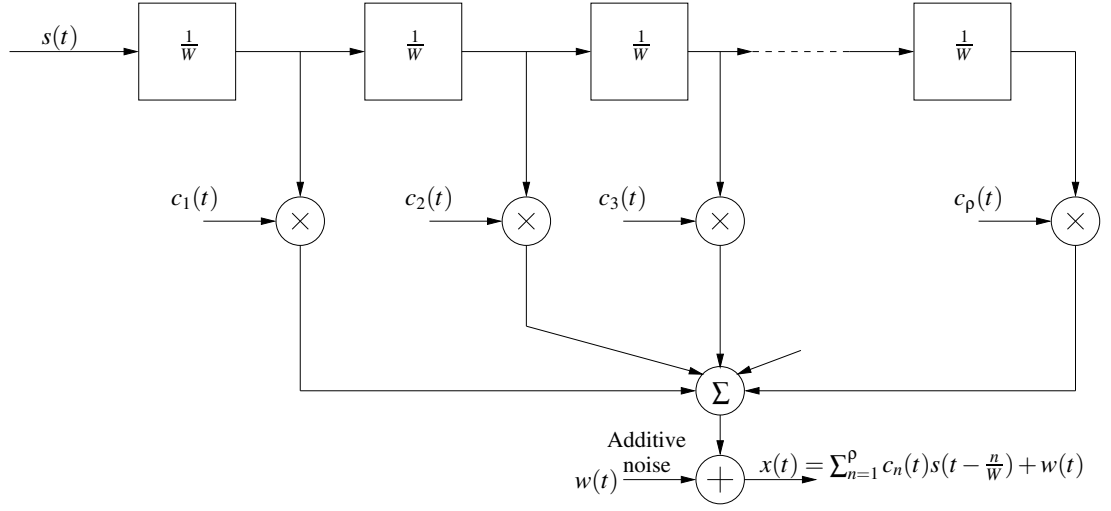
Figure 2.1: Tapped delay line channel model [31].

to have slow fading when the channel coherence time T_c is larger than the symbol time duration T_s, while it is considered to be fast when $T_c < T_s$.

The channel coherence bandwidth Δf_c is defined as the frequency range that has correlated fading process and it is related to the maximum delay spread of the channel such that

$$\Delta f_c \propto \frac{1}{\tau_{max}}, \tag{2.4}$$

where τ_{max} is the maximum delay spread of the channel. The channel fading is considered flat fading if the coherence bandwidth is larger than the signal bandwidth that is, $\Delta f_c >> W$ as in the case of narrow-band systems. On the other hand, the channel is considered as a frequency-selective fading when $\Delta f_c << W$, which is the case of wide-band systems [32].

The probability density function (PDF) of Rayleigh fading channels can be written as

$$p(h) = \frac{h}{\sigma_h^2} \exp\left(\frac{-h^2}{2\sigma_h^2}\right), \qquad h > 0, \tag{2.5}$$

where h is the channel coefficients and σ_h^2 is the channel variance.

2.3 Orthogonal Frequency-Division Multiplexing (OFDM)

One of the challenges to the single carrier transmission is the inter-symbol interference (ISI) that induced due to the channel delay spread τ_{max} being larger than the symbol duration T_{max}. The basic idea of the OFDM scheme is to transmit the data over K subcarriers,

(a) Single Carrier.
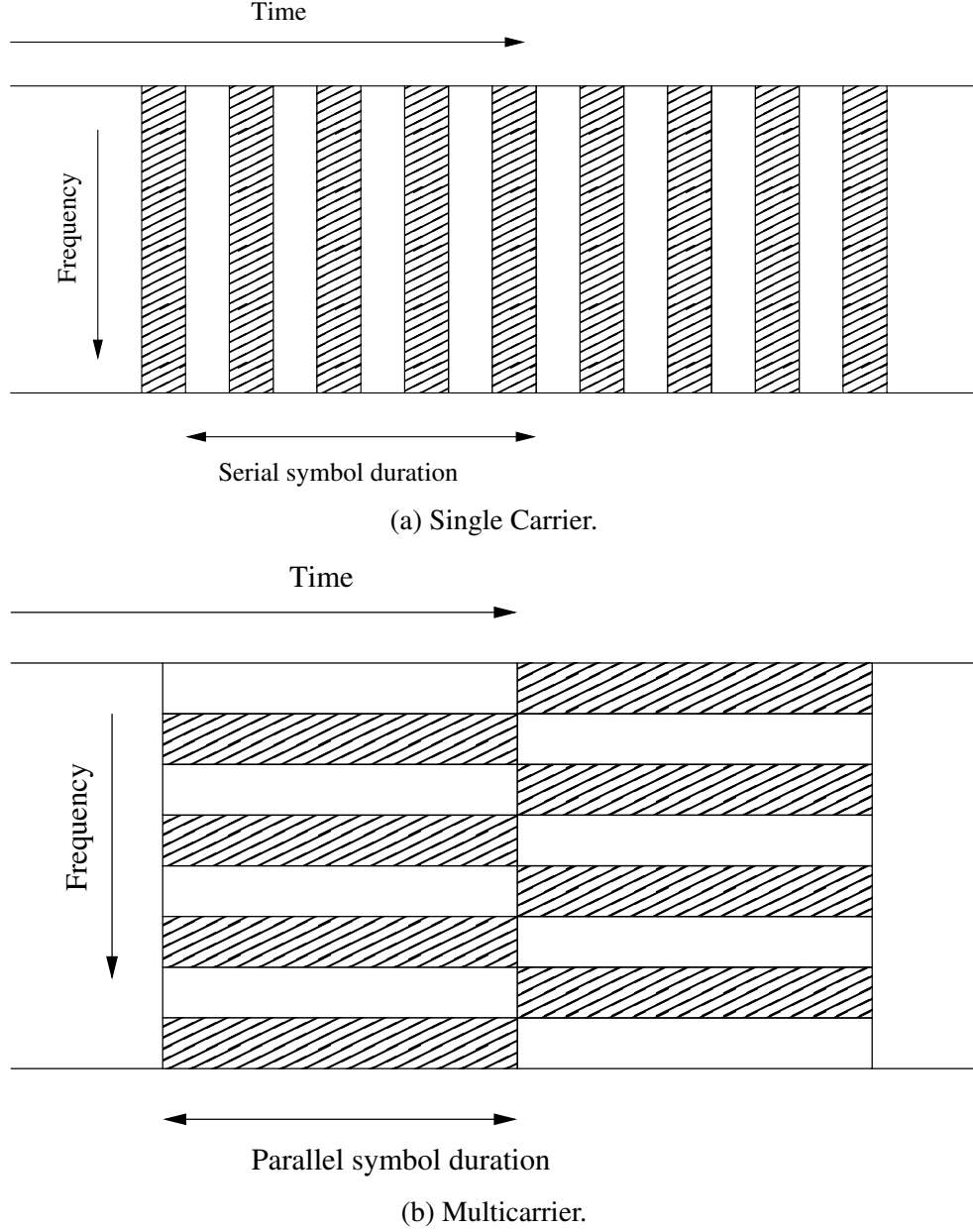
(b) Multicarrier.

Figure 2.2: The multicarrier concept [33].

each has a bandwidth B/K as shown in Fig. 2.2 b).

OFDM is a type of multicarrier transmission that involves modulating the data with an inverse fast Fourier transform (IFFT) at the transmitter and demodulating the received data with fast Fourier transform (FFT) at the receiver as depicted in Fig. 2.3. First, the serial to parallel (S/P) block divides the data stream into K parallel symbols, followed by IFFT or inverse discrete Fourier transform (IDFT) for each symbol such that

$$s_l(t) = \frac{1}{\sqrt{K}} \sum_{k=0}^{K-1} d_{k,l} e^{j2\pi kt/K}, \tag{2.6}$$

where $s_l(t)$ is the time domain of $d_{k,l}$ at l-th symbol, and $l = 1, 2, \ldots, L$. Subsequently, a
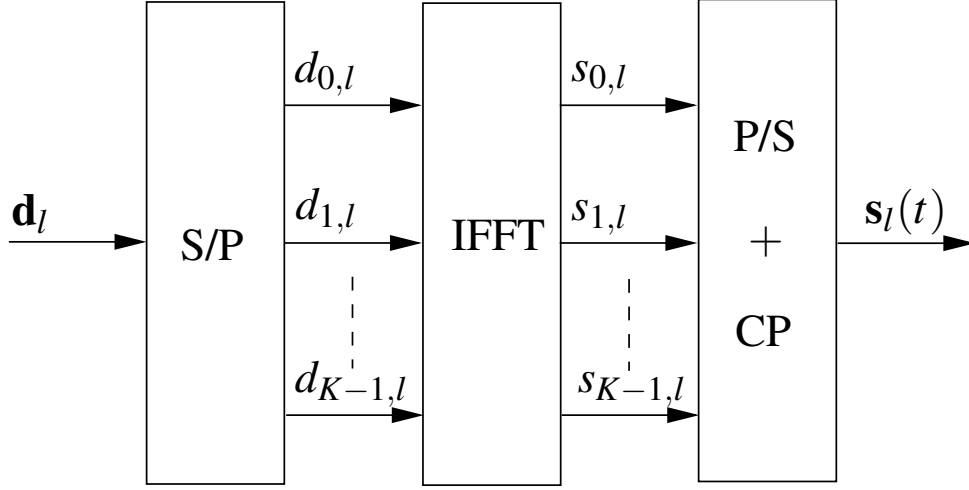
Figure 2.3: Block diagram for multicarrier modulation.

cyclic prefix (CP) is appended to the beginning of each block to maintain the cyclic effect of the FFT and to avoid the inter-block interference (IBI) induced by the multipath fading channels. The complex baseband samples to be transmitted are given as

$$s_l(t) = [s_{K-K_{cp}}, \ldots, s_{k-1}, s_0, \ldots, s_{K-1}]^T , \qquad (2.7)$$

where, K_{cp} is the length of the CP and is typically selected to cover the multipath delay spread.

To demodulate the received signal, the CP is removed first, followed by FFT or DFT transform to the received signal such that

$$d_{l,k} = \frac{1}{\sqrt{K}} \sum_{t=0}^{K-1} s_l(t) e^{-j2\pi kt/K}. \qquad (2.8)$$

The FFT based OFDM implementation is a computationally efficient algorithm compared to the DFT based implementation, especially for $K > 32$ points [31]. The majority of the modern wireless standards such as wireless fidelity (WiFi), long-term evolution, (LTE) and worldwide interoperability for microwave access (WiMAX) employed the OFDM modulation for its immunity towards the frequency selectivity of the fading channels [34, 35].

One of the OFDM modulation challenges is the peak-to-average power ratio (PAPR) of the transmitted time domain signal as a result of the constructive addition of multiple subchannels with the same phase [31]. Mathematically, the PAPR represents the ratio of

the maximum transmitted power to the average transmitted power such that

$$PAPR = \frac{Max[\mathbf{s}_l(t)\mathbf{s}_l^*(t)]}{E\{\mathbf{s}_l(t)\mathbf{s}_l^*(t)\}}. \tag{2.9}$$

The large peaks in the transmitted signal may result in an inter-modulation distortion (IMD) due to the power amplifier being saturated, or clipping the signal in the digital-to-analog converter (DAC). Different techniques have been used to eliminate the effect of the PAPR on the transmitted signal, such as the selective mapping [36], partial transmit sequence [37], clipping and filtering [38] and many other techniques.

2.4 MIMO Detectors

One of the objectives of this chapter is to describe some of the commonly used MIMO detectors for the spatially multiplexed MIMO (SM-MIMO) systems in the uplink mode of transmission. The MIMO system under consideration consists of N_t transmit antennas and N_r receive antennas such that $N_t < N_r$. The flat-fading channel matrix has the form, $\mathbf{H} \in \mathbb{C}^{N_r \times N_t}$ and the received signal $\mathbf{x} \in \mathbb{C}^{N_r \times 1}$ can be written as

$$\mathbf{x} = \mathbf{Hs} + \mathbf{w}, \tag{2.10}$$

where $\mathbf{w} \in \mathbb{C}^{N_r \times 1}$ is the AWGN vector, and $\mathbf{s} \in \mathbb{C}^{N_t \times 1}$ is the transmitted signal.

2.4.1 Maximum Likelihood (ML) Detector

MLDs are the optimum equalizers for the MIMO communication systems. The MLD minimizes the Euclidean distance of the noise such that [5, 31, 39]

$$\hat{\mathbf{s}} = \arg\min_{\mathbf{s} \in \mathbf{s}^M} ||\mathbf{x} - \mathbf{Hs}||^2, \tag{2.11}$$

where $\hat{\mathbf{s}}$ is the estimation of the transmitted vector at the receiver and $\mathbf{s} \in \mathbf{s}^M$ refers to the search over the candidate vectors of $\mathbf{s}^M$. This search has an extremely high complexity that varies exponentially with the constellation size M and the number of transmitters N_t [5, 39]. Similar detectors have been invented that gives the performance of the MLD such as the sphere decoding but its complexity remains high for large N_t [39].

2.4.2   Linear Detectors

Linear detectors (LDs) for MIMO systems are considered to equalize the received signals with a reduced complexity detection. These detectors reverse the channel effect and filter the received signals to estimate the transmitted signals such that

$$\hat{\mathbf{s}} = \mathbf{W}\mathbf{x}, \tag{2.12}$$

where $\mathbf{W} = \mathbf{H}^{-1}$ is the inverse or pseudo-inverse of the channel matrix. There are mainly two types of these detectors; the ZF detectors and the MMSE detectors.

2.4.2.1   Zero Forcing (ZF) Detectors

These detectors can be obtained by applying the Moore-Penrose pseudo-inverse on the channel matrix $\mathbf{H}$ for $N_r > N_t$ such that

$$\mathbf{W}_{ZF} = (\mathbf{H}^H\mathbf{H})^{-1}\mathbf{H}^H . \tag{2.13}$$

However, when $N_t = N_r$, the ZF detector is obtained using the standard matrix inversion methods. The disadvantage of using the ZF detectors is the noise enhancement at the output of this detector [5, 31, 39, 6]. MMSE detectors are used to reduce this noise enhancement as will be illustrated in the next section.

2.4.2.2   Minimum Mean-Square Error (MMSE) Detectors

The aim of this detector is to reduce the effect of the noise in the MIMO detectors by minimizing the mean-square error formula

$$\mathbf{W}_{MMSE} = \arg \min_W E[||\mathbf{s} - \mathbf{W}^H\mathbf{x}||^2]. \tag{2.14}$$

The optimization solution of this formula requires the statistical information of the noise σ^2 and can be written as [5, 31]

- if $N_r \geq N_t$

$$\mathbf{H}^{-1} = (\mathbf{H}^H\mathbf{H} + \frac{\sigma^2}{E_s}\mathbf{I}_{N_t})^{-1}\mathbf{H}^H, \tag{2.15}$$

- if $N_r < N_t$

$$\mathbf{H}^{-1} = \mathbf{H}^H(\mathbf{H}\mathbf{H}^H + \frac{\sigma^2}{E_s}\mathbf{I}_{N_r})^{-1}. \tag{2.16}$$

The MMSE detectors have improved performance compared to the ZF detectors at low to moderate SNR values, however, at high SNR, both detectors exhibit similar performance.

2.4.3 Sucessive-Interfernce Cancellation (SIC) Detectors

A trade-off between the optimal performance and the reduced complexity implementation can be achieved using the SIC MIMO detectors. This detector is implemented for the ZF and the MMSE detectors based on the QR-factorization. There are different methods to construct the QR-factorization such as the Gram-Schmidt (GS), modified Gram-Schmidt (MGS), Householder transformation and many other methods [40]. The QR-factorization based MGS will be illustrated first followed by the ZF-SIC and the MMSE-SIC detectors.

2.4.3.1 QR-Factorization Based MGS

To illustrate this method, the thin matrix $\mathbf{H} \in \mathbb{C}^{N_r \times N_t}$ is defined as

$$
\mathbf{H} = \begin{bmatrix}
h_{1,1} & h_{1,2} & \ldots & h_{1,N_t} \\
h_{2,1} & h_{2,2} & \ldots & h_{2,N_t} \\
\vdots & \vdots & \ddots & \vdots \\
h_{N_r,1} & h_{N_r,2} & \ldots & h_{N_r,N_t}
\end{bmatrix} . \tag{2.17}
$$

Matrix $\mathbf{H}$ can be factorized into $\mathbf{H} = \mathbf{QR}$, where $\mathbf{Q} \in \mathbb{C}^{N_r \times N_t}$ is an orthonormal matrix and $\mathbf{R} \in \mathbb{C}^{N_t \times N_t}$ is an upper triangular matrix as shown in Algorithm 1. The MGS algorithm is a modification to the original GS algorithm that improves the column orthogonality of $\mathbf{Q}$ and makes the procedure more reliable.

Algorithm 1 : MGS[40]

1: **procedure** $\mathbf{H} = MGS(\mathbf{QR})$
2:     $[N_r, N_t] = size(\mathbf{H})$,
3:     $\mathbf{Q} = zeros(N_r, N_t)$,
4:     $\mathbf{R} = zeros(N_t, N_t)$,
5:     For $l = 1$ to N_t
6:         $\mathbf{R}(l, l) = ||\mathbf{H}(:, l)||$,
7:         $\mathbf{Q}(:, l) = \mathbf{H}(:, l)/\mathbf{R}(l, l)$,
8:         $\mathbf{R}(l, l+1 : N_t) = \mathbf{Q}^H(:, l) \times \mathbf{H}(:, l+1 : N_t)$,
9:         $\mathbf{H}(:, l+1 : n) = \mathbf{H}(:, l+1 : N_t) - \mathbf{Q}(:, l) \times \mathbf{R}(l, l+1 : N_t)$,
10:    end for
11:    **Return** $\mathbf{Q}, \mathbf{R}$.

2.4.3.2 ZF-SIC

Based on the QR-factorization of the channel matrix $\mathbf{H} = \mathbf{Q}\mathbf{R}$, the received signal of (2.10) can be written as

$$\mathbf{x} = \mathbf{Q}\mathbf{R}\mathbf{s} + \mathbf{w}. \tag{2.18}$$

This detector assumes multiplying (2.18) by $\mathbf{Q}^H$ such that

$$\mathbf{Q}^H\mathbf{x} = \mathbf{Q}^H\mathbf{Q}\mathbf{R}\mathbf{s} + \mathbf{Q}^H\mathbf{w},$$

$$\tilde{\mathbf{x}} = \mathbf{R}\mathbf{s} + \tilde{\mathbf{w}},$$

$$\begin{bmatrix} \tilde{x}_1 \\ \tilde{x}_2 \\ \vdots \\ \tilde{x}_{N_r} \end{bmatrix} = \begin{bmatrix} r_{1,1} & r_{1,2} & \cdots & r_{1,N_t} \\ 0 & r_{2,2} & \cdots & r_{2,N_t} \\ \vdots & \vdots & \ddots & \vdots \\ 0 & 0 & \cdots & r_{1,N_t} \end{bmatrix} \begin{bmatrix} s_1 \\ s_2 \\ \vdots \\ s_{N_t} \end{bmatrix} + \begin{bmatrix} \tilde{w}_1 \\ \tilde{w}_2 \\ \vdots \\ \tilde{w}_{N_t} \end{bmatrix}, \tag{2.19}$$

where $\tilde{\mathbf{x}} = \mathbf{Q}^H\mathbf{x} \in \mathbb{C}^{N_t \times 1}$ and $\tilde{\mathbf{w}} = \mathbf{Q}^H\mathbf{w} \in \mathbb{C}^{N_t \times 1}$. The equalization process starts by estimating $\tilde{s}_{N_t}$ in a back substitution procedure ends at $\tilde{s}_1$ such that

$$\tilde{s}_{N_t} = \frac{\tilde{x}_{N_t}}{r_{1,N_t}},$$

$$\tilde{s}_{N_t-1} = \frac{\tilde{x}_{N_t-1} - r_{N_t-1N_t}\tilde{s}_{N_t}}{r_{N_t-1N_t-1}},$$

$$\vdots$$

$$\tilde{s}_1 = \frac{\tilde{x}_1 - \cdots - r_{1N_t}\tilde{s}_{N_t}}{r_{11}}, \tag{2.20}$$

where $\tilde{s}_l$ is the estimation of the l-th symbol and $l = 1, 2, \ldots, N_t$.

2.4.3.3 MMSE-SIC

The MMSE-SIC detectors have improved performance compared to the ZF-SIC detectors due to the background noise elimination [5]. This detector can be implemented using the same procedure as the ZF-SIC but with the following modifications,

- The extended channel matrix can be written as $\mathbf{H}_{ex} = \left[\mathbf{H}^T \sqrt{\frac{N_0}{E_s}} \mathbf{I}_{N_t} \right]$.

- The received signal are extended with zero padding such that $\mathbf{x}_{ex} = \left[\mathbf{x}^T \mathbf{0} \right]^T$.

- The extended noise vector can be written as $\mathbf{w}_{ex} = \left[\mathbf{w}^T \quad -\sqrt{\frac{N_0}{E_s}}\mathbf{s}^T \right]^T$.

- The QR-factorization of the extended channel matrix $\mathbf{H}_{ex}$ can be written as $\mathbf{H}_{ex} = \mathbf{Q}_{ex}\mathbf{R}_{ex}$.

2.5 Forward Error Correcting (FEC) Coding

The early beginnings of the coding and information theory goes back to 1948 when Claude Shannon defined the channel capacity rate in his published paper [41], which is a limit for the information flow in any communication system in the presence of noise [41, 42, 43, 44]. Since then, the attempts have been made to reach that limit using different error correcting codes (ECCs), and Fig. 2.4 describes the block diagram of the coded communication system. The Hamming codes and Golay codes are the first ECCs that are invented in 1974 [45], which are very basic codes and have limited ability for correction. More sophisticated codes have been developed over the past few decades to achieve Shannon limit and most of these techniques have used iterative decoders such as the parallel concatenating convolutional codes (PCCCs), which are also known as turbo codes, and long irregular LDPC codes.

The principle of ECCs can be summarized as follows, a redundant bits or symbols to be added to the information blocks before the transmission to correct the errors occurred at the received signals. Some of the codes are systematic, which means that the code word can be divided into a systematic part which consists of the information, and the redundant part that is used to correct the erroneous bits or symbols of the information [43, 45]. While other codes are non-systematic, which means that the information part does not appear in the code word.

In general, ECCs can be classified based on the way of adding the redundant part into two groups, block, and convolutional codes. In the block codes, the information is processed on block basis which means that each block of information is encoded individually and it depends on the current state of the information only, and the LDPC codes are an example of these codes. On the other hand, the information in the convolutional codes are processed either on a block basis or bit basis and the encoder requires the current and the previous input and output of the information [45].

The aim of this chapter is to illustrate the principles of the FEC coding and to demonstrate the encoding and decoding process for some of the well-known codes. First, the convolutional encoder and decoder are illustrated, then the structure of the turbo codes is described including the different decoding techniques. Finally, the irregular LDPC codes
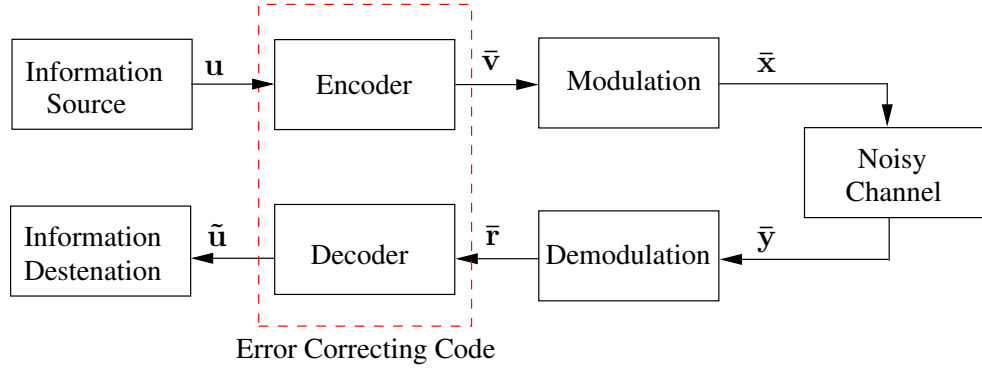
Figure 2.4: Diagram of the coded communication systems [45].

are described including the encoder and the decoder design. The main focus of this chapter is the coding techniques that are related to this work.

2.6 Convolutional Codes

Convolutional codes are one of the first ECCs that are invented by Elias in 1955 [45, 42, 44]. The encoder representation of these codes is a linear finite-state shift register and the code-words of size n are generated by passing the k size information through that shift-register with coding rate k/n and using the equivalent function generator [31, 46]. Many decoders have been used with these codes, but the Viterbi decoder that is invented in 1967 is the most popular algorithm, these codes have been widely adopted in the communication systems such as, the international mobile telecommunication standard 2000 (IMT-2000), and the global system for mobile (GSM) [45]. On the other hand, combining these codes in parallel with an interleaver results in a more sophisticated code with a performance that approaches Shannon limit [31, 47].

2.6.1 Encoder

The general form of the convolutional encoder is demonstrated in Fig. 2.5 [31]. The constraint length K of the convolutional code determines the number of stages for the shift registers and each stage consists of k bits. The input data are shifted through the shift-registers and the n bits code-word is calculated through an equivalent number of linear algebraic functions called function generators [31]. These function generators are described in octal forms, such as the $(5, 7)_8$ code which can be written as $g_1 = [101]$, $g_2 = [111]$. Convolutional codes can be divided based on their function generators into recursive systematic codes (RSC) and non-recursive non-systematic codes (NRSC).
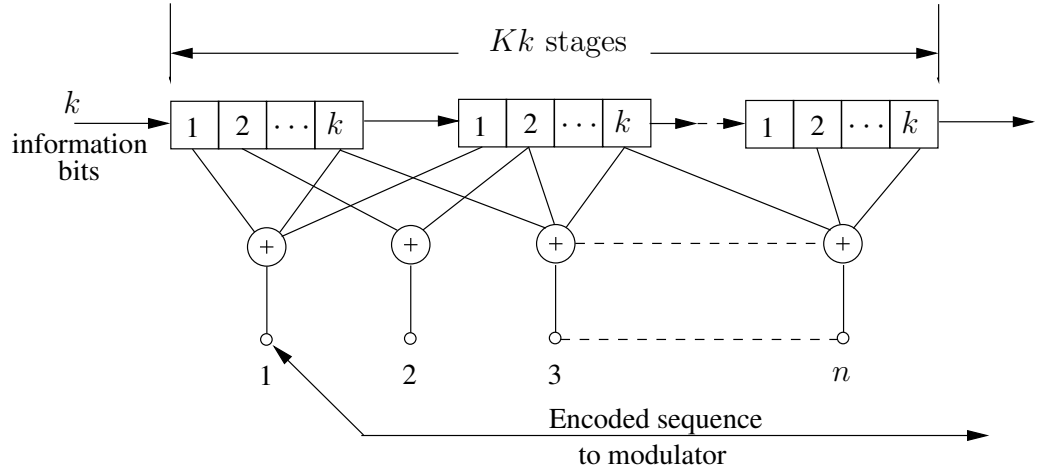
Figure 2.5: Convolutional encoder [31].
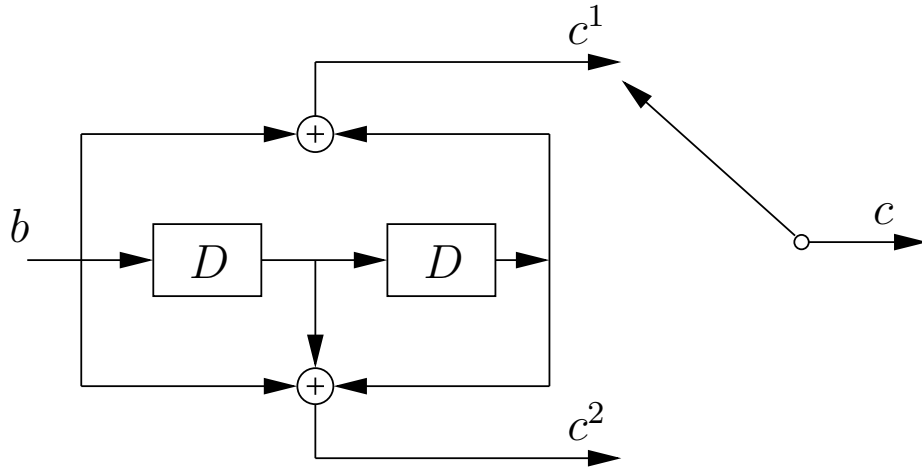
Figure 2.6: Convolutional encoder for $(5, 7)_8$ code [48].

2.6.1.1 Non-recursive Non-systematic Codes (NRNSC)

The structure of this code is illustrated in Fig. 2.6 [48] for the $(5, 7)_8$ code and can be written as $G = [g_1 g_2]$, it shows that the code word is a function of the present and previous states of the input. As can be seen, the output code words are $\mathbf{c} = [c_0^1 c_0^2, c_1^1 c_1^2, \ldots, c_m^1 c_m^2]$ which are equivalent to the input sequence $\mathbf{b} = [b_0, b_1, \ldots, b_m]$. Appendix A includes a list of the optimum convolutional codes with its constraint length and the free distance for different coding rates.

2.6.1.2 Recursive Systematic Codes (RSC)

These codes are called systematic because their code words consist of two parts, the information sequence, and the parity bits. The structure of this code is illustrated in Fig. 2.7 for the code $(1, 7/5)_8$ and using $G' = [1, g_2/g_1]$, which shows that the code word is a function of the present and previous states of the input and the output.
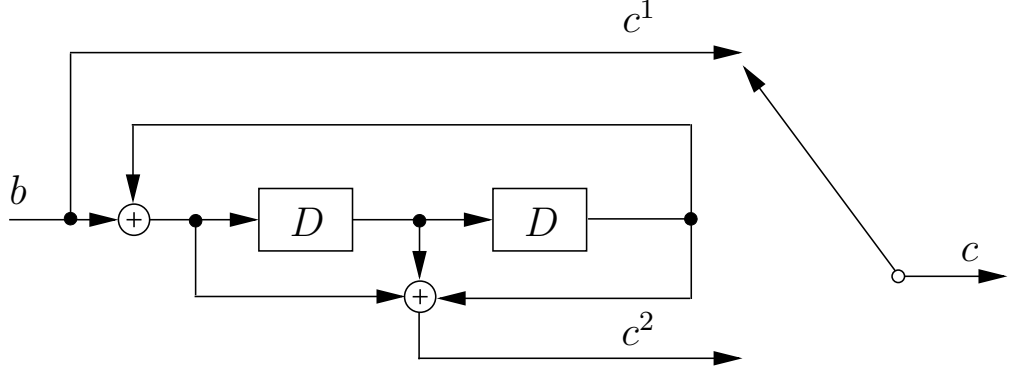
Figure 2.7: Convolutional encoder for $(1, 7/5)_8$ RSC code.

2.6.2 Decoder

There are several procedures to decode the code words of the convolutional codes and the selection of the decoding methods depend on the constraint length of the code [31]. The optimal decoder can only be used for the low constraint length codes which is the Viterbi decoder that includes maximum-likelihood decoding. However, for high constraint lengths, it is more convenient to use the maximum a posteriori algorithm which has lower complexity change at high constraint length codes.

2.6.2.1 Maximum-Likelihood Decoder (Viterbi Decoder)

The Viterbi decoder is considered as the optimal decoding method for the convolutional codes due to the maximum-likelihood search for the most possible sequence in the trellis [31, 49]. The trellis diagram of the $(5, 7)_8$ code is shown in Fig. 2.8 with four time instances.

The soft decoding procedure can be summarized for the additive white Gaussian noise (AWGN) channel as follows [50],

1. The received signal $\mathbf{r}_t = r_t^{(1)}, r_t^{(2)}, \ldots, r_t^{(n)}$ at time t can be written as

$$r_t^{(i)} = a_t^{(i)} + n_t^{(i)}, \tag{2.21}$$

   where $a_t^{(i)}$ and $n_t^{(i)}$, are the mapped code word and the AWGN signals at index $i = 1, 2, \ldots, n$.

2. The AWGN channel parameters are assumed to be independent and identically dis-

21
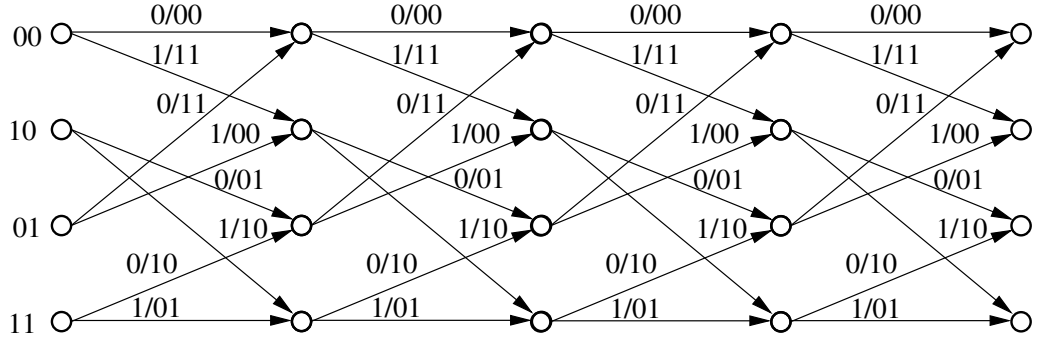
Figure 2.8: Trellis diagram for the $(5,7)_8$ code [50].

tributed (i.i.d), which means that the likelihood for this channel can be written as,

$$f(\mathbf{r}_t|\mathbf{a}_t) = \prod_{i=1}^{n} \frac{1}{\sqrt{2\pi\sigma^2}} \exp[-\frac{(r_t^{(i)} - a_t^{(i)})^2}{2\sigma^2}]. \tag{2.22}$$

3. The likelihood function for the entire received sequence can be written as

$$f(\mathbf{r}|\mathbf{a}) = f(\mathbf{r}_0, \mathbf{r}_1, \ldots, \mathbf{r}_{L-1}|\mathbf{a}_0, \mathbf{a}_1, \ldots, \mathbf{a}_{L-1}) = \prod_{t=0}^{L-1} f(\mathbf{r}_t|\mathbf{a}_t). \tag{2.23}$$

The log-likelihood representation for this function can be written as,

$$\log_e(f(\mathbf{r}|\mathbf{a})) = \sum_{t=0}^{L-1} \log_e(f(\mathbf{r}_t|\mathbf{a}_t)). \tag{2.24}$$

4. Lets define the path metric as

$$M_t(q) = -\sum_{i=0}^{t} \log_e(f(\mathbf{r}_i|\mathbf{a}_i)) = M_{t-1}(p) + \mu_t(\mathbf{r}_t, \hat{\mathbf{a}}^{(p,q)}), \tag{2.25}$$

where p and q are the trellis states at time t and $t+1$ respectively, and $\mu_t(\mathbf{r}_t, \hat{\mathbf{a}}_t)$ is the branch metric from state p to state q that can be written as

$$\mu_t(\mathbf{r}_t, \hat{\mathbf{a}}_t) = a[-\log_e(f(\mathbf{r}_t|\hat{\mathbf{a}}^{(p,q)})) - b], \tag{2.26}$$

where a and b are arbitrary positive constants.

5. The consecutive procedure continued by selecting the path with smallest path metric and increment t until the sequence ends.

2.6.2.2 Maximum A Posteriori (MAP) Decoder (The BCJR Decoder)

The maximum a posteriori (MAP) decoder is also called BCJR decoder after the initial of its inventors Bahl, Cock, Jelenik, and Raviv. The performance of this decoder is almost the same as Viterbi decoder but with higher complexity [50]. This decoder is an optimal algorithm that minimizes the probability of a symbol error and its algorithm can be summarized as follows [45, 51, 52],

1. The decoder inputs are the received signals $\mathbf{r}$ and the a priori L-values that are calculated using,

$$L(a_t|\mathbf{r}) = \log_e \left(\frac{p(a_t = -1|\mathbf{r})}{p(a_t = +1|\mathbf{r})} \right). \tag{2.27}$$

2. The states of the trellis diagram of Fig. 2.8 is defined as $S_{t-1} = s'$ and $S_t = s$, and using Bayes' rule, the L-values of (2.27) can be rewritten as,

$$L(a_t|\mathbf{r}) = \log_e \left(\frac{\sum_{a_t=+1} p(S_{t-1} = s', S_t = s, \mathbf{r})}{\sum_{a_t=-1} p(S_{t-1} = s', S_t = s, \mathbf{r})} \right). \tag{2.28}$$

3. The probability of $p(s', s, \mathbf{r})$ can further be written as,

$$p(s', s, \mathbf{r}) = \beta_{t+1}(s)\gamma_t(s', s)\alpha_{t-1}(s'), \tag{2.29}$$

where $\beta_t(s) = p(\mathbf{r}_{>t}|s)$ is the probability that the trellis is in state s at time t, $\gamma_t(s', s) = p([s, \mathbf{r}_t]|s')$ is the probability of the state transition from s' to s, and finally $\alpha_{t-1}(s') = p(s', \mathbf{r}_{<t})$ is the probability that the trellis is in state s' at time $t-1$. The terms $\mathbf{r}_{>t}, \mathbf{r}_t, \mathbf{r}_{<t}$, represents the future received sequence, present sequence and prior to the present sequence of the received code word.

4. The initial value of $\alpha_{t-1}(s')$ is set to $\alpha_0(S = 0) = 1$ and $\alpha_0(S = s) = 0$ otherwise, and the forward recursive calculation of $\alpha_t(s)$ can be calculated using,

$$\alpha_t(s) = \sum_{all \ s'} \gamma_t(s', s)\alpha_{t-1}(s'). \tag{2.30}$$

5. The final value for $\beta_L(s) = 1$ is set to $\beta_L(s) = 1$ for all s, and the backward recursive calculation of the $\beta_t(s)$ can be calculated using,

$$\beta_t(s') = \sum_{all \ s} \beta_{t+1}(s)\gamma_t(s', s). \tag{2.31}$$

23

6. The term $\gamma_t(s', s)$ can be calculated using,

$$\gamma_t(s', s) = \frac{1}{\sqrt{2\pi\sigma^2}} \exp\left(\frac{-|r_t - \sqrt{E_s}a^{(s', s)}|^2}{2\sigma^2}\right), \tag{2.32}$$

and therefore, equation (2.27) can be rewritten as,

$$L(a_t|\mathbf{r}) = \log_e\left(\frac{\sum_{(s', s) \in S^+} \beta_{t+1}(s)\gamma_t(s', s)\alpha_{t-1}(s')}{\sum_{(s', s) \in S^-} \beta_{t+1}(s)\gamma_t(s', s)\alpha_{t-1}(s')}\right). \tag{2.33}$$

7. Finally, the decision v_t on the decoded bits can be calculated using,

$$v_t = \text{sign}[L(a_t|\mathbf{r})]. \tag{2.34}$$

The complexity of the Viterbi decoder and the MAP decoder are extremely high especially at large constraint length codes due to the extensive search of the maximum likelihood. These decoders have limited applications to the turbo codes due to the iterative procedure and therefore, sub-optimal decoders with reduced complexity are to be used instead. The complexity of the MAP decoder can enormously be reduced using the log MAP algorithm or the max-log MAP algorithm but on the cost of a slight degradation in the performance, these algorithms will be highlighted in the next sections.

2.6.2.3   Log MAP Decoder

This algorithm is a sub-optimal decoder to the convolutional codes, its basic approach is to take the logarithm for the parameters, $\alpha_t(s'), \beta_t(s)$ and $\gamma_t(s', s)$. Then, the Jacobian algorithm [53] can be applied to simplify the calculation of these parameters as [52, 49],

$$\log_e(e^{x_1} + e^{x_2}) \approx \max(x_1, x_2) + f_c(|x_2 - x_1|), \tag{2.35}$$

where $f_c(|x_2 - x_1|)$ is the correction function and their values are listed in a look-up table. Therefore, equations (2.30),(2.31), and (2.32) can be rewritten as,

$$\alpha_t(s) = \log_e(\sum_{all\ s'} \gamma_t(s', s)\alpha_{t-1}(s')) \approx \max(\gamma_t(s', s), \alpha_{t-1}(s')) - f_c(|\alpha_{t-1}(s') - \gamma_t(s', s)|),$$
$$\tag{2.36}$$

$$\beta_t(s') = \log_e(\sum_{all\ s} \beta_{t+1}(s)\gamma_t(s', s)) \approx \max(\gamma_t(s', s), \beta_{t+1}(s)) - f_c(|\beta_{t+1}(s) - \gamma_t(s', s)|),$$
$$\tag{2.37}$$

$$\gamma_t(s', s) = \log_e \left(\frac{1}{\sqrt{2\pi\sigma^2}} \exp\left(\frac{-|r_t - \sqrt{E_s}a^{(s',s)}|^2}{2\sigma^2} \right) \right),$$

$$= -\log_e(\sqrt{2\pi\sigma^2}) - (|r_t - \sqrt{E_s}a^{(s',s)}|^2). \tag{2.38}$$

Equation (2.33) can be rewritten as,

$$L(a_t|\mathbf{r}) = \log_e \left(\frac{\sum_{(s',s)\in S^+} e^{(\beta_{t+1}(s)+\gamma_t(s',s)+\alpha_{t-1}(s'))}}{\sum_{(s',s)\in S^-} e^{(\beta_{t+1}(s)+\gamma_t(s',s)+\alpha_{t-1}(s'))}} \right). \tag{2.39}$$

2.6.2.4 Max-Log MAP Decoder

The complexity of the log MAP decoder can further be reduced by neglecting the correction function part in the calculation of the parameters $\alpha_t(s')$ and $\beta_t(s)$ from (2.36) and (2.37), respectively. This simplification is called max-log MAP algorithm and it can be written as,

$$\log_e(e^{x_1} + e^{x_2} + \ldots + e^{x_L}) \approx \max(x_1, x_2, \ldots, x_L). \tag{2.40}$$

Based on that, the algorithm that is illustrated in Section 2.6.2.3 applies here but with updating the equations for calculating $\alpha_t(s')$ and $\beta_t(s)$ into,

$$\alpha_t(s) = \log_e(\sum_{all\ s'} \gamma_t(s', s)\alpha_{t-1}(s')) \approx \max(\gamma_t(s', s), \alpha_{t-1}(s')), \tag{2.41}$$

$$\beta_t(s') = \log_e(\sum_{all\ s} \beta_{t+1}(s)\gamma_t(s', s)) \approx \max(\gamma_t(s', s), \beta_{t+1}(s)), \tag{2.42}$$

The performance of the convolutional code depends mainly on the constraint length, the higher the constraint length the better performance and the higher complexity. Alternatively, more sophisticated codes can be employed with reduced complexity to achieve Shannon limit such as the turbo codes and the LDPC codes.

2.7 Turbo Codes

Forward error correcting codes FEC are widely used in wireless communication systems to reduce the bit error rate of the received signal during the transmission of the data through a wireless channel. For example, turbo codes have been used in 3G mobile communication and for deep-space communication as an error correcting codes [52]. Turbo codes were invented by Berrou, Glavieux and Thitimajashima in 1993, and it has
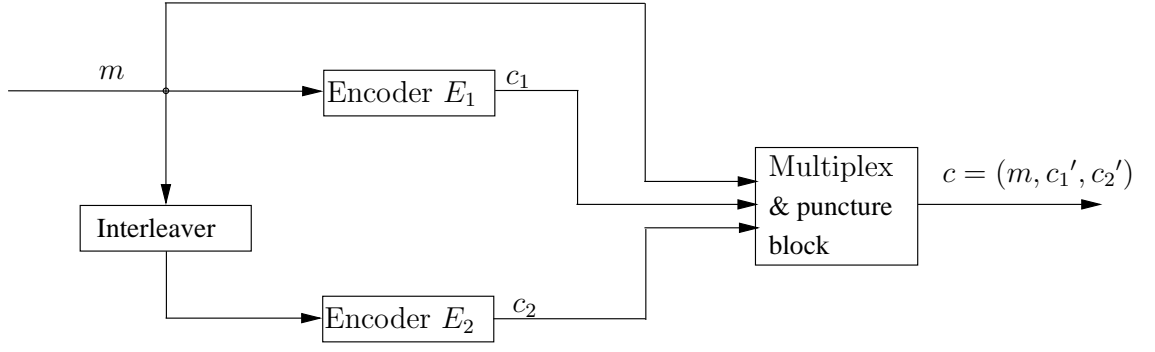
Figure 2.9: Turbo Encoder [47].

shown a great performance for a very long codes with acceptable complexity [52, 48, 50]. The main structure of the turbo encoder may consist of two or more RSC or non recursive systematic code (NRSC) for the convolutional encoders concatenated in parallel and separated by an interleaver [48]. On the receiving end, a decoder is required to extract the transmitted message from the received code word in an iterative procedure [54]. The selection of the turbo decoder depends on the system requirements and the decoder specifications. In general, the BCJR and MAP algorithms are the highest in complexity algorithms which can be reduced into log MAP algorithm with a small degradation in the system performance. On the other hand, max-log MAP algorithm and soft-output Viterbi algorithm (SOVA) can be used as turbo decoders with reduced complexity and performance [52]. The design of the encoder and the decoder of the turbo codes will be illustrated in the next sections.

2.7.1 Turbo Encoder

The turbo encoder consists of two RSC encoders as shown in Fig. 2.9, both of them are of rate $1/2$ and they are separated by a block interleaver. The overall rate of this encoder is $R = 1/3$ which can be calculated using (2.43). However, it can be reduced to $1/2$ to improve the coding rate and increase the transmission efficiency by using the puncture function as shown in Fig. 2.11.

$$R = \frac{R_1 R_2}{R_1 + R_2 - R_1 R_2},$$
(2.43)

where, R_1 and R_2 are the rates of the first and the second convolutional codes [47, 45, 42]. The aim of the puncturing process is to increase the coding rate by removing some of the parity bits periodically from the code word of each RSC without affecting the systematic
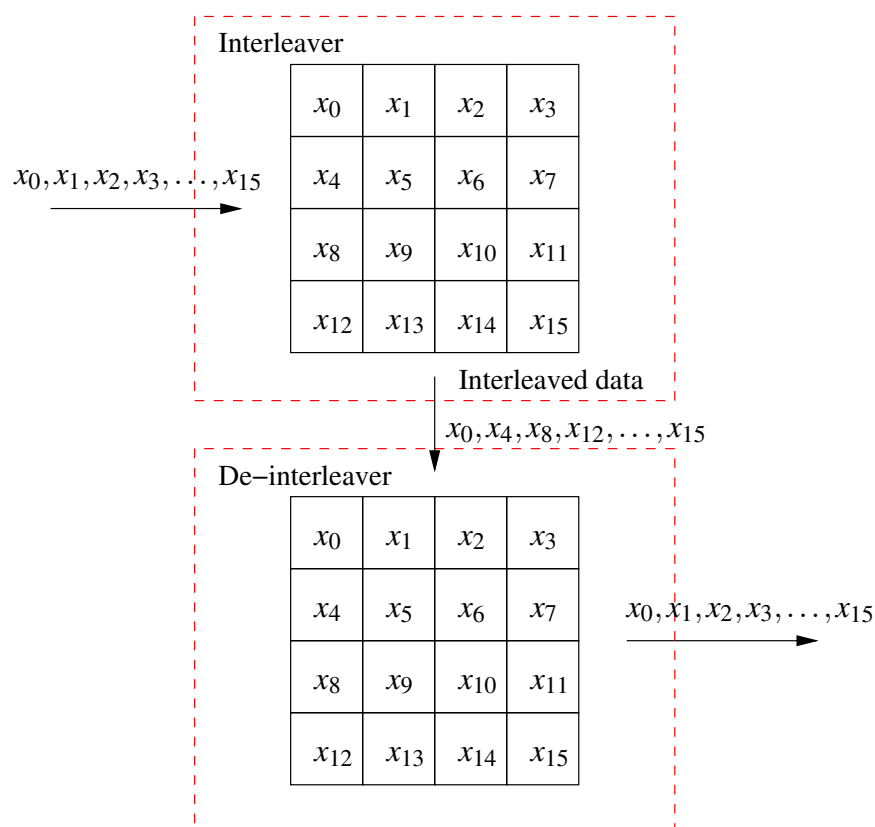
Figure 2.10: Rows-columns interleaver [50].

data sequence as shown in Fig. 2.11. In addition, different coding rates can be achieved with a suitable puncturing process in the encoder. At the decoder, the punctured symbols have to be replaced by zeros to prevent accumulating their branch metrics [50]. The interleaver is used here to produce a permuted version of the data before it enters the second RSC encoder to achieve statistically independent parity bits by each encoder [47, 55]. There are mainly several types of interleavers that can be used, such as the random interleavers, LTE interleavers and the row-column interleavers. Fig. 2.10 shows a simple row-column interleaver with 4×4 matrix, which shows that the data to be interleaved have to be written in a row order and the interleaved data are to be read in a column order. The deinterleaving process is the reciprocal of this procedure as the interleaved data have to be written in a column order and to be read in a row order.

Demultiplex

Unpunctured

$y^s(1)$	$y^{1p}(1)$	$y^{2p}(1^i)$	$y^s(2)$	$y^{1p}(2)$	$y^{2p}(2^i)$

$y^s(1)$	$y^{1p}(1)$	$y^{2p}(1^i)$	$y^s(2)$	$y^{1p}(2)$	$y^{2p}(2^i)$

I

$y^s(1)$	$y^{1p}(1)$	$y^s(2)$	$y^{2p}(2^i)$	$y^s(3)$	$y^{1p}(3)$

Punctured

Interleaver

$y^s(1)$	$y^{1p}(1)$	$y^s(2)$	$y^{1p}(2)$	$y^s(3)$	$y^{1p}(3)$	Decoder 1
$y^s(1^i)$	$y^{2p}(1^i)$	$y^s(2^i)$	$y^{2p}(2^i)$	$y^s(3^i)$	$y^{2p}(2^i)$	Decoder 2

$y^s(1)$	$y^{1p}(1)$	$y^s(2)$	0	$y^s(3)$	$y^{1p}(3)$	Decoder 1
$y^s(1^i)$	0	$y^s(2^i)$	$y^{2p}(2^i)$	$y^s(3^i)$	0	Decoder 2
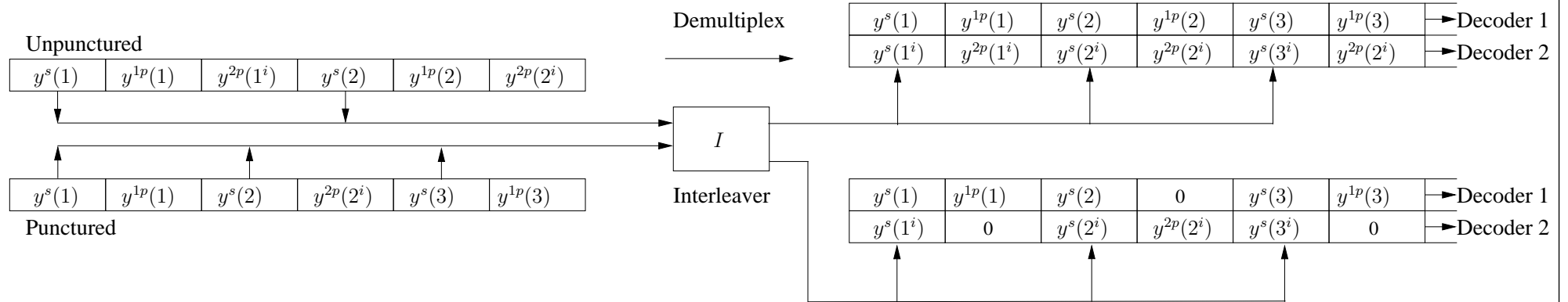
Figure 2.11: Puncturing / Depuncturing process [52, 55].

2.7.2 Turbo Decoder

The outstanding performance of the turbo codes compared to other known codes as a result of the iterative decoding procedure between the two parallel concatenated RSC decoders are the main reason behind this name, which is known to achieve near Shannon limit performance [48, 56]. The schematic diagram for the turbo decoder is illustrated in Fig. 2.12 and the decoding procedure starts by receiving the code word $\mathbf{r} = [r_1^{(0)}, r_1^{(1)}, r_1^{(2)}, \cdots, r_N^{(0)}, r_N^{(1)}, r_N^{(2)}]$, which consists of the systematic part $r_t^{(0)}$, the parity of the first encoder $r_t^{(1)}$, and the parity of the second encoder $r_t^{(2)}$.

The convolutional decoders that are illustrated in Section 2.7.2 can be utilized for the first and the second decoders of Fig. 2.12. The first decoder receives $r_t^{(0)}$ and $r_t^{(1)}$, in addition to an initial a priori information received from the output of the second decoder after its being deinterleaved, the initial condition for the a priori will be zero at the first iteration. The log likelihood ratio LLR of the information for the first decoder can be calculated using,

$$LLR(r_t^{(0)}|a_t^{(0)}) = \log_e \left(\frac{P(r_t^{(0)}|a_t^{(0)} = +1)}{P(r_t^{(0)}|a_t^{(0)} = -1)} \right). \tag{2.44}$$

In a special case when the channel is AWGN and the modulation type is 4-QAM, the LLR can be simplified for the real and imaginary parts as,

$$LLR_0(r_t^{(0)}|a_t^{(0)}) = \frac{2\sqrt{E_s}}{\sigma^2}\text{Re}(r_t^{(0)}), \tag{2.45}$$

$$LLR_1(r_t^{(0)}|a_t^{(0)}) = \frac{2\sqrt{E_s}}{\sigma^2}\text{Im}(r_t^{(0)}). \tag{2.46}$$

Similar calculations for the 16-QAM scheme can be obtained to achieve four levels of LLR values for each received constellation symbol. These LLR values will be used in the decoder to calculate the reliability of the first code $L_t^{(1)}$ which then will be subtracted from the information signal and the a priori of the first decoder to produce the extrinsic information $E_t^{(1)}$ from the first decoder as,

$$E_t^{(1)} = L_t^{(1)} - r_t^{(0)} - \Lambda_t^{(1)}, \tag{2.47}$$

where $\Lambda_t^{(1)} = \Pi^{-1}(E_t^{(2)})$ is the a priori information to the first decoder. Similarly, $\Lambda_t^{(2)} = \Pi(E_t^{(1)})$ is the a priori information to the second decoder, that is produced from
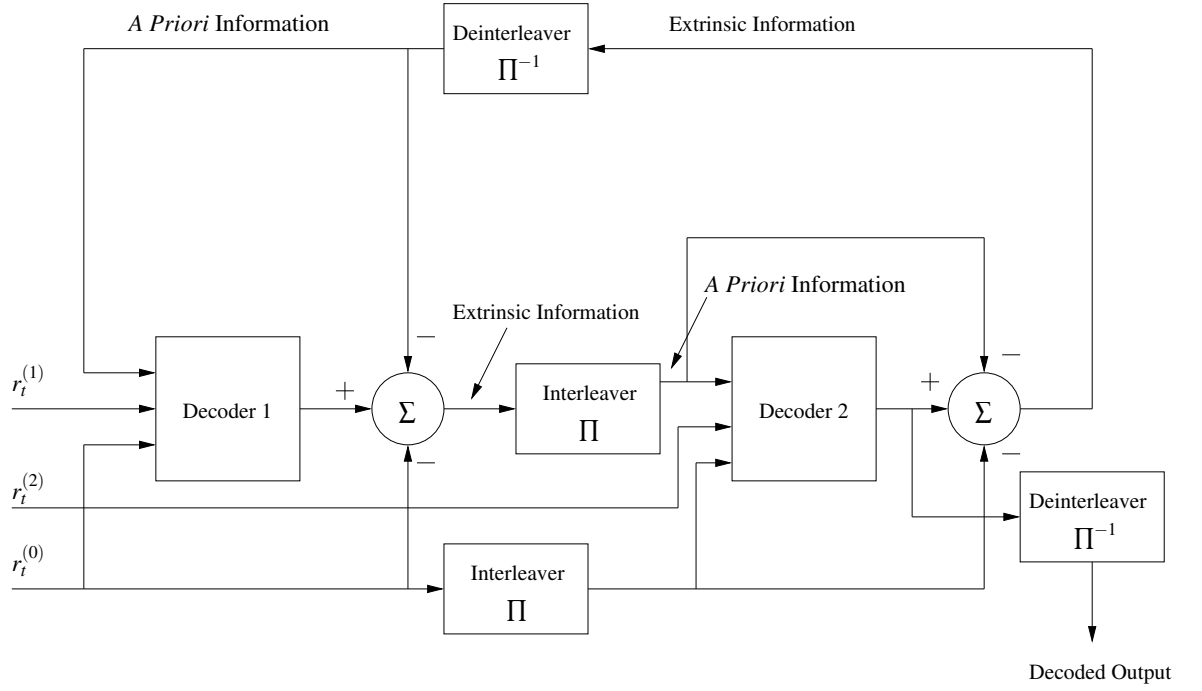
Figure 2.12: Schematic diagram of Turbo decoder [52].

interleaving the extrinsic information of the first decoder. In the same procedure, the a priori information $\Lambda_t^{(2)}$ with the interleaved systematic information and the output of the second encoder $r_t^{(2)}$ will produce the reliability of the second decoder $L_t^{(2)}$. The extrinsic information for the second decoder can be calculated using,

$$E_t^{(2)} = L_t^{(2)} - \Pi(r_t^{(0)}) - \Lambda_t^{(2)}. \tag{2.48}$$

The extrinsic information of the second decoder is deinterleaved and sent back to the first decoder as a priori information. This algorithm will proceed for several iterations and the decoded output of the second decoder should be deinterleaved to produce the required information [52, 47]. Since the turbo codes rely on the iterative procedure between the two convolutional codes, then the complexity of the decoders have to be as minimum as possible especially for the large constraint length codes. Therefore, the selection of the RSC decoder is practically limited to the log MAP, max-log MAP and the SOVA decoders as illustrated in Section 2.6.2.

2.8 Low-Density Parity-Check (LDPC) Codes

LDPC codes are an iterative decoding error correcting codes which are first invented by Gallager in 1962 [57] and updated by Tanner in 1981 [58]. Then this code remains unknown for several years until it rediscovered by Mackay and Neal in 1995 [59]. These codes are a class of linear block codes and their performance is known to achieve near-capacity performance [52, 55].

The parity check matrix of the LDPC codes can be represented as a sparse matrix $\mathbf{H}_p$ with a number of ones distributed to its rows and columns that are called weights. Based on the rows and the columns weight distribution, these codes can be divided into regular and irregular LDPC codes. In the regular LDPC codes, the number of weights are constant for all the rows and similarly for all the columns. On the contrary, if the row weights and the column weights are varied, the code is known as irregular LDPC codes [48].

2.8.1 LDPC Code Representation

The LDPC code can be represented in two configurations; the parity check matrix and Tanner graph. In the beginning, there are three parameters to define for the LDPC code which are, the code word length N_c, the matrix dimension N_r, and the parity bits $N_p = N_c - N_r$. In addition, the number of 1's in each row and column are called weights, which are denoted for the rows as η_r and for the columns as η_c. These parameters are used to construct the parity matrix and Tanner graph as will be illustrated in the next sections.

2.8.1.1 The Parity Check Matrix

The construction of the LDPC codes is mainly based on the parity check matrix. Therefore, LDPC codes can be classified into [52, 50],

1. Regular LDPC code, which has fixed row and column weights in the parity check matrix, has the following parity check matrix

$$
\mathbf{H}_p = \begin{bmatrix} 1 & 1 & 1 & 1 & 0 & 0 & 0 & 0 \\ 0 & 0 & 0 & 0 & 1 & 1 & 1 & 1 \\ 1 & 1 & 0 & 0 & 1 & 1 & 0 & 0 \\ 0 & 0 & 1 & 1 & 0 & 0 & 1 & 1 \end{bmatrix}, \tag{2.49}
$$
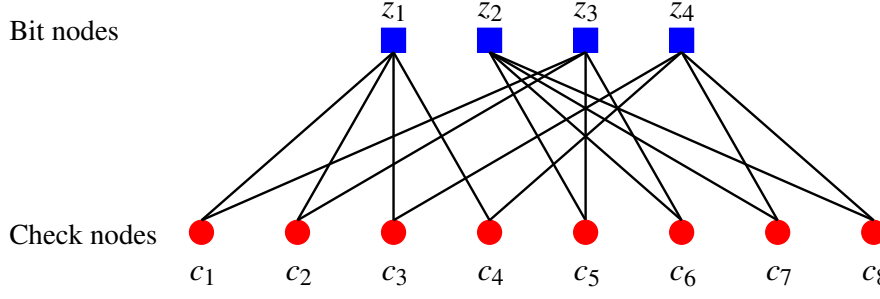
Figure 2.13: Tanner graph for the parity check matrix of (2.49).

where the row and the column weights are $\eta_r = 4$ and $\eta_c = 2$, respectively. The construction of the parity check matrix can be either randomly created or structured, where the random method has normally better performance [48].

2. Unlike the regular LDPC code, irregular LDPC code has variable column and row weights in the parity check matrix. Therefore, the performance of the irregular LDPC codes is better than the regular LDPC codes and it is more practical than the regular codes.

2.8.1.2   Tanner Graph

Tanner graph is a technique that is proposed by Michel Tanner in 1981 to construct long error correcting codes utilizing short error codes [58]. The graph of Fig. 2.8.1.2 consists of two sets of nodes namely, the bit nodes and the check nodes. The relationship between the check nodes and the bit nodes can be demonstrated based on the columns of the parity check matrix of (2.49). To illustrate, the check node c_1 is connected to the bit nodes $\{z_1, z_3\}$, and similarly for the other check nodes. The bit node z_1 is connected to the check nodes $\{c_1, c_2, c_3, c_4\}$, and similarly for the other bit nodes. The cyclic process of the Tanner graph can be defined as the path that starts at a coded bit and ends at the same node which should exceed 4 for better performance. The bipartite diagram of Fig. 2.8.1.2 has more than one cyclic with length ≤ 4 such as, $c_3 \rightarrow z_1 \rightarrow c_4 \rightarrow z_4 \rightarrow c_3$. Therefore, the parity check matrix of (2.49) has a bad performance and cannot be used in the coding [52].
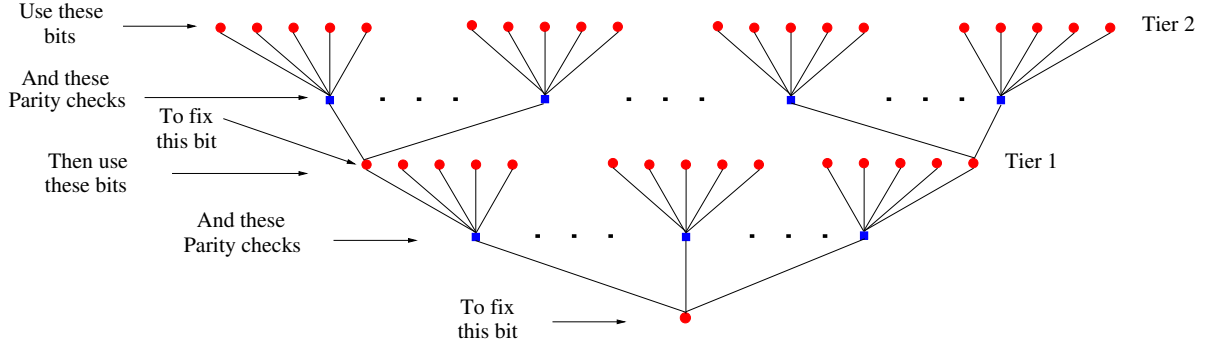
Figure 2.14: Two tier parity check tree associated with Tanner graph.

2.8.2 LDPC Encoder

The encoding process for the LDPC codes requires the following steps,

1. Transforming the parity check matrix $\mathbf{H}_p$ into a systematic form such that, $\bar{\mathbf{H}}_p = [\mathbf{I}_{N_p} \ \mathbf{P}^T]$, using Gauss-Jordan elimination [52, 48], where $\mathbf{I}_{N_r}$ and $\mathbf{P}^\mathbf{T}$ are the identity matrix with dimensions of N_r and the parity matrix with dimensions $N_r \times N_p$, respectively.

2. Constructing the generator matrix $\mathbf{G}_p = [\mathbf{P} \ \mathbf{I}_{N_p}]$ which will be used to encode the information block.

3. The code word w_c can be generated now by multiplying the information message w_u and the generator matrix $\mathbf{G}_p$ as, $w_c = w_u \mathbf{G}_p^T$.

2.8.3 LDPC Decoder

The presented algorithm of LDPC decoder in this section is called the iterative belief propagation (IBP) or sum-product algorithm (SPA) [52, 48, 50, 45]. The probabilities are propagated through Tanner graph and accumulated to obtain the desired code word with the minimum probability of error. This algorithm involves calculating q_{ij} which is defined as the probability of the j-th code bit that is related to all the check bits except the i-th node, i.e. $q_{i,j} = p(c_j = x | \{z_i = 0, i' \in N_j/i\})$, where N_j is the set of all the code bit nodes. It also involves calculating $r_{i,j}$ which represents the probability of the i-th parity check that is related to all the possible coded bits, that is $r_{i,j} = p(z_i = 0|c)$ [52, 50].

Considering Tanner graph of Fig. 2.8.3, that demonstrates the probability propagation between the code nodes and the check nodes. The decoding procedure requires initialization to the q_{ij} parameters before calculating the horizontal and vertical steps, which will be illustrated next.

2.8.3.1 The Initialization Step

The initialization of the parameters q_{ij} is calculated using the channel PDF f_j^x for the j-th received symbol that equals x. As an example, the initialization for the AWGN channels can be written as [52, 50, 48]

$$
\begin{aligned}
f_j^0 &= \frac{\exp(-\frac{(r_j+1)^2}{2\sigma^2})}{\sqrt{2\pi}\sigma}, \\
f_j^1 &= \frac{\exp(-\frac{(r_j-1)^2}{2\sigma^2})}{\sqrt{2\pi}\sigma},
\end{aligned}
\tag{2.50}
$$

where r_j represents the j-th received symbol. These values are used as initials to the q_{ij} parameters and the $\mathbf{Q}$ matrix is initiated as

$$
\mathbf{Q} = \begin{bmatrix}
q_{1,1} = f_1^\lambda & q_{1,2} = f_2^\lambda & \cdots & q_{1,j} = f_{N_j}^\lambda \\
q_{2,1} = f_1^\lambda & q_{2,2} = f_2^\lambda & \cdots & q_{2,j} = f_{N_j}^\lambda \\
\vdots & \vdots & \cdots & \vdots \\
q_{i,1} = f_1^\lambda & q_{i,2} = f_2^\lambda & \cdots & q_{i,j} = f_{N_j}^\lambda
\end{bmatrix},
\tag{2.51}
$$

where N_j is the number of check nodes in Tanner Graph, and the superscript λ takes the values $\{0, 1\}$.

2.8.3.2 The Horizontal Step

After initializing the q_{ij} parameters, the decoding process starts by calculating the r_{ij} parameters utilizing the initial values using [52, 50]

$$
r_{ij} = \sum_{\mathbf{c}:c_j=x} p(z_i = 0|\mathbf{c}) \prod_{j' \in N_i/j} q_{ij'},
\tag{2.52}
$$

where $p(z_i = 0|\mathbf{c})$ is either 0 or 1. Similarly, the r_{ij} can be written in the matrix form as [52]

$$
\mathbf{R} = \begin{bmatrix}
r_{1,1} & r_{1,2} & \cdots & r_{1,j} \\
r_{2,1} & r_{2,2} & \cdots & r_{2,j} \\
\vdots & \vdots & \cdots & \vdots \\
r_{i,1} & r_{i,2} & \cdots & r_{i,j}
\end{bmatrix}.
\tag{2.53}
$$

2.8.3.3 The Vertical Step

On the other hand, the q_{ij} probabilities are updated in this step based on Baye's Rule using [52, 50]

$$q_{ij} = \frac{p(c_j = x)p(z_i = 0, j' \in N_j/i | c_j = x)}{p(z_i = 0, j' \in N_j/i)},$$
$$= \beta_{ij} f_j^x \prod_{i' \in N_j/i} r_{i'j}, \tag{2.54}$$

where $\beta_{ij} = 1/(\sum_x f_j^x \prod_{i' \in N_j/i} r_{i'j})$ represents a factor that makes $\sum q_{ij} = 1$.

The updated q_{ij} parameters are substituted in $\mathbf{Q}$ matrix of (2.51) to replace the initial values. Another probabilities are calculated in the vertical step which are called the pseudo posterior probabilities q_{ij}. These probabilities are used to calculate an estimate to the transmitted code word and can be calculated using [52, 50]

$$q_j = \beta_j f_j^x \prod_{i \in N_j} r_{ij}. \tag{2.55}$$

These probabilities are calculated for $x = 0, 1$ and placed in a matrix $\mathbf{Q}'$ to produce an estimate to the transmitted signal, such that [52]

$$\mathbf{Q}' = \begin{bmatrix} q_1^0 & q_2^0 & \cdots & q_j^0 \\ q_1^1 & q_2^1 & \cdots & q_j^1 \end{bmatrix}. \tag{2.56}$$

After several iterations and based on a specific termination condition, the decoded code word is calculated using (2.56). However, if it happens that an error exceeds the code ability, then the termination condition will not satisfied and the decoder will fail to detect and correct the errors [50].

2.9   Chapter Summary

This chapter is dedicated to reviewing briefly the main parts of the communication system that is used in this thesis. In Section 2.2, the frequency-selective Rayleigh fading channel model is illustrated with a block diagram representation of the tapped delay line model. An introduction to the OFDM modulation technique is presented in Section 2.3 with a block diagram representation and some highlights to their applications in eliminating the frequency selectivity of the channels.

The focus of Section 2.4 is to demonstrate the linear and nonlinear MIMO equalization techniques that are used to equalize the channel effect. A general introduction to the coding theory and the FECCs are presented in Section 2.5 with a basic diagram of the coded system. Following that, the recursive and non-recursive convolutional codes are illustrated with the structure of their encoders in Section 2.6 and 2.6.1, respectively. In addition, different decoders for the convolutional codes are described in Section 2.6.2, which includes the Viterbi decoder, the BCJR decoder, the log-MAP decoder and the max log-MAP decoder. Convolutional code's ability is determined by the code constraint length which will specify the complexity of that code.

On the other hand, iterative codes such as turbo codes and LDPC codes have better performance due to the iterative algorithm of their decoders. In Section 2.7, the encoder and the decoder of the turbo codes are illustrated with a definition to the interleaver and the puncture functions. In Section 2.8, a brief introduction to the LDPC codes is introduced, followed by a representation of the parity check matrix and Tanner graph. The encoding and the decoding process of the LDPC codes are described in Sections 2.8.2 and 2.8.3, respectively.

Chapter 3

Improved Coded Massive MIMO OFDM Detection using LLRs Derived from Complex Ratio Distributions

3.1 Introduction

Massive MIMO-OFDM systems are a key technology to achieve high data rate and to improve link reliability in modern wireless communication systems, especially when combined with powerful error control coding techniques such as LDPC codes and turbo codes.

Hence, in the last few years, it has naturally attracted immense research interest. A reduced complexity approach has been used with the Gaussian approximation in [60], where the information of the variable nodes is individually updated in each iteration. A joint detection and decoding of coded LDPC massive MIMO systems using reduced complexity linear programming (LP) has been proposed in [61] by making use of the data and training symbols, the noise subspace and the channel code. This LP receiver was demonstrated to have better performance compared to the existing receivers with robust performance when the pilot symbols are sparsely distributed on the sub-carriers. In [62], a method was proposed that combines irregular LDPC codes with a modulator and a detector in which the variable nodes and the detector nodes were combined in the iterative decoding at the receiver.

Another approach utilizing non-binary LDPC codes for massive MIMO system were used in [63] to achieve the performance of binary LDPC codes with a higher number of antennas and a linear MMSE detector. In [64], a soft MMSE biased detector that uses the Jacobi iterative method was proposed to reduce the complexity of large MIMO detection. This system can provide the post-equalized SINR without iterations and exhibits reduced complexity when using Gray-mapping. However, all of these publications assume that the noise characteristics at the output of the linear MIMO detectors are Gaussian distributed.

The contribution of this chapter can be summarized in the following points,

- The noise PDF for the ZF equalized massive MIMO-OFDM system is derived using Neumann matrix approximation method. The derived PDF is subsequently utilized in the LLR calculations to improve the performance of different coded systems such as LDPC coded and turbo coded massive MIMO-OFDM systems.

- Estimating the complexity required in using the LLR equation based on the exact noise PDF, and a reduced complexity approximation is introduced for this LLR using Newton polynomial interpolation.

- Comparing the performance of turbo coded and LDPC coded massive MIMO-OFDM systems using the Gaussian LLR, exact LLR, and different approximations.

(a) Transmitter.
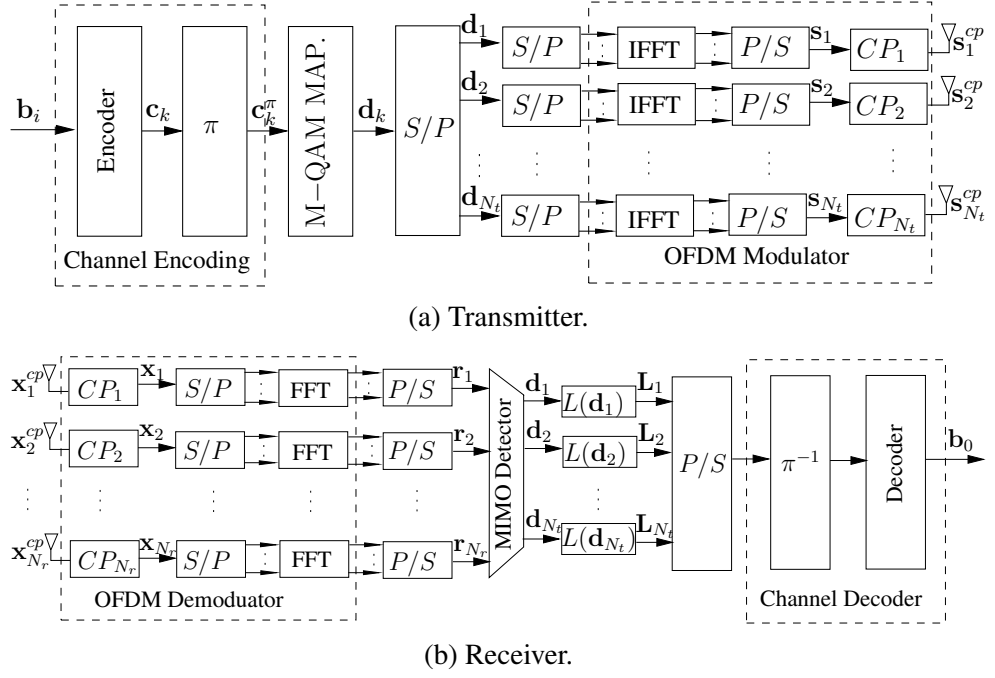
(b) Receiver.

Figure 3.1: Massive MIMO-OFDM system transceiver.

3.2 System Model

An uplink coded massive MIMO-OFDM system is considered here with $N_r \times N_t$ antennas as in Fig. 3.1 with $N_r >> N_t$. The terms N_t and N_r are used here to denote the number of transmitting and receiving antennas, respectively. First, the binary data stream, $\mathbf{b}_i$, is generated and channel encoded to produce the codewords, $\mathbf{c}_k$, which are randomly interleaved, $\mathbf{c}_k^\pi = \Pi(\mathbf{c}_k)$ and modulated using an M-ary quadrature amplitude modulation (M-QAM), i.e. $\mathbf{d}_k = C(\mathbf{c}_k^\pi)$, Π and C represent respectively the interleaving and constellation mapping operators.

Following modulation, a S/P converter splits the modulated symbols into N_t parallel sub-blocks, $\mathbf{d}_l \in \mathbb{C}^{K \times 1}$, where K is the block length of the IFFT used in the OFDM modulators and l is the transmit antenna index. Subsequently, the OFDM waveforms for each transmit antenna are individually constructed, i.e. $\mathbf{s}_l = \mathbf{F}^H \mathbf{d}_l$, where $\mathbf{F} \in \mathbb{C}^{K \times K}$ is the FFT matrix with $f_{m,n} = \frac{1}{\sqrt{K}} e^{-j2\pi \frac{mn}{K}}$ for $m, n = 1, 2, \cdots, K - 1$. To avoid multipath-induced IBI and inter-symbol interference (ISI), a CP is inserted at the start of each block to cover the excess delay spread of the channel, that is

$$\mathbf{s}_l^{cp} = \left[s_{K-K_{cp}}, \ldots, s_{K-1}, s_0, \ldots, s_{K-1} \right]^T, \tag{3.1}$$

where K_{cp} is the length of the cyclic prefix. The transmitted signals propagate through

time-flat, frequency-selective fading channels and are received in the presence of complex zero-mean AWGN of variance σ_w^2. After OFDM demodulation, involving CP removal and the FFT transform at each of the N_r antennas, the received signal vector, $\mathbf{r}_k \in \mathbb{C}^{N_r \times 1}$, for the k-th subcarrier can be written as

$$\mathbf{r}_k = \mathbf{H}_k \mathbf{d}_k + \mathbf{w}_k, \tag{3.2}$$

where $\mathbf{d}_k$ are the transmitted information symbols for the k-th subcarrier across the transmit antennas, $\mathbf{H}_k \in \mathbb{C}^{N_r \times N_t}$ is the channel matrix in the frequency domain, and finally, $\mathbf{w}_k \in \mathbb{C}^{N_r \times 1}$ is the FFT of the time-domain AWGN samples. To detect the transmitted information symbols, a ZFE can be utilized as follows

$$\hat{\mathbf{s}}_k = \mathbf{H}_k^\dagger \mathbf{r}_k = \mathbf{d}_k + \mathbf{H}_k^\dagger \mathbf{w}_k, \tag{3.3}$$

where $\mathbf{H_k}^\dagger$ is the ZFE matrix that can be obtained using the pseudo-inverse of $\mathbf{H_k}$ defined as

$$\mathbf{H}_k^\dagger = \mathbf{G}_k^{-1} \mathbf{H}_k^H, \tag{3.4}$$

and $\mathbf{G}_k = \mathbf{H}_k^H \mathbf{H}_k$ is the symmetric Gram matrix of the channel. A closer examination of the noise term in (3.3) reveals that the ZFE operation affected the distribution of the noise, and the Gaussian assumption can not be used to describe its properties. Therefore, in order to achieve optimal performance in detection, a more accurate noise model is needed.

3.3 Channel Model

In an uplink transmission mode, the transmitter can be considered as the user and the number of the transmitting elements is limited to $N_t = 10$ antennas. On the other hand, the receiver is equipped with hundreds of antennas and represent the base station. This model assumes slow frequency selective fading channel, where the channel parameters are constant during the transmission of each block of data. This channel can be represented as a linear filter with the following impulse response [65, 32]

$$h_{n,l}(t) = \sum_{r=1}^{L_r} \alpha_r \exp(-j\theta_r)\delta(t - \tau) , \qquad (3.5)$$

where, $\delta(\cdot)$ is the Dirac delta function, α_r, θ_r, τ are the channel gain, phase and delay, r is the channel index, L_r is the number of channel paths. Furthermore, $h_{n,l}$ is the channel parameters between the $l-$th transmitter and the $n-$th receiver. The matrix representation of (3.5) can be written as

$$\mathbf{h}(t) = \begin{bmatrix} h_{1,1}(t) & h_{1,l}(t) & \dots & h_{1,N_t}(t) \\ h_{n,1}(t) & h_{n,l}(t) & \dots & h_{n,N_t}(t) \\ \vdots & \vdots & \ddots & \vdots \\ h_{N_r,1}(t) & h_{N_r,l}(t) & \dots & h_{N_r,N_t}(t) \end{bmatrix} . \qquad (3.6)$$

3.4 Neumann-Series Approximation

One of the key issues in the detection using (3.3) is the complexity involved in the computation of the pseudo-inverse of $\mathbf{H}_k$ required for the uplink transmission in massive MIMO systems with a high number of receivers. The aim of Neumann approximation is to obtain a matrix decomposition that results in a diagonally dominant Gram matrix given as [66, 67]

$$\mathbf{A} = \mathbf{D} + \mathbf{E}, \qquad (3.7)$$

where $\mathbf{D}$ is a diagonal matrix composed using the diagonal elements of $\mathbf{A}$. In contrast, $\mathbf{E}$ is composed using the off-diagonal elements of $\mathbf{A}$. The inverse of $\mathbf{A}$ can be written in the form [66]

$$\mathbf{A}^{-1} = \sum_{\iota=0}^{\infty} \left(-\mathbf{D}^{-1}\mathbf{E}\right)^{\iota} \mathbf{D}^{-1} , \qquad (3.8)$$

$$\mathbf{A}^{-1} = \mathbf{D}^{-1} - \left(\mathbf{D}^{-1}\mathbf{E}\right)\mathbf{D}^{-1} + \left(\mathbf{D}^{-1}\mathbf{E}\right)^{2}\mathbf{D}^{-1}\dots . \qquad (3.9)$$

The number of terms selected in (3.9) depends on the value of the index ι, which controls the complexity of the matrix inversion. As N_r goes to ∞, the index value can be set to zero without having a noticeable effect on the inverse of that matrix. For $N_r >> N_t$, the Gram matrix becomes a diagonal dominant matrix, thus, $\iota = 0$ can be used as long as $N_r \geqslant 10N_t$ is satisfied [66].

3.5   Approximate Effective Noise PDF

For large matrices, the Gram matrix becomes diagonally dominant [66, 67]. This property can be exploited to compute the Gram matrix using the Neumann series approximation method to reduce the complexity in calculating the Moore-Penrose pseudo-inverse. In (3.4), $\mathbf{G}_k$ is involved in calculating the ZFE and can be decomposed into two matrices, i.e. $\mathbf{G}_d$, which is composed only of diagonal elements, and $\mathbf{G}_e = \mathbf{G}_k - \mathbf{G}_d$, containing only the off-diagonal elements of $\mathbf{G}_k$. The Neumann matrix inverse for $\mathbf{G}_k$ can be given as [66]

$$\mathbf{G}_k^{-1} = \sum_{\iota=0}^{L} \left(-\mathbf{G}_d^{-1}\mathbf{G}_e\right)^{\iota} \mathbf{G}_d^{-1}. \tag{3.10}$$

The complexity involved in calculating this inverse will depend on L, which controls the number of terms in the summation of (3.10). For massive MIMO systems, that is $N_r \geqslant 10N_t$, an accurate approximation of $\mathbf{G}_k$ can be obtained for $L = 0$, [66]. In this case, the Gram matrix inverse will be reduced to a diagonal matrix inversion, which will simplify the procedure required to find the PDF of $\mathbf{G}_k^{-1}$. As stated in [68], the Neumann series approximation can be used to efficiently rewrite the pseudo inverse equation of the ZFE detector in the following form

$$\mathbf{H}_k^{\dagger} = \mathbf{G}_d^{-1}\mathbf{H}_k^{H}. \tag{3.11}$$

Therefore, the noise term in (3.3) at the output of the ZFE detector becomes

$$\tilde{\mathbf{w}}_k = \mathbf{G}_d^{-1}\mathbf{H}_k^{H}\mathbf{w}_k = \begin{bmatrix} \dfrac{\sum_{n=1}^{N_r} H_{n,1}^{*}(k)w_{n,k}}{\sum_{n=1}^{N_r}|H_{n,1}(k)|^2} \\ \\ \dfrac{\sum_{n=1}^{N_r} H_{n,l}^{*}(k)w_{n,k}}{\sum_{n=1}^{N_r}\left|H_{n,l}(k)\right|^2} \\ \\ \dfrac{\sum_{n=1}^{N_r} H_{n,N_t}^{*}(k)w_{n,k}}{\sum_{n=1}^{N_r}\left|H_{n,N_t}(k)\right|^2} \end{bmatrix}. \tag{3.12}$$

3.5.1   The Gram Matrix Distribution

The Gram matrix $\mathbf{G}_d$ of the MIMO channel $\mathbf{H_k}$ can be written as

$$\mathbf{G_d} = \mathbf{H}_k^H \mathbf{H}_k \,,$$

$$= \begin{bmatrix} \sum_{n=1}^{N_r} |H_{n,1}(k)|^2 & 0 & 0 \\ 0 & \sum_{n=1}^{N_r} |H_{n,l}(k)|^2 & 0 \\ 0 & 0 & \sum_{n=1}^{N_r} |H_{n,N_t}(k)|^2 \end{bmatrix}. \tag{3.13}$$

Each diagonal element has the following form

$$\zeta_{l,k} = \sum_{n=1}^{N_r} |H_{n,l}(k)|^2 = \zeta_{1,l}(k) + \zeta_{2,l}(k) + \cdots + \zeta_{N_r,l}(k), \tag{3.14}$$

where the elements $\zeta_{n,l}(k) = (H_{n,l}^I(k))^2 + (H_{n,l}^Q(k))^2$ are real random variables with 2 degrees of freedom. The characteristic function for these random variables can be written in the form [31]

$$\psi_{\zeta_{n,l,k}}(\omega) = \frac{1}{1 - j2\sigma_H^2 \omega}. \tag{3.15}$$

The distribution for the summation in (3.14) can be represented as N_r convolutions of $\zeta_{n,l}(k)$, which means N_r multiplications in the frequency domain. According to that, the characteristic function and the PDF of (3.14) can be written for the l-th transmit element as [31], [68]

$$\psi_{\zeta_{l,k}}(\omega) = \left(\frac{1}{1 - j2\sigma_H^2 \omega} \right)^{N_r}, \tag{3.16}$$

$$p(\zeta_{l,k}) = \frac{|\zeta_{l,k}|^{N_r - 1}}{(2\sigma_H^2)^{N_r} \Gamma(N_r)} \exp\left(-\frac{|\zeta_{l,k}|}{2\sigma_H^2} \right), \tag{3.17}$$

where, $\zeta_{l,k} = \sum_{n=1}^{N_r} |H_{n,l}(k)|^2$ for $l = 1, 2, \ldots, N_t$ and σ_H^2 is the average variance of $H_{n,l}(k)$. It is worth noting that the mean of $\zeta_{l,k}$ is $\mu_\zeta = 2N_r \sigma_H^2$ and the variance is $\sigma_\zeta^2 = 4N_r \sigma_H^4$ for Chi-Square with $2N_r$ degree of freedom [31]. The mean squared error (MSE) method which can be calculated as $MSE = \sum_k (p(\zeta_{l,k}) - \hat{p}_{l,k})^2 / K$, is used here to calculate the error resulting from the difference between the empirical and theoretical PDFs. In addition, the Kolmogorov-Smirnov (KS) goodness-of-fit test [69] is applied at 5% significance level with the null hypothesis that the two vectors exhibit the same distribution.

Fig. 3.2 a) shows the empirical and theoretical PDFs, i.e. (3.17), for a system with

(a) PDF plot for $p(\zeta_{l,k})$

(b) PDF plot for $p(\lambda^{\nu}_{l,k})$

(c) PDF plot for $p(\alpha^{\nu}_{l,k})$
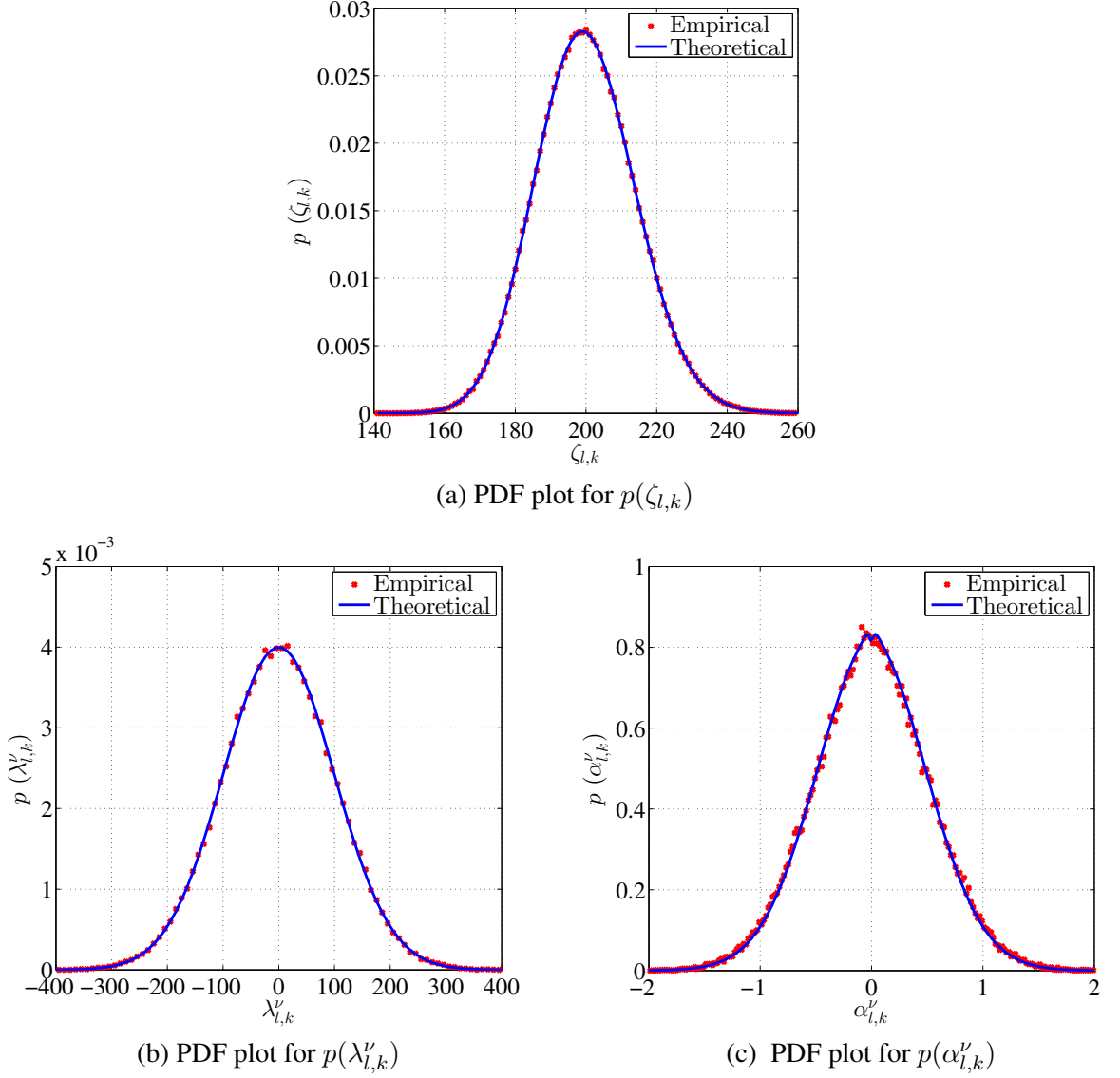
Figure 3.2: Histogram plot of the equalized noise versus the derived PDFs. (a) Plot of (3.17) versus the empirical $P(\zeta_{l,k})$. (b) Plot of (3.23) versus the empirical $P(\lambda^{\nu}_{l,k})$. (C) Plot of (3.37) versus the empirical $P(\alpha^{\nu}_{l,k})$.

$N_t = 10$ and $N_r = 200$ at an SNR of -10 dB demonstrating a very close agreement. In this case, the computed value of the MSE is 9.9176×10^{-9} and the KS test decision is 0 implying that the null hypothesis can not be rejected.

3.5.2 Distribution of the $\mathrm{H}^H W$ Elements

The numerator of (3.12), can be written as

$$
\mathbf{H}_k^H \mathbf{W}_k =
\begin{bmatrix}
H_{1,1}^*(k) & \cdots & H_{n,1}^*(k) & \cdots & H_{N_r,1}^*(k) \\
\vdots & & \vdots & & \vdots \\
H_{1,l}^*(k) & \cdots & H_{n,l}^*(k) & \cdots & H_{N_r,l}^*(k) \\
\vdots & & \vdots & & \vdots \\
H_{1,N_t}^*(k) & \cdots & H_{n,N_t}^*(k) & \cdots & H_{N_r,N_t}^*(k)
\end{bmatrix}
\begin{bmatrix}
w_{1,k} \\
\vdots \\
w_{n,k} \\
\vdots \\
w_{N_r,k}
\end{bmatrix}
$$

$$
=
\begin{bmatrix}
\sum_{n=1}^{N_r} H_{n,1}^*(k) w_{n,k} \\
\vdots \\
\sum_{n=1}^{N_r} H_{n,l}^*(k) w_{n,k} \\
\vdots \\
\sum_{n=1}^{N_r} H_{n,N_t}^*(k) w_{n,k}
\end{bmatrix}
=
\begin{bmatrix}
\lambda_{1,k} \\
\vdots \\
\lambda_{l,k} \\
\vdots \\
\lambda_{N_t,k}
\end{bmatrix} . \tag{3.18}
$$

Each element, $\lambda_{l,k}$ of the vector $\boldsymbol{\lambda}_k = \mathbf{H}_k^H \mathbf{W}_k$ can be given as

$$
\lambda_{l,k} = \sum_{n=1}^{N_r} H_{n,l}^*(k) w_{n,k}, \tag{3.19}
$$

therefore, its inphase (I) and quadrature (Q) components exhibit the following forms, respectively

$$
\lambda_{l,k}^I = \sum_{n=1}^{N_r} H_{n,l}^I(k) w_{n,k}^I + H_{n,l}^Q(k) w_{n,k}^Q, \tag{3.20}
$$

and

$$
\lambda_{l,k}^Q = \sum_{n=1}^{N_r} H_{n,l}^Q(k) w_{n,k}^I - H_{n,l}^I(k) w_{n,k}^Q. \tag{3.21}
$$

As can be seen, $\lambda_{l,k}^I$, $\lambda_{l,k}^Q$ are the result of a sum of products for $2N_r$ independent Gaussian variables. It was shown in [70] that their characteristic function and distribution can be given as

$$
\psi_{\lambda_{l,k}^\nu}(\omega) = \left(\frac{1}{1 + \sigma_H^2 \sigma_w^2 \, \omega^2} \right)^{N_r}, \tag{3.22}
$$

$$
p(\lambda_{l,k}^\nu) = \frac{\exp(\frac{-|\lambda_{l,k}^\nu|}{\sigma_H \sigma_w})}{\Gamma(N_r) \, \sigma_H \sigma_w} \sum_{n=1}^{N_r} \frac{(N_r + n - 2)!}{(N_r - n)! \, 2^{N_r + n - 1} \, \Gamma(n)} \left(\frac{|\lambda_{l,k}^\nu|}{\sigma_H \sigma_w} \right)^{N_r - n}, \tag{3.23}
$$

where $\nu = \{I, Q\}$. By taking the statistical expectation of (3.20) and (3.21), it can easily be shown that the mean value of this PDF is zero, i.e. $\mu_\lambda = 0$, and its variance can be theoretically computed as

$$
\begin{aligned}
\sigma_\lambda^2 &= \int_{-\infty}^{\infty} \lambda^2 \, p(\lambda) d\lambda \, , \\
&= \sum_{n=1}^{N_r} \frac{\Gamma(N_r + n - 1) \int_0^\infty \lambda^{N_r - n + 2} \exp(\frac{-\lambda}{\sigma_H \sigma_w}) d\lambda}{\Gamma(N_r)\Gamma(N_r - n + 1)\Gamma(n)2^{(Nr+n-2)}} \, , \\
&= \sum_{n=1}^{N_r} \frac{\Gamma(N_r - n + 3)\Gamma(N_r + n - 1)(\sigma_H \, \sigma_w)^2}{\Gamma(N_r)\Gamma(N_r - n + 1)\Gamma(n)2^{(Nr+n-2)}} \, .
\end{aligned}
\tag{3.24}
$$

The empirical PDF of $\lambda_{l,k}^\nu$ and its theoretical PDF given in (3.23) demonstrate a very close agreement as shown in Fig. 3.2 b). The computed value of MSE is 8.874×10^{-10} and the KS test decision is 0 implying that the null hypothesis can not be rejected.

3.5.3 Independence Verification

To prove that the two random variables $\lambda_{l,k}^\nu$ and $\zeta_{l,k}$ are independent, the following points will be considered. First, based on the central limit theorem (CLT), the i.i.d. random variables $X_1, X_2, \dots X_n$ with mean μ and variance $\sigma^2 < \infty$ can be written as

$$
S_n = \frac{1}{\sigma\sqrt{n}} \sum_{i=1}^n (X_i - \mu) \, .
\tag{3.25}
$$

Based on the CLT and for large n, the distribution of $\bar{X}_n$ can approximately be considered as normal distribution with mean μ and variance $\frac{\sigma^2}{n}$ [71, 72]. As stated in [73], as long as the value $n > 10$, the distribution of S_n approaches the normal distribution.

According to that, and since $N_r \geq 100$, the PDF of the real and imaginary parts of $\lambda_{l,k} = \sum_{n=1}^{N_r} H_{n,l}^*(k)w_{n,k}$, can be written in the form of a normal distribution with $N(0, \sigma_\lambda^2)$ as

$$
p(\lambda_{l,k}^\nu) = \frac{1}{\sqrt{2\pi\sigma_\lambda^2}} \exp(-\frac{\lambda_{l,k}^{\nu\,2}}{2\sigma_\lambda^2}).
\tag{3.26}
$$

Similarly, the PDF of $\zeta_{l,k} = \sum_{n=1}^{N_r} |H_{n,l}(k)|^2$ for large N_r, can be written as $N(\mu_\zeta, \sigma_\zeta^2)$

$$
p(\zeta_{l,k}) = \frac{1}{\sqrt{2\pi\sigma_\zeta^2}} \exp(-\frac{(\zeta_{l,k} - \mu_\zeta)^2}{2\sigma_\zeta^2}),
\tag{3.27}
$$

where the theoretical values of $\sigma_\lambda^2, \mu_\zeta, \sigma_\zeta^2$ are calculated in Sections 3.5.1 and 3.5.2, re-

(a) Plot of $p(\lambda)$ and $N(\mu_\lambda, \sigma_\lambda)$.

(b) Plot of $p(\zeta)$ and $N(\mu_\zeta, \sigma_\zeta)$.
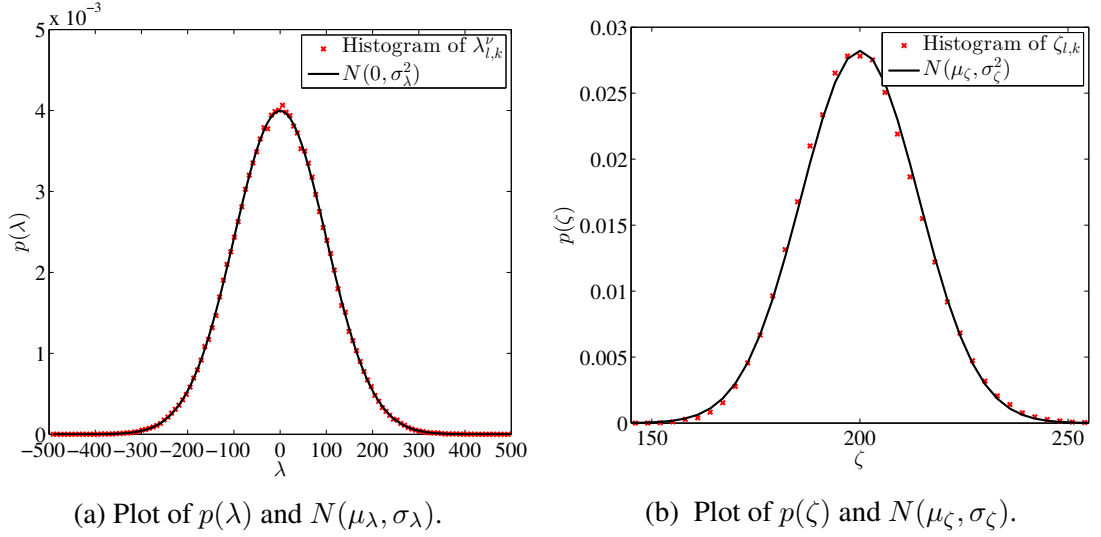
Figure 3.3: The PDF of $\zeta_{l,k}$ and $\lambda_{l,k}^\nu$ for massive MIMO-OFDM systems at $N_t = 10$ and $N_r = 200$.

spectively. Fig. 3.3 shows the histogram plot of ζ and λ compared to its equivalent Gaussian PDF.

Second, based on this large N_r assumption, the two Gaussian random variables will be independent if their covariance is zero. Thus, the covariance of $\zeta_{l,k}$ and $\lambda_{l,k}^\nu$, $c_{\zeta\lambda}$ will be calculated to prove they are independent random variables. $c_{\zeta\lambda}$ is computed as

$$
\begin{aligned}
c_{\zeta\lambda} &= E\{(\zeta_{l,k} - \mu_\zeta)\lambda_{l,k}\} \,, \\
&= E\{\zeta_{l,k}\lambda_{l,k}\} - \mu_\zeta E\{\lambda_{l,k}\} \,.
\end{aligned}
\tag{3.28}
$$

Since $E\{\lambda_{l,k}\} = 0$, the covariance of (3.28) can be written as

$$
\begin{aligned}
c_{\zeta\lambda} &= E\{\zeta_{l,k}\lambda_{l,k}\} \,, \\
&= E\left\{ \sum_{n=1}^{N_r} |H_{n,l}(k)|^2 \sum_{m=1}^{N_r} H_{m,l}^*(k)w_{m,k} \right\} \,.
\end{aligned}
\tag{3.29}
$$

By expanding the inner sum

$$
\begin{aligned}
c_{\zeta\lambda} = E\{ & \sum_{n=1}^{N_r} |H_{n,l}(k)|^2 H_{1,l}^*(k)w_{1,k} + \sum_{n=1}^{N_r} |H_{n,l}(k)|^2 \times \\
& H_{2,l}^*(k)w_{2,k} + \ldots + \sum_{n=1}^{N_r} |H_{n,l}(k)|^2 H_{N_r,l}^*(k)w_{N_r,k} \} \,,
\end{aligned}
\tag{3.30}
$$

and expanding the outer sum

$$c_{\zeta\lambda} = E\{|H_{1,l}(k)|^2 H_{1,l}^*(k)w_{1,k} + |H_{1,l}(k)|^2 H_{2,l}^*(k)w_{2,k}$$

$$+ \ldots + |H_{1,l}(k)|^2 H_{N_r,l}^*(k)w_{N_r,k} + |H_{2,l}(k)|^2 \times$$

$$H_{1,l}^*(k)w_{1,k} + |H_{2,l}(k)|^2 H_{2,l}^*(k)w_{2,k} + \ldots +$$

$$|H_{2,l}(k)|^2 H_{N_r,l}^*(k)w_{N_r,k} + \ldots + |H_{N_r,l}(k)|^2 H_{N_r,l}^*(k)w_{N_r,k}\}. \qquad (3.31)$$

Since the channel parameters and the AWGN are independently distributed, (3.31) can be written as

$$c_{\zeta\lambda} = E\{|H_{1,l}(k)|^2 H_{1,l}^*(k)\}E\{w_{1,k}\} + E\{|H_{1,l}(k)|^2 H_{2,l}^*(k)\}E\{w_{2,k}\} + \ldots +$$

$$E\{|H_{1,l}(k)|^2 H_{N_r,l}^*(k)\}E\{w_{N_r,k}\} + \ldots + E\{|H_{N_r,l}(k)|^2 H_{N_r,l}^*(k)\}E\{w_{N_r,k}\}.$$

$$(3.32)$$

The AWGN has zero mean which makes the term $E\{w_{m,k}\} = 0$, and the covariance $c_{\zeta\lambda} = 0$.

In addition, the following tests have been applied to verify the independent property of the two random variables $\lambda_{l,k}^\nu, \zeta_{l,k}$.

- The histogram plot in Fig. 3.3 shows close match between the empirical and the theoretical PDFs.

- The Chi-square test of independency [69] is performed based on the `crosstab(x1,x2)` function in Matlab. This test shows that the probability of statistics is 0.2397, which indicates that the null hypothesis that is the two random variables are independent cannot be rejected.

- The Kolmogorov-Smirnov test [69] is performed based on modifying the `kstest2(x1,x2)` function in Matlab to compare the empirical and the theoretical PDFs instead of the random variables. The decision on equality test between the theoretical and the empirical PDFs was (H=0) which implies that the null hypothesis that is the two random variables exhibit the same PDF cannot be rejected.

3.5.4 Ratio Distribution

The real and imaginary parts of the noise equation (3.12) have similar PDFs, and hence, a general equation will be derived to represent both parts. First, the noise equation at the

output of the MIMO detector can be written as

$$
\begin{bmatrix} \frac{1}{\zeta_{1,k}} & 0 & 0 \\ 0 & \frac{1}{\zeta_{l,k}} & 0 \\ 0 & 0 & \frac{1}{\zeta_{N_t,k}} \end{bmatrix} \begin{bmatrix} \lambda^{\nu}_{1,k} \\ \lambda^{\nu}_{l,k} \\ \lambda^{\nu}_{N_t,k} \end{bmatrix} = \begin{bmatrix} \frac{\lambda^{\nu}_{1,k}}{\zeta_{1,k}} \\ \frac{\lambda^{\nu}_{l,k}}{\zeta_{l,k}} \\ \frac{\lambda^{\nu}_{N_t,k}}{\zeta_{N_t,k}} \end{bmatrix} = \begin{bmatrix} \alpha^{\nu}_{1,k} \\ \alpha^{\nu}_{l,k} \\ \alpha^{\nu}_{N_t,k} \end{bmatrix}. \tag{3.33}
$$

The joint probability for $\lambda^{\nu}_{l,k}$ and $\zeta_{l,k}$ can then be written as [68]

$$
p(\lambda^{\nu}_{l,k}, \zeta_{l,k}) = p(\lambda^{\nu}_{l,k})p(\zeta_{l,k}) = \frac{|\zeta_{l,k}|^{N_r-1} \exp\left(-\frac{|\zeta_{l,k}|}{2\sigma_H^2}\right)}{(2\sigma_H^2)^{N_r}\Gamma(N_r)} \times
$$
$$
\sum_{n=1}^{N_r} \frac{\exp\left(\frac{-|\lambda^{\nu}_{l,k}|}{\sigma_H\sigma_w}\right)\Gamma(N_r+n-1)\left|\lambda^{\nu}_{l,k}\right|^{N_r-n}}{(N_r-n)!\,2^{N_r+n-1}\Gamma(n)\sigma_H\sigma_w^{N_r-n}\Gamma(N_r)}, \tag{3.34}
$$

and the substitution of $\lambda^{\nu}_{l,k} = \zeta_{l,k}\alpha^{\nu}_{l,k}$ in this equation will result in

$$
p(\alpha^{\nu}_{l,k}\zeta_{l,k}, \zeta_{l,k}) = \sum_{n=1}^{N_r} A_n \exp\left(-\beta\,|\zeta_{l,k}|\right)|\zeta_{l,k}|^{2N_r-n-1}, \tag{3.35}
$$

where A_n and β are equal to

$$
A_n = \frac{\left|\alpha^{\nu}_{l,k}\right|^{N_r-n}(N_r+n-2)!(\sigma_H\sigma_w)^{n-N_r-1}}{\Gamma^2(N_r)(2\sigma_H^2)^{N_r}(N_r-n)!\,2^{N_r+n-1}\Gamma(n)},
$$

$$
\beta = \frac{\sigma_w + 2\sigma_H\left|\alpha^{\nu}_{l,k}\right|}{2\sigma_w\sigma_H}.
$$

Now, to find the noise PDF, this equation must be integrated w.r.t $\zeta_{l,k}$ as [68, 74]

$$
p(\alpha^{\nu}_{l,k}) = \int_{-\infty}^{\infty} |\zeta_{l,k}|\,p(\alpha^{\nu}_{l,k}\zeta_{l,k}, \zeta_{l,k})d\zeta_{l,k}, \tag{3.36}
$$

$$
p(\alpha^{\nu}_{l,k}) = \sum_{n=1}^{N_r} \frac{(N_r+n-2)!(2N_r-n)!(\frac{\sigma_w}{2\sigma_H})^{N_r}\left|\alpha^{\nu}_{l,k}\right|^{N_r-n}}{2^{N_r+n-1}\Gamma^2(N_r)(N_r-n)!\Gamma(n)(\left|\alpha^{\nu}_{l,k}\right| + \frac{\sigma_w}{2\sigma_H})^{2N_r-n+1}}. \tag{3.37}
$$

The mean value of this PDF is zero and its variance is given as

$$
\sigma^2_{\alpha_t} = \sum_{n=1}^{N_r} \frac{\Gamma(N_r-n+3)\Gamma(N_r+n-1)\Gamma(N_r-2)\left(\frac{\sigma_w}{\sigma_H}\right)^2}{\Gamma^2(N_r)\Gamma(N_r-n+1)\Gamma(n)2^{(N_r+n)}}. \tag{3.38}
$$

To verify the accuracy of this PDF, a comparison between the histogram plot of the actual

Imaj

0010   0110   1110   1010
 •   •   •   •

2j

0011   0111   1111   1011
 •   •   •   •

−2   2
←──────────────────────────────→ Real

0001   0101   1101   1001
 •   •   •   •

−2j

0000   0100   1100   1000
 •   •   •   •
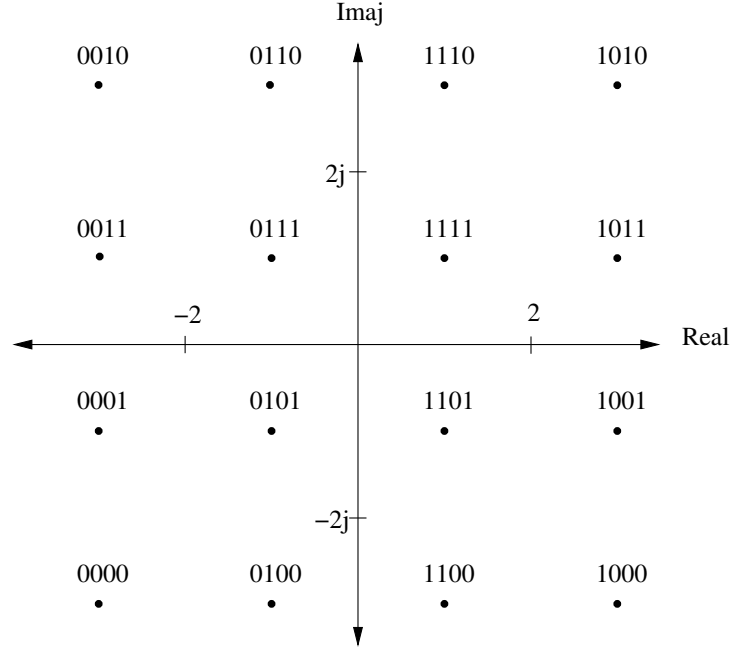
Figure 3.4: 16-QAM constellation map.

noise PDF and this equation is given in Fig. 3.2 c). A close inspection of the figure reveals that the empirical PDF of $\alpha_{l,k}^{\nu}$ and its theoretical PDF given in (3.37) are closely matched. The computed MSE is 2.076×10^{-5}, while the KS test decision is 0 verifying the validity of the null hypothesis.

Using the PDF in (3.37) describing the noise characteristics after ZFE, the LLRs of the coded massive MIMO-OFDM systems are obtained and the performance of the LDPC coded and turbo coded systems is compared to the performance of the systems with Gaussian PDF based LLR.

3.6 LLR Calculation

The output of the ZFE in (3.3) is utilized to calculate the LLR equations required for soft decoding with 4-QAM scheme, which are given as

$$L(b_0) = \log_e \left(\frac{p(\alpha_{l,k}^I | s_{l,k}^I = 1)}{p(\alpha_{l,k}^I | s_{l,k}^I = -1)} \right), \tag{3.39}$$

$$L(b_1) = \log_e \left(\frac{p(\alpha_{l,k}^Q | s_{l,k}^Q = 1)}{p(\alpha_{l,k}^Q | s_{l,k}^Q = -1)} \right). \tag{3.40}$$

where the superscripts I and Q denoted the in-phase and quadrature parts of complex-valued signals, respectively, as in (3.20) and (3.21).

The point representation of the constellation map in Fig. 3.4 can be written as (b_0, b_1, b_2, b_3), where the LLR of the first two bits b_0, b_1 are functions of the real part of the equalized received signal while the last two bits b_2, b_3 are functions of the imaginary part. The LLR equations for the 16-QAM scheme can be written based on the constellation map of Fig. 3.4 as

$$L(b_0) = \log_e \left(\frac{p(\alpha_{l,k}^I | s_{l,k}^I = 1)}{p(\alpha_{l,k}^I | s_{l,k}^I = -1)} \right),$$

(3.41)

$$L(b_1) \approx min \left(\log_e \left(\frac{p(\alpha_{l,k}^I | s_{l,k}^I = -1)}{p(\alpha_{l,k}^I | s_{l,k}^I = -3)} \right), \log_e \left(\frac{p(\alpha_{l,k}^I | s_{l,k}^I = 1)}{p(\alpha_{l,k}^I | s_{l,k}^I = 3)} \right) \right),$$

(3.42)

$$L(b_2) = \log_e \left(\frac{p(\alpha_{l,k}^Q | s_{l,k}^Q = 1)}{p(\alpha_{l,k}^Q | s_{l,k}^Q = -1)} \right),$$

(3.43)

$$L(b_3) \approx min \left(\log_e \left(\frac{p(\alpha_{l,k}^Q | s_{l,k}^Q = -1)}{p(\alpha_{l,k}^Q | s_{l,k}^Q = -3)} \right), \log_e \left(\frac{p(\alpha_{l,k}^Q | s_{l,k}^Q = 1)}{p(\alpha_{l,k}^Q | s_{l,k}^Q = 3)} \right) \right).$$

(3.44)

3.6.1 LLR Approximation

A reduced complexity approach can be used to simplify the soft bit calculations evaluated based on this PDF [62] by approximating the LLR values, without affecting the system performance. The polynomial interpolation is used to approximate the LLR equations by a low order polynomial [75, 76]. Newton's polynomial interpolation is an approximation method that gives good interpretation to the original function using [77, 75, 76]

$$f_n(x) = a_0 + a_1(x - x_0) + a_2(x - x_0)(x - x_1) + \cdots$$
$$+ a_n(x - x_0)(x - x_1) \times \cdots \times (x - x_n),$$

(3.45)

where the coefficients, $a_0 = y(x_0)$, $a_1 = y(x_0, x_1)$, $a_2 = y(x_0, x_1, x_2)$, $\cdots$, $a_n = y(x_0, x_1, x_2, \cdots, x_n)$, can be calculated in a forward procedure using

$$y(x_i, x_j) = \frac{y(x_i) - y(x_j)}{x_i - x_j}, \tag{3.46}$$

and the forward interpolation procedure illustrated in Algorithm 2 is used to calculate the approximated LLR polynomial.

Algorithm 2 : Newton polynomial interpolation [77]

1: **procedure** $C = pinterp(x, y)$
2:     set $n = length(x)$
3:     set $w = Zeros(n, n)$
4:     set $first\ column\ w_1 = y$
5:     **for** $j \leftarrow 2\ to\ n$ **do**
6:         **for** $(k \leftarrow j\ to\ n)$ **do**
7:             $w_{k,j} = (w_{k,j-1} - w_{k-1,j-1})/(x_k - x_{k-j+1})$
8:         **end for**
9:     **end for**
10:     set $C = w_{n,n}$
11:     **for** $k \leftarrow (n-1)\ to\ 1\ by\ -1$ **do**
12:         $C = conv(C, poly(x(k)))$
13:         $m = length(C)$
14:         $C_m = C_m + w_{k,k}$
15:     **end for**

For 4-QAM, the real and imaginary parts of the received symbols after ZFE are scaled in the range -2.5 to 2.5 with 4 points distributed as $\{-2.5, -1.25, 1.25, 2.5\}$. Subsequently, the evaluation procedure starts by calculating the Newton table that will be used to determine the polynomial coefficients. By applying the regression procedure, the equivalent LLR equation for the selected example will then be written as

$$L(x) = \sum_{\rho=0}^{N_x} a_\rho x^\rho, \tag{3.47}$$

where values of a_ρ parameters are listed in Table 3.1 and N_x is the polynomial order. Similarly for the 16-QAM scheme, the real and imaginary parts of the received symbols

Table 3.1: a_ρ parameters for LLR approximation with BPSK/4-QAM scheme.

N_r	a_0	a_1	a_2	a_3
100 3rd order	0	4.02502	0	-0.1275
100 1st order	0	3.2524	0	0
150 3rd order	0	4.1269	0	-0.1027
150 1st order	0	3.485	0	0
200 3rd order	0	4.27	0	-0.0842
200 1st order	0	3.4441	0	0

after the ZFE are scaled in the range -7 to 7 with 7 points distributed as $\{-7, -4.5, -1.5, 0, 1.5, 4.5, 7\}$. Based on that, the equivalent a_ρ parameters for (3.47) are shown in Table 3.2.

Table 3.2: a_ρ parameters for LLR approximation with 16-QAM scheme.

N_r	b_i	a_0	a_1	a_2	a_3	a_4	a_5	a_6
	b_0/b_2	0	1.7949	0	-0.03	0	2.7×10^{-4}	0
100	b_1/b_3	3.329	0	-1.199	0	0.056	0	-7.2×10^{-4}
	b_0/b_2	0	1.701	0	-0.021	0	1.2×10^{-4}	0
150	b_1/b_3	3.219	0	-1.242	0	0.064	0	-8.7×10^{-4}
	b_0/b_2	0	1.789	0	-0.017	0	1.2×10^{-4}	0
200	b_1/b_3	3.428	0	-1.253	0	0.058	0	-7.7×10^{-4}

This approximation will reduce the complexity of the exact LLR as shown in Table 3.3, where N_x is selected to obtain 1st and 3rd order polynomials for the BPSK/4QAM schemes and 6-th order polynomial for the 16-QAM scheme. The plot of the actual LLR equation versus (3.47) is demonstrated in Fig. 3.5 for both approximated LLRs.

3.6.2 Complexity Calculation

When the number of receiving antennas is relatively high in massive MIMO systems, the LLR calculations using the PDF of (3.37) will exhibit higher complexity compared to other approximated PDF approaches such as the Gaussian distribution. However, the utilization of the proposed LLRs based on the newly derived PDF results in a significant performance improvement.

The $gaxpy$ operation approach found in [40] is used here to determine the number of operations required in calculating (3.37), (3.39), (3.40) and (3.47) as shown in Table 3.3. The number of operations required to calculate the exact PDF depends mainly on N_r, whereas using the Gaussian PDF in calculating the LLRs is limited to few multiplications which is equivalent to the proposed approximation using the Newton interpolation.

Table 3.3: Operations required per symbol.

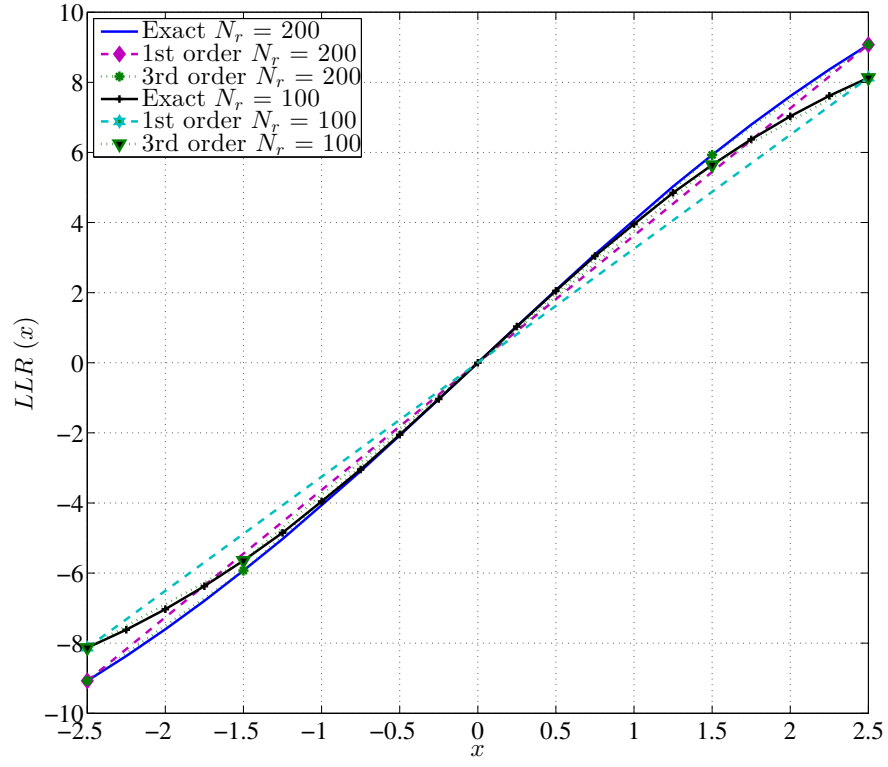| Equation	Division	Addition	Subtract	Multiplication
Eq. (3.37)	$2N_r + 2$	$2N_r$	$6N_r + 1$	$8{N_r}^2 + 3N_r - 2$
LLR Neumann	$4N_r + 1$	$4N_r$	$12N_r$	$16{N_r}^2 - 2N_r$
LLR Gaussian BPSK/4QAM	2	0	0	2
LLR App. 1st BPSK/4QAM	0	0	0	1
LLR App. 3rd BPSK/4QAM	0	0	1	4
LLR Gaussian 16-QAM	6	2	2	6
LLR App. 16-QAM	0	4	11	42

(a) BPSK and 4-QAM $N_r = 100, 200$
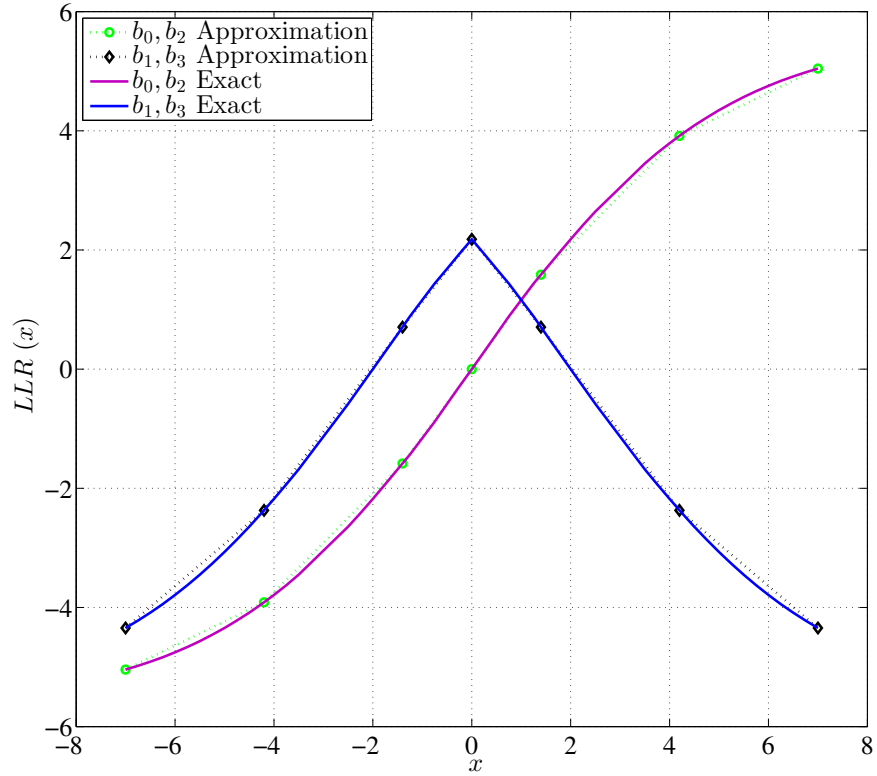
(b) 16-QAM scheme $N_r = 100$

Figure 3.5: Plot of exact and approximate LLR for a system with $N_t = 10$ and different receive antennas at, (a) BPSK and 4-QAM, (b) 16-QAM scheme.
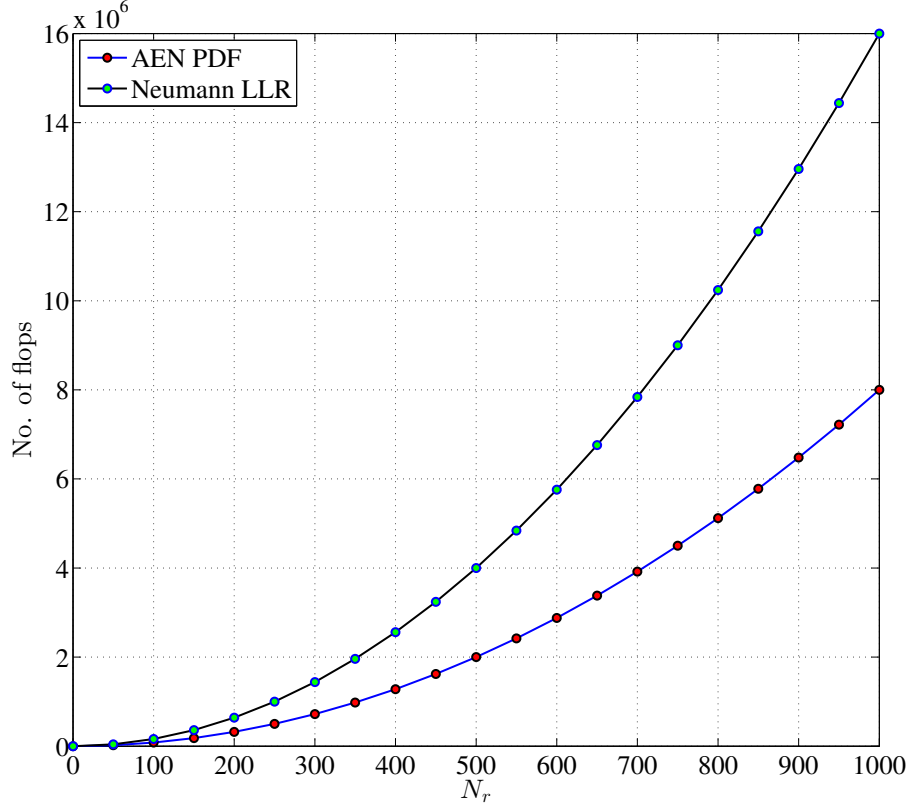
Figure 3.6: Number of flops required to calculate the LLR using the exact PDF.

The floating point operation (FLOP) counts of the *gaxpy* approach weights higher the most nested operations rather than the exact complexity [40]. Based on that, Fig. 3.6 shows the effect of increasing N_r on the total complexity, assuming that the number of flops required to calculate (3.37) is $O(8N_r^2)$, and for the exact LLR is $O(16N_r^2)$.

3.7 Simulation and Results

In this section, improving the performance of the coded massive MIMO-OFDM systems using LLRs equations based on the newly derived PDF will be considered and compared to the performance of the commonly used Gaussian assumption [60, 61, 62]. The scenario of this chapter has the following specifications, the number of transmit antennas is in the range $N_t = 4, 10$ and the number of receive antennas' range is $N_r = 100, 150, 200$ as shown in Figs. 3.7 and 3.9 for the LDPC coded systems and Figs. 3.8 and 3.10 for the turbo coded systems. The length of FFT block utilized is 1024 symbols, the block length of the 1/2 rate Extended Irregular Repeat-Accumulate (eIRA) LDPC code is 64800 bits that are randomly interleaved after encoding. The LLR equations are calculated for the

real and the imaginary parts of the recovered N_t signals by substituting (3.37) in (3.39) and (3.40) for the real and imaginary parts of the 4-QAM and in (3.41)-(3.44) for the 16-QAM, respectively.

The transmitted signals propagate through time-flat, frequency-selective Rayleigh fading channels with 6 multipath arrivals and a delay spread of maximum 85 samples and are received in the presence of complex zero-mean AWGN of variance σ_w^2.

The behavior of LLR equations can be illustrated based on Fig. 3.5 and the constellation map of Fig. 3.4. It is observed that the LLR for b_0 and b_2 are increasing for the positive and negative values of x because the transition in the constellation map of Fig. 3.4 is from 0 to 1. However, in the case of b_1 and b_3, the transition from 0 to 1 was in the negative interval of x only, while the transition has inverted in the positive region to become from 1 to 0 which result in a reduction in the LLR calculation for b_1 and b_3.

A closer look at Figs. 3.7a) and 3.7b) at $BER = 10^{-4}$ reveals that the performance of the LDPC coded systems with the proposed LLRs has improved by 2 dB compared to the Gaussian based LLRs for the BPSK/4-QAM schemes. While the improvement for the 16-QAM coded system was 1 dB as shown in Figs 3.9a) and 3.9b).

Furthermore, using the LLR equations based on the newly derived PDF has improved the BER performance of the turbo coded massive MIMO-OFDM system with BPSK/4-QAM scheme by 0.8~1 dB at 10^{-4} BER as illustrated in Figs. 3.8a) and 3.8b). While this improvement has reduced to 0.6 dB for the 16-QAM turbo coded as shown in Figs 3.10a) and 3.10b), respectively.

The number of operations required in calculating the LLRs for the coded system using the newly derived PDF is compared to the Gaussian based LLR and the result is shown in Table 3.3. It can be observed that calculating the LLR with the exact PDF will exhibit higher operations than the Gaussian PDF. To reduce the cost of using this LLR, Newton's interpolation method have been used to rewrite this equation as a linear polynomial of different orders. According to the results shown in Figs. 3.8a) and 3.8b), the first order approximation has successfully matched the BER performance of the turbo coded system with BPSK/4-QAM scheme for the derived LLR and reduced the complexity to one multiplication as shown in Table 3.3, while the approximation for the LLRs of the 16-QAM scheme required 5-th and 6-th order polynomials to match the exact performance. On the other hand, Figs. 3.7a) and 3.7b) show that the third order approximation can successfully match the performance of the LDPC coded systems with BPSK/4-QAM scheme, while the first order approximation reduces the performance by 0.3 dB. The approximation of

(a) $N_t = 4$

(b) $N_t = 10$

Figure 3.7: Simulation of the LDPC coded massive MIMO-OFDM system rate $1/2$ with BPSK/4-QAM and $N_r = 100; \ 150; \ 200$ for, (a) $N_t = 4$ (b) $N_t = 10$.

(a) $N_t = 4$

(b) $N_t = 10$

Figure 3.8: Simulation of the turbo coded massive MIMO-OFDM system rate $1/3$ with $(561; 753)_8$ polynomial generator, BPSK/4-QAM, and $N_r = 100; 150; 200$ for, (a) $N_t = 4$ (b) $N_t = 10$.

(a) $N_t = 4$

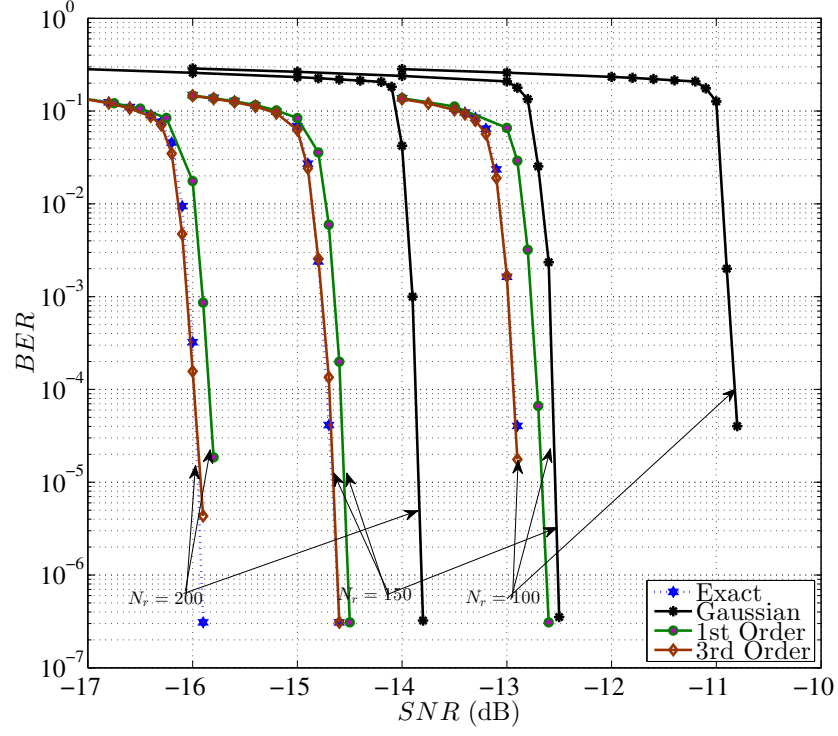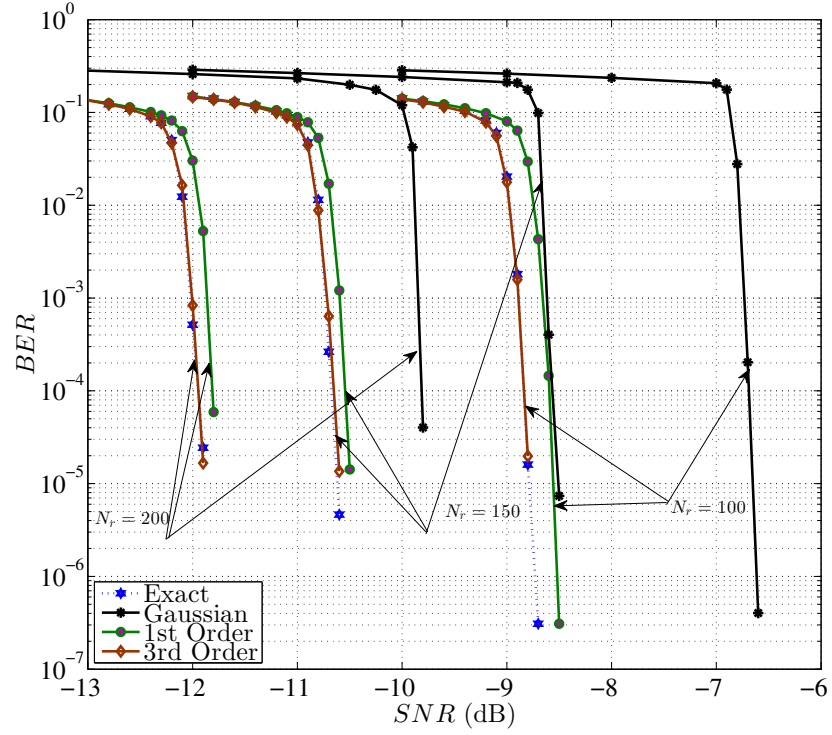

(b) $N_t = 10$

Figure 3.9: Simulation of the LDPC coded massive MIMO-OFDM system rate $1/2$ with 16-QAM and $N_r = 100;\ 150;\ 200$ for, (a) $N_t = 4$ (b) $N_t = 10$.
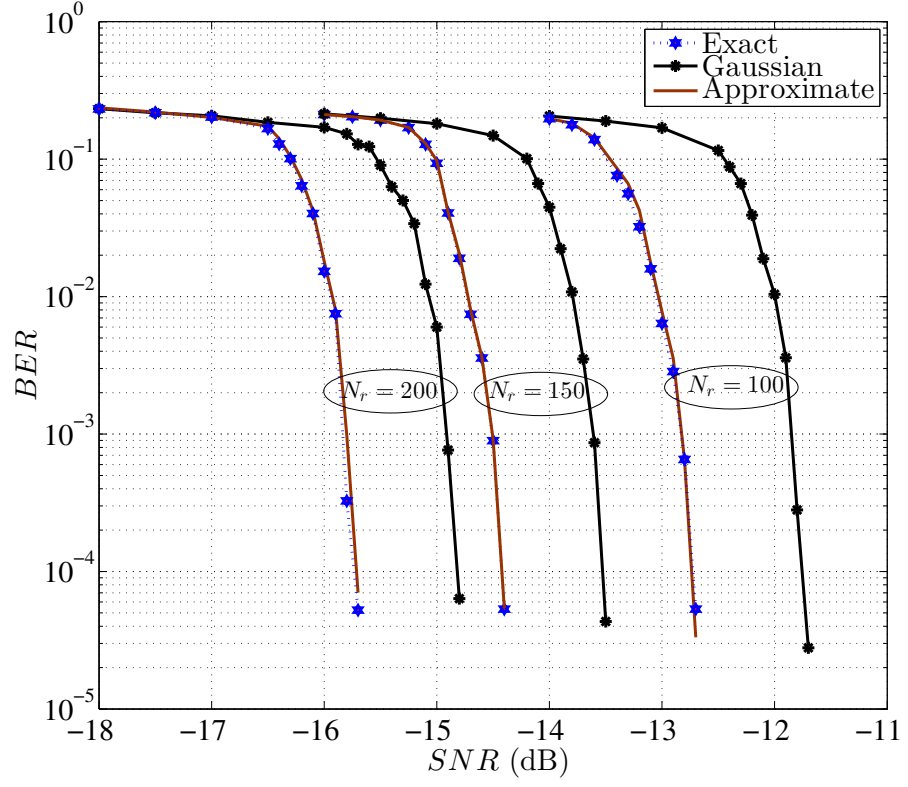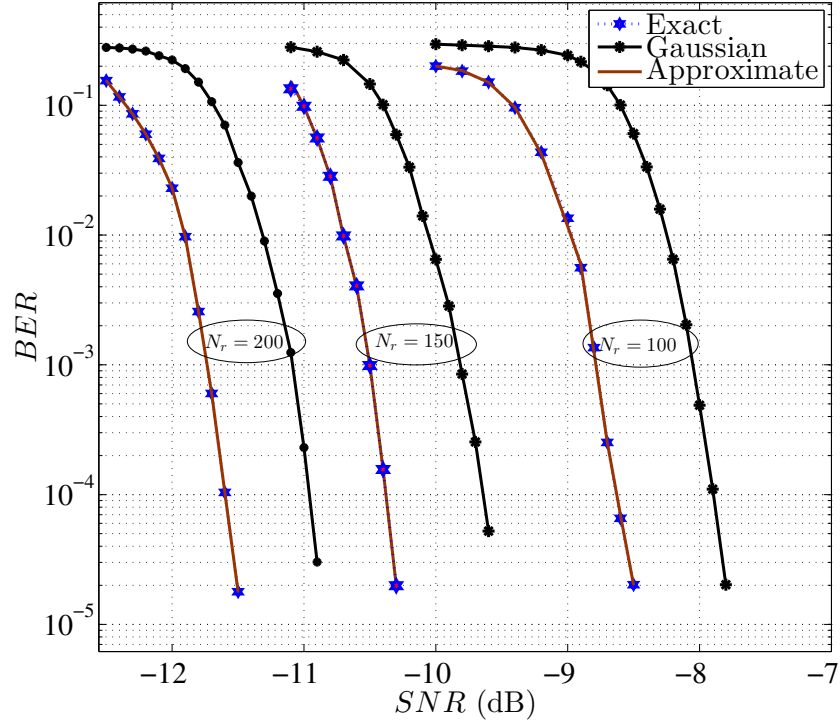
(a) $N_t = 4$

(b) $N_t = 10$

Figure 3.10: Simulation of the turbo coded massive MIMO-OFDM system rate $1/3$ with $(561; 753)_8$ polynomial generator, 16-QAM, and $N_r = 100; \ 150; \ 200$ for, (a) $N_t = 4$ (b) $N_t = 10$.
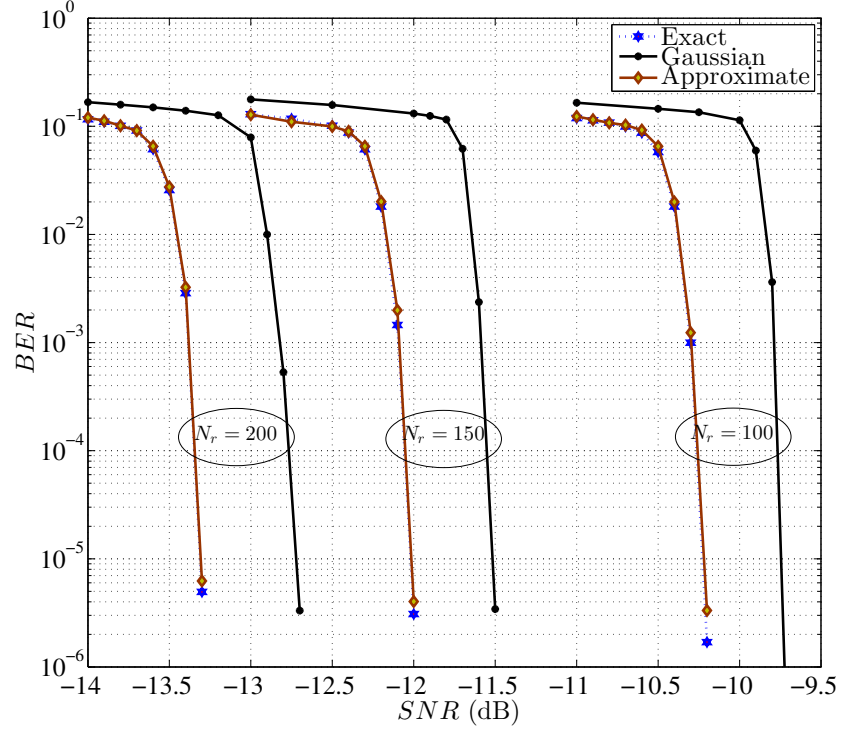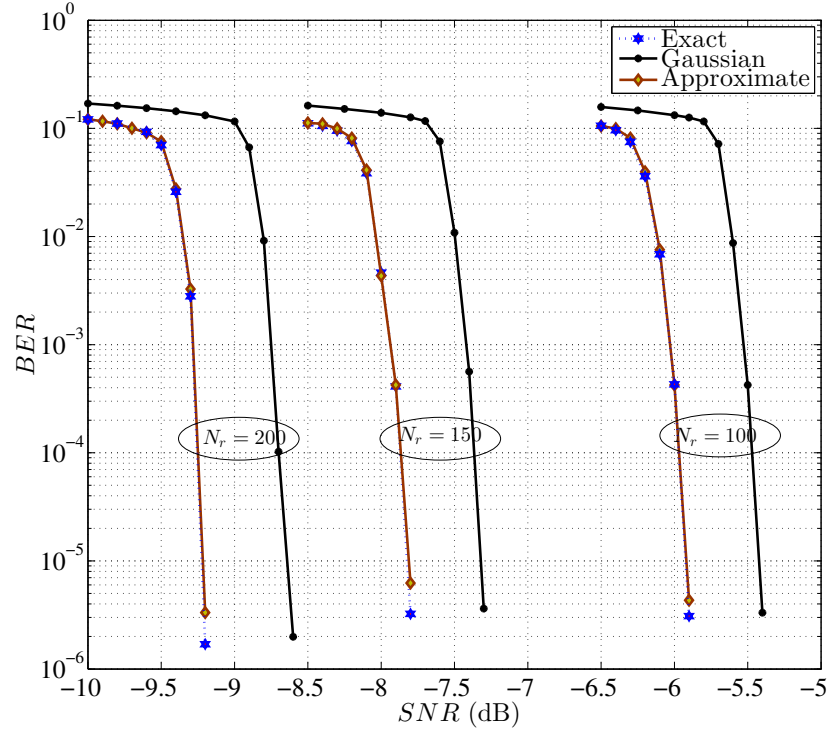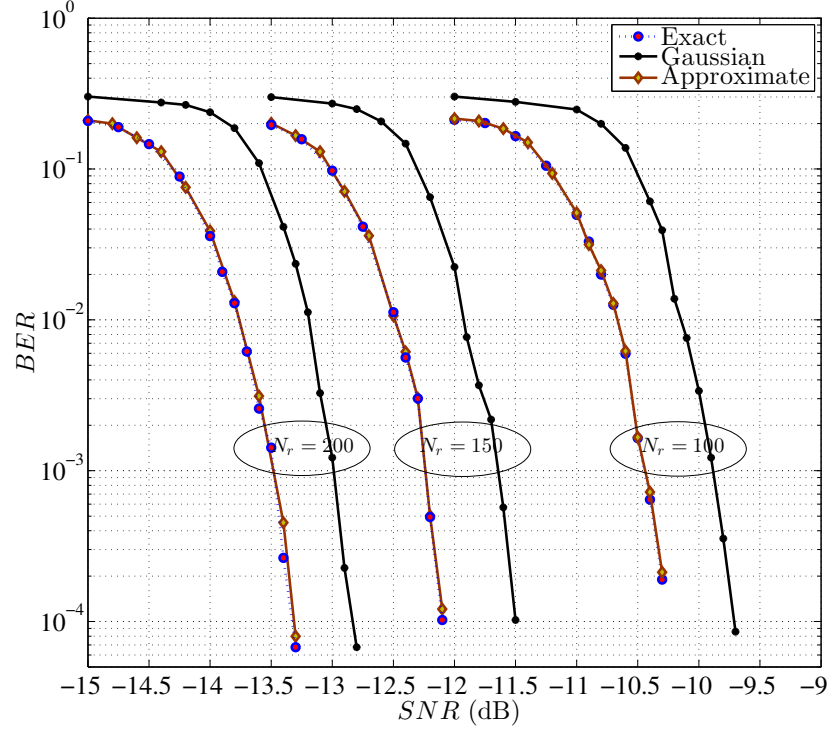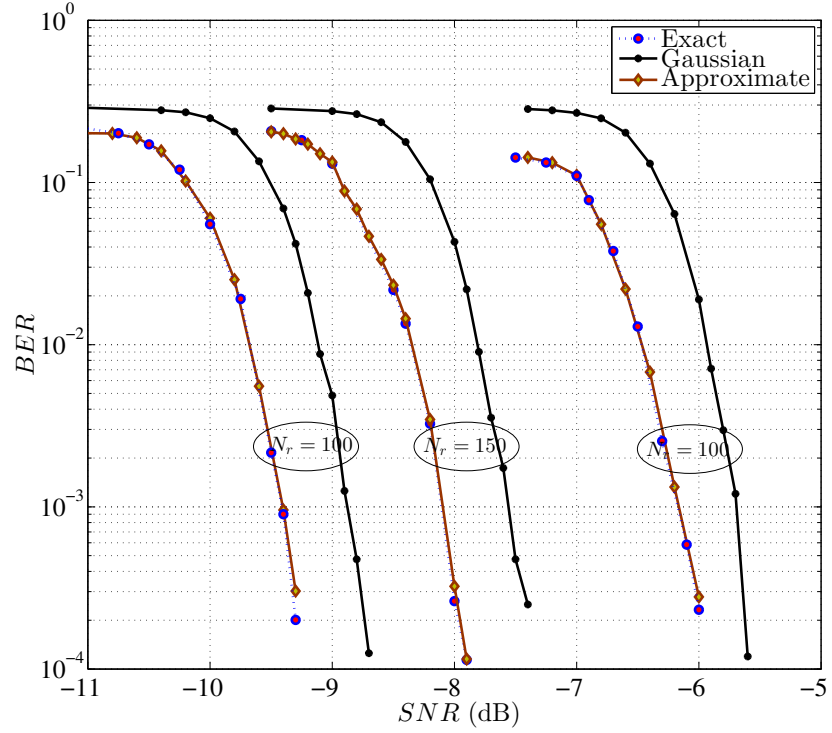
the LLRs for the 16-QAM scheme required 5-th and 6-th order polynomials to match the performance as shown in Figs. 3.9a) and 3.9b), respectively.

In addition, Fig. 3.11 demonstrates the reduction in the number of required receive antennas when using the exact LLRs compared to LLRs derived based on the Gaussian assumption as a function of the SNR. Closer inspection of the figure shows that to obtain a BER performance of 10^{-5} at SNR = -16.3 dB, the required number of receive antennas was $N_r = 500$ for the exact LLR computations, while the Gaussian based LLRs require $N_r = 575$ antennas to achieve the same performance at $N_t = 10$ transmit antennas and 4-QAM scheme. Thus, using error correction with exact LLR computations, a reduction of 75 antenna elements and their corresponding RF chains can be achieved. Furthermore, increasing the number of transmit antennas from 5 to 10 to 20 results in a reduction of 2.4 and 3.5 dB for the exact PDF approach respectively. In contrast, for the Gaussian based PDF, the degradation was in both cases 3 dB.

In Fig. 3.12a), the performance of the turbo coded massive MIMO-OFDM system at $N_t = 10, N_r = 100$ is obtained for different OFDM block length to address their effect on the BER performance of the coded systems. It is observed that at $N_{fft} \geqslant 512$, the coded system exhibit similar performance, while at $N_{fft} = 256$ the performance has reduced by 0.5 dB compared to the original performance. Further reduction in the OFDM block length to 128 has reduced the BER performance by more than 2 dB. In Fig. 3.12b), the performance of the turbo coded massive MIMO-OFDM system at $N_t = 10, N_r = 100$ is obtained for different interleaver block length to examine their effect on the BER performance of the coded system. It is observed that when the interleaver length N_π has dropped from 4096 to 512 it results in a reduction of 0.6 dB to the BER performance, while the complexity and the run time is highly increased. In Fig. 3.13, the performance of the coded and uncoded massive MIMO-OFDM system at $N_t = 10, N_r = 100$ is examined for different CP lengths to discuss their effect on the BER performance. It is observed from Fig. 3.13a) that, as the CP length decreased from 128 to 32, the performance has degraded by almost 8 dB at BER = 10^{-5}. However, reducing the CP length for the coded system of Fig. 3.13b) has a small effect on the performance that is less than 0.5 dB.
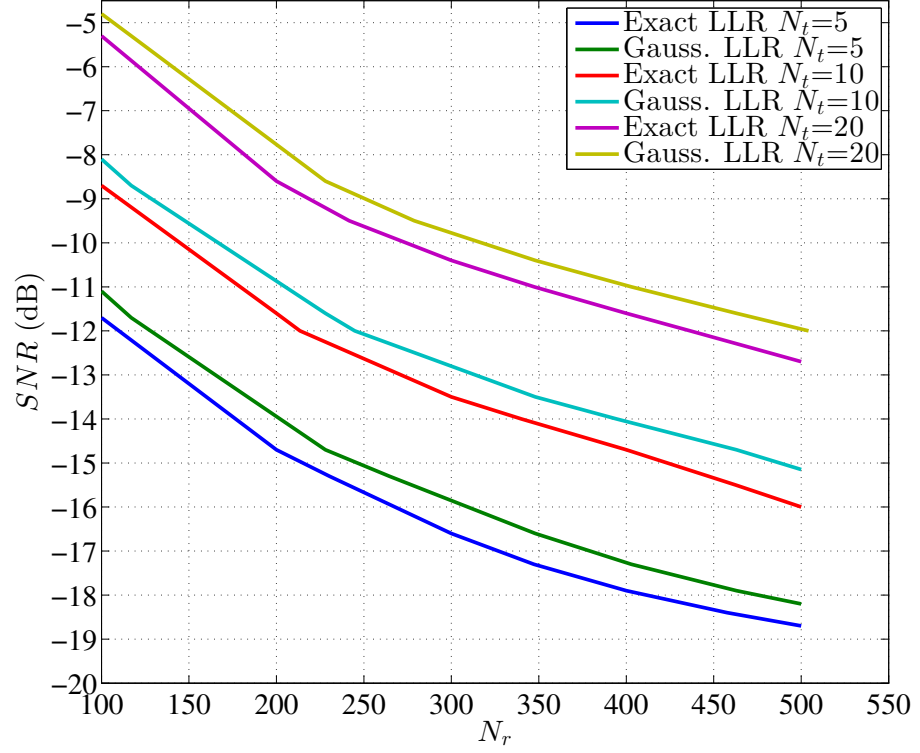
(a) Turbo coded system.
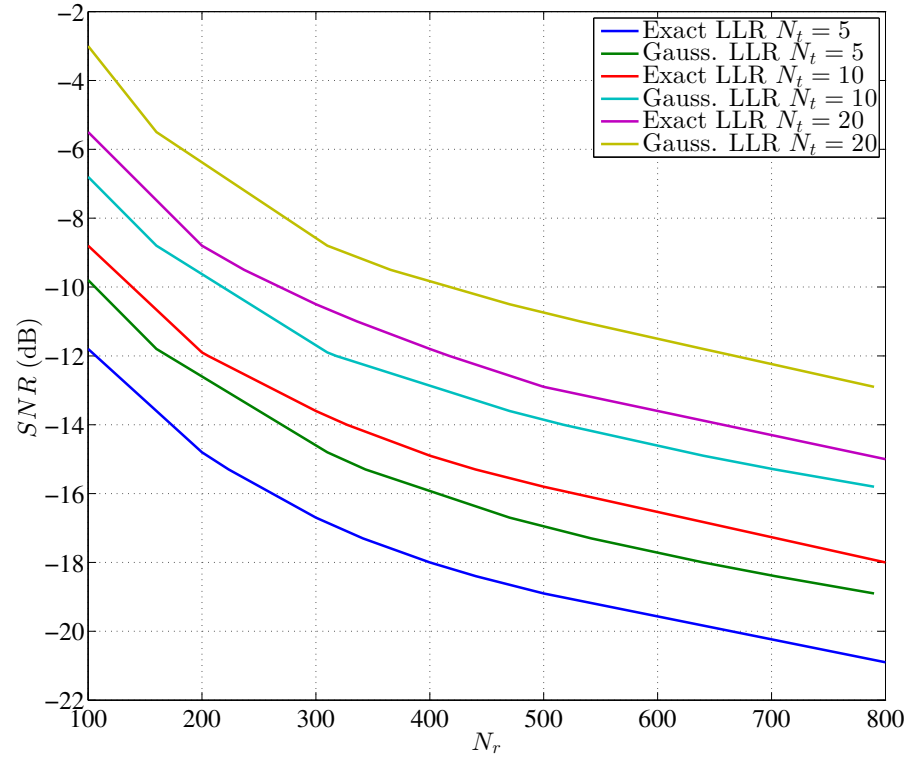
(b) LDPC coded system.

Figure 3.11: Comparing the number of required receive antennas in Gaussian PDF based LLR and the exact LLR at different transmit and receive antennas for, (a) Turbo coded system. (b) LDPC coded system.
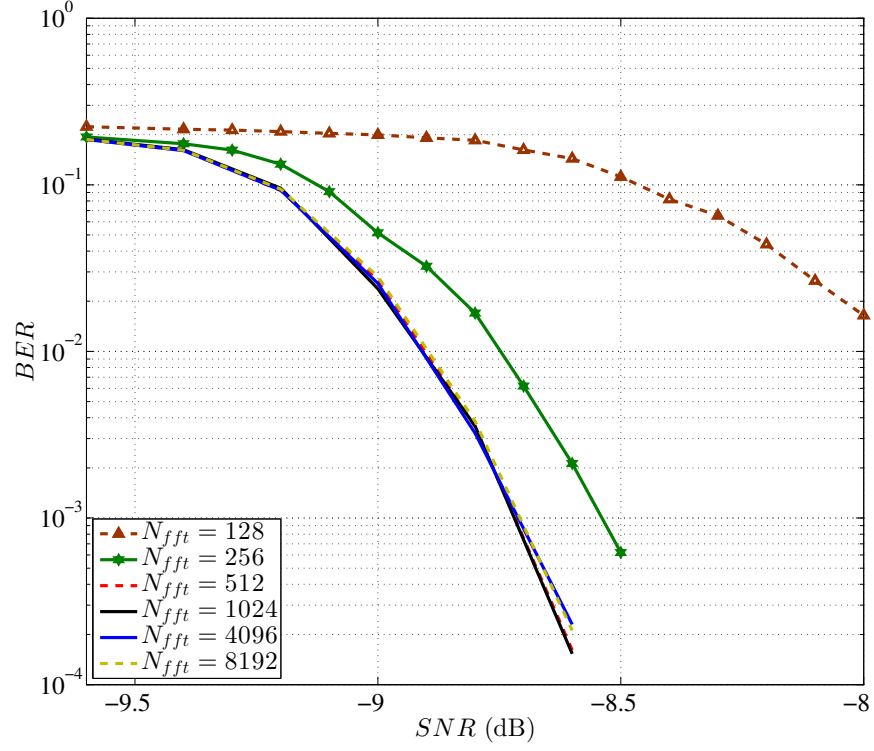
(a) Turbo coded system with different OFDM block lengths.
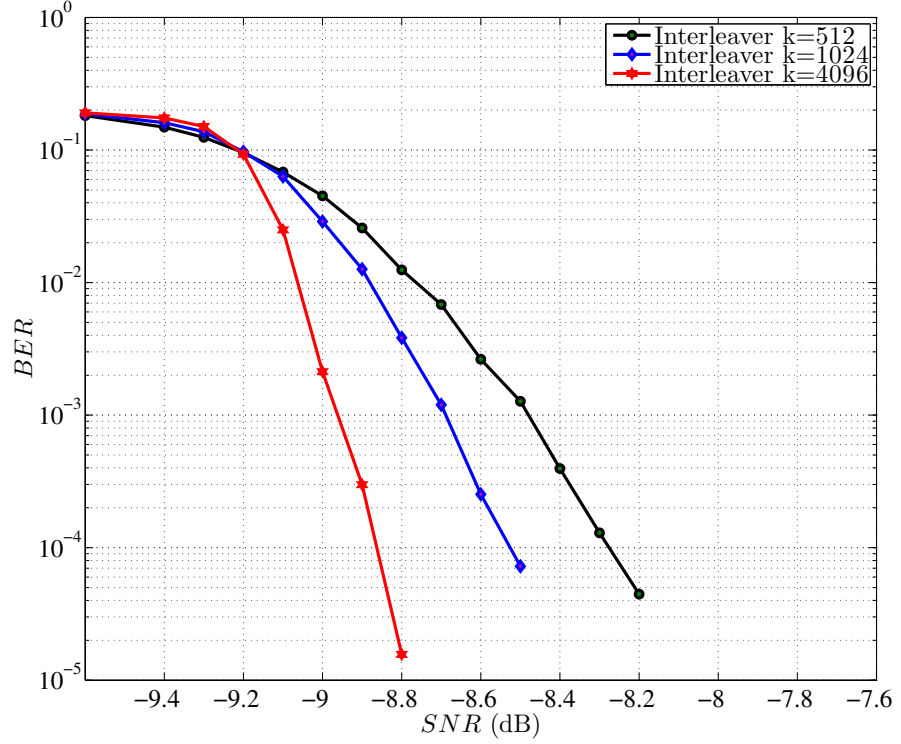
(b) Turbo coded system with different interleaver block lengths.

Figure 3.12: Comparing the effect of different OFDM and interleaver block lengths on the performance of the turbo coded massive MIMO-OFDM systems with $N_t = 10, N_r = 100$. (a) Turbo coded system with different OFDM block lengths. (b) Turbo coded system with different interleaver block lengths.
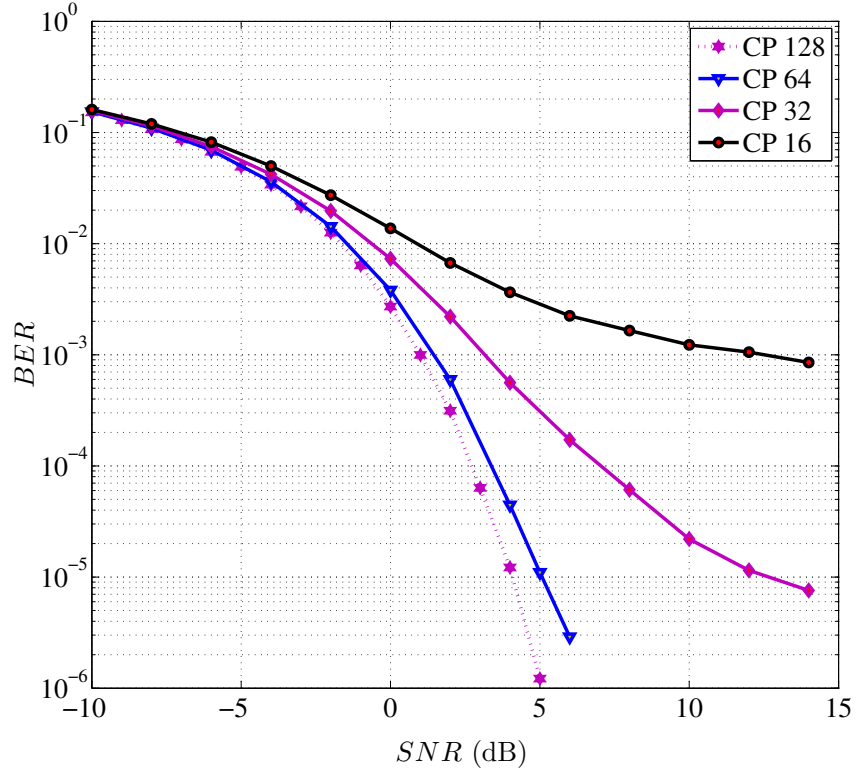
(a) Uncoded system.
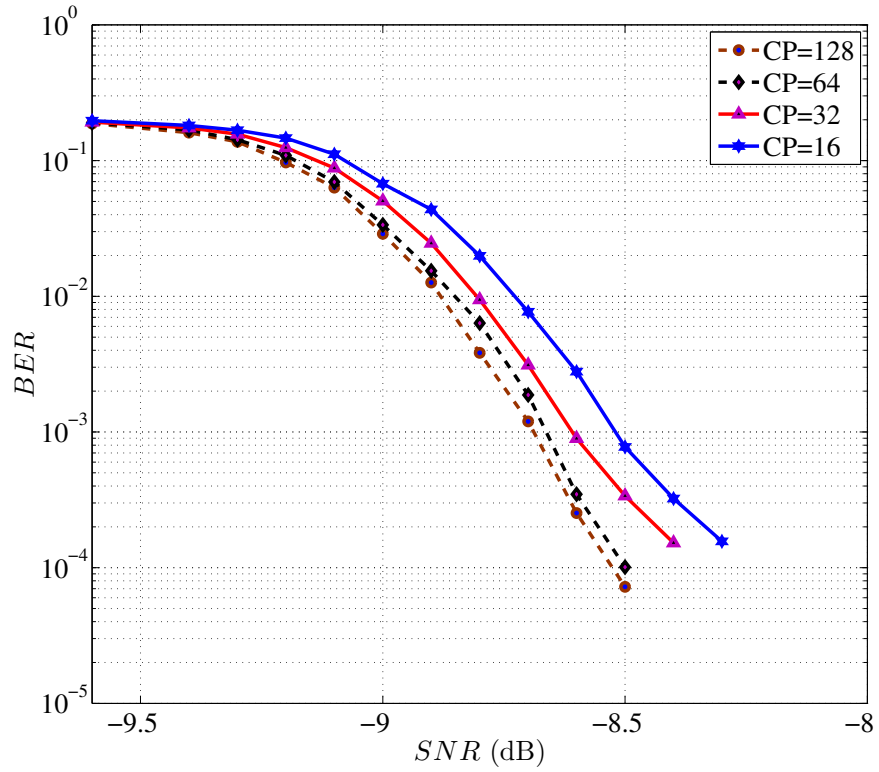
(b) Turbo coded system.

Figure 3.13: Comparing the effect of CP on the performance of the coded/uncoded massive MIMO-OFDM systems with $N_t = 10, N_r = 100$. (a) Uncoded massive MIMO-OFDM system. (b) Turbo coded massive MIMO-OFDM system.

3.8 Chapter Summary

In this chapter, the LLRs for the coded massive MIMO-OFDM systems has been derived based on the complex ratio distribution for the ZFE by means of Neumann approximation. The experimentally obtained histogram plots from Monte-Carlo simulations were shown to be optimally modelled by the theoretically derived PDF which was subsequently used to calculate the LLRs for the LDPC and turbo decoders. This has improved the BER performance of the simulation by 2 dB at 10^{-4} for the LDPC coded system, and 1 dB for the turbo coded system, compared to Gaussian distribution using the ZFE and with the 4-QAM scheme. However, the improvement in the BER performance for the 16-QAM modulated systems was 1 dB for the LDPC coded systems and 0.6 dB for the turbo coded systems, respectively.

Furthermore, calculating the LLRs using the PDF of (3.37) have improved the performance compared to the Gaussian assumption resulting in a reduction in the required number of receive antennas by 75 at an SNR of -16.3 dB. However, this new PDF increased the computational complexity of LLR calculations, thus, increasing the overall receiver complexity. To reduce this complexity and to maintain good performance, an equivalent LLR equation has been suggested with a low complexity design using Newton polynomial interpolation. The performance of this approximated LLR equation showed a close match to the exact LLR with negligible complexity.

The effect of changing the OFDM block length, the interleaver length and the CP length on the performance of the coded massive MIMO-OFDM systems have been addressed in this chapter as part of selecting the most convenient test bed. It is observed that reducing the block length of the OFDM, the interleaver or the CP will result in a degradation to the BER performance of the coded system, however, increasing the interleaver length can increase the complexity and improve the performance.

Chapter 4

Performance Evaluation for the Massive MIMO-OFDM systems

4.1 Introduction

Massive MIMO systems have recently attracted immense interest in the field of wireless communications due to their ability to increase data throughput and improve link quality [78, 67, 79, 80]. Meanwhile, OFDM is a multi-carrier technique with immunity to the channel's frequency selectivity, which can transmit data over large numbers of sub-carriers rather than a single carrier transmission [2, 81]. The combination of these two techniques in the form of a massive MIMO-OFDM system is a key technology for the next generation wireless communication systems due to its improved performance compared to conventional MIMO systems [78, 82].

Calculating the channel capacity and the outage probability for the massive MIMO-OFDM systems are of interest due to their impact on the system design. The channel capacity and the outage probability of the massive MIMO systems have been studied in the literature [83, 84, 85, 86] for the uplink and downlink transmission with different channels. The channel capacity of the massive MIMO systems over Nakagami-m fading channels has been investigated in [83] for two MIMO models with linear detectors. In [84], an upper bound has been derived for the channel capacity of the spatial non-stationary massive MIMO systems in the uplink mode of transmission. In addition, the outage probability has been analyzed in [85] for the multi-user massive MIMO systems with Rayleigh fading channels and an approximate expression is introduced to bound the outage probability. Furthermore, based on the outage probability requirements, a novel approach has been introduced in [86] to minimize the required number of antennas for the massive MIMO systems.

In addition, employing forward error correction (FEC) coding can further improve the performance of massive MIMO-OFDM systems due to the resulting frequency diversity and increased the reliability of the transmitted data signals over K subcarriers and N_t transmitters [87]. Improvement in the BER performance can reduce the number of receiving antennas required to design coded massive MIMO-OFDM systems compared to uncoded systems [88, 89, 90, 91, 92, 93, 94].

To evaluate the performance of coded massive MIMO-OFDM systems time consuming simulations are required. Thus, upper-bounds are of immense interest due to their ability to predict the performance of such a system. In [70, 95, 96, 97, 98], the upper-bounds of convolutional codes have been studied for the AWGN and for fading channels including different approximations. The performance of convolutionally coded MIMO

systems with MMSE detector has been derived in [99] using the moment generating function (MGF). In[100], a tight bound on a bit-interleaved space-time coded modulation (BI-STCM) scheme has been developed for MIMO systems with rate (1/2) convolutional code. Furthermore, link-level capacity (LLC) and a tight bound have been derived in [101] for a MIMO-BICM system with a ZFE and a fast fading channel.

In [102, 103] the upper-bound of parallel concatenated codes assuming a uniform interleaver has been determined for turbo coded systems. The authors derived the upper-bound for both block and convolutional concatenated codes for an AWGN channel. In [104], an average bound has been proposed for the performance of turbo coded systems with correlated and uncorrelated Rayleigh fading channels. In [89, 105], the authors have proposed an upper-bound to the turbo coded MIMO system with correlated and uncorrelated Rayleigh slow fading channels, and the proposed bound approached the simulation results within (0.2-0.5) dB at a BER of 10^{-5}.

However, no significant results have been presented for the upper-bound performance of coded massive MIMO-OFDM systems. The contribution of this chapter can be summarized as follows:

- Deriving the BER for the massive MIMO-OFDM system with frequency selective Rayleigh fading channels and ZFE for different M-ary modulations.

- Obtaining the PDF of the SNR after the ZFE to be used in deriving the outage probability, the average capacity, and three bounds to the capacity at low and high SNR, respectively.

- Deriving the PEP for the massive MIMO-OFDM system to be used in the performance evaluation of the coded system.

- This PEP is subsequently used to evaluate the upper-bounds of the convolutionally coded and turbo coded systems.

This analysis are based on using the Neumann matrix approximation to simplify the matrix inversion of the ZFE when deriving the noise PDF.

4.2   Uncoded Massive MIMO-OFDM Systems

4.2.1   Bit Error Rate (BER)

This section starts by deriving the BER for the binary phase shift-keying (BPSK) and 4-QAM modulations and then extend the derivations to include higher QAM constellations.

4.2.1.1   BPSK and 4-QAM

Deriving the BER for the BPSK modulation requires computing the following integration [31]

$$P_e^{BPSK} = \int_0^\infty p(\alpha_{l,k}^\nu + 1) \, d\alpha_{l,k}^\nu. \tag{4.1}$$

The BER is obtained by substituting (3.35) and (3.36) in (4.1) and integrating (4.2) in two steps with respect to $\alpha_{l,k}^\nu$ and $\zeta_{l,k}$ following the procedure presented in [106]

$$P_e^{BPSK} \approx \int_0^\infty \int_0^\infty \sum_{n=1}^{N_r} \frac{(N_r + n - 2)! \, |\zeta_{l,k}|^{2N_r-n} \exp\left(-\frac{|\zeta_{l,k}|}{2\sigma_H^2}\right)}{(2\sigma_H^2)^{N_r} (\sigma_H\sigma_w)^{N_r-n+1} (N_r - n)! \, 2^{N_r+n-1} \, \Gamma(n)\Gamma^2(N_r)} \times$$
$$\exp\left(\frac{-\left|(\alpha_{l,k}^\nu + 1)\zeta_{l,k}\right|}{\sigma_H\sigma_w}\right)(\left|\alpha_{l,k}^\nu + 1\right|)^{N_r-n} d\alpha_{l,k}^\nu d\zeta_{l,k}. \tag{4.2}$$

First, integrating with respect to $\alpha_{l,k}^\nu$ to obtain I_1, i.e.

$$I_1 = \int_0^\infty (\left|\alpha_{l,k}^\nu + 1\right|)^{N_r-n} \exp\left(\frac{-\left|(\alpha_{l,k}^\nu + 1)\zeta_{l,k}\right|}{\sigma_w \, \sigma_H}\right) d\alpha_{l,k}^\nu. \tag{4.3}$$

The solution for (4.3) is obtained using [107, Eq. (3.351.2)],

$$I_1 = \frac{(N_r - n)! \exp(-\frac{|\zeta_{l,k}|}{\sigma_w\sigma_H})}{(\frac{|\zeta_{l,k}|}{\sigma_w\sigma_H})^{N_r-n+1}} \sum_{m=0}^{N_r-n} \frac{(\frac{|\zeta_{l,k}|}{\sigma_w\sigma_H})^m}{m!}. \tag{4.4}$$

Similarly, integrating with respect to $\zeta_{l,k}$ results in

$$I_2 = \int_0^\infty |\zeta_{l,k}|^{N_r+m-1} \exp\left(-|\zeta_{l,k}|\,\eta\right) d\zeta_{l,k}, \tag{4.5}$$

where $\eta = \left(\frac{\sigma_w + 2\sigma_H}{2\sigma_H^2\sigma_w}\right)$. Solving (4.5) using [107, Eq. (3.351.3)], will obtain I_2 as

$$I_2 = \frac{\Gamma(N_r + m)}{\eta^{N_r+m}}. \tag{4.6}$$
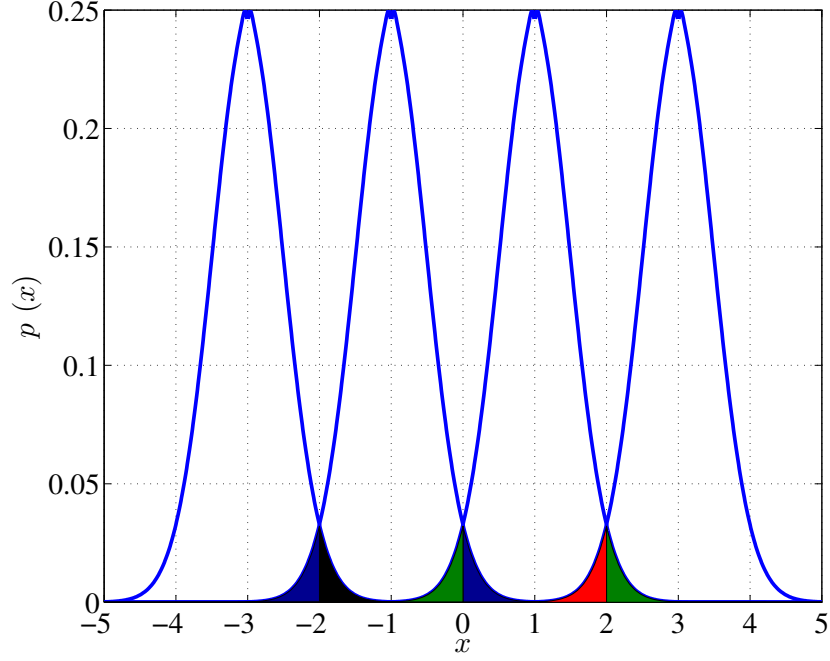
Figure 4.1: Noise distribution in 4-PAM modulated massive MIMO-OFDM with $N_t = 10$ and $N_r = 100$.

Substituting I_1 and I_2 in (4.2), results in

$$P_e^{BPSK} = \frac{1}{(2\sigma_H^2)^{N_r}\Gamma^2(N_r)} \sum_{n=1}^{N_r} \frac{(N_r + n - 2)!I_1 I_2}{(\sigma_H \sigma_w)^{N_r-n+1}(N_r - n)!\, 2^{N_r+n-1}\,\Gamma(n)} \,. \tag{4.7}$$

After straightforward mathematical manipulations, the BER for massive MIMO-OFDM systems with BPSK and 4-QAM modulation can be written as

$$P_e^{BPSK} = \frac{\left(\frac{\sigma_w}{2\sigma_H}\right)^{N_r}}{2^{N_r-1}\Gamma^2(N_r)} \sum_{n=1}^{N_r} \sum_{m=0}^{N_r-n} \frac{2^{-n}(N_r + n - 2)!\Gamma(N_r + m)}{m!\,\Gamma(n)(1 + \frac{\sigma_w}{2\sigma_H})^{N_r+m}}. \tag{4.8}$$

4.2.1.2 4-Pulse Amplitude Modulation (4-PAM) and 16-QAM Modulation

The BER for higher QAM constellations can be determined using the relationship between the PAM and QAM schemes [31]

$$P_s^{M-QAM} = 1 - (1 - P_s^{\sqrt{M}-PAM})^2, \tag{4.9}$$

$$P_e^{M-QAM} = \frac{P_s^{M-QAM}}{\log_2 M}, \tag{4.10}$$

70

where P_s^{M-QAM} and $P_s^{\sqrt{M}-PAM}$ denote the symbol error rate (SER) for the QAM, PAM modulations, respectively, and P_e^{M-QAM} is the BER for M-QAM. The SER for the 4-PAM can be derived by exploiting the noise distribution in Fig. 4.1. For practical SNR ranges, only 6 error events need to be considered that are distributed within 4 equiprobable noise PDFs. Due to symmetry, the SER can be obtained by considering only one event. The error probability generated by the noise PDF $p(|\alpha_{l,k}^\nu + 3|)$ can be calculated as

$$P_{s_1} = \int_{-2}^{\infty} p(|\alpha_{l,k}^\nu + 3|)d\alpha_{l,k}. \tag{4.11}$$

The result of this integration is similar to (4.1), hence, the SER for the 4-PAM modulation can be written as

$$P_s^{4-PAM} = \frac{6}{4}P_{s_1} = \frac{3(\frac{\sigma_w}{2\sigma_H})^{N_r}}{2^{N_r}\Gamma^2(N_r)} \sum_{n=1}^{N_r} \sum_{m=0}^{N_r-n} \frac{2^{-n}(N_r+n-2)!\,\Gamma(N_r+m)}{m!\,\Gamma(n)\,(1+\frac{\sigma_w}{2\sigma_H})^{N_r+m}}. \tag{4.12}$$

Subsequently, the SER and the BER for 16-QAM can be determined by substituting (4.12) into (4.9) and the outcome in (4.10). In general, the SER for the $\sqrt{M}$-PAM for $\sqrt{M} \geq 4$ can be written as

$$P_s^{\sqrt{M}-PAM} = \frac{2(\sqrt{M}-1)}{\sqrt{M}}P_{s1}. \tag{4.13}$$

The BER performance of the massive MIMO-OFDM systems are demonstrated in Fig 4.3 for a different number of receive and transmitted antennas at BPSK and 16-QAM schemes.

4.2.2 Signal to Noise Ratio (SNR)

Different approaches have been used to calculate the PDF of the SNR at the receiver. In this section, the PDF of the SNR can be written based on the more accurate noise PDF derived (3.37) [68]. The instantaneous SNR at the output of the ZFE can be written as,

$$\gamma_{l,k} = \frac{E_b}{2\,(\alpha_{l,k}^\nu)^2}. \tag{4.14}$$

where, E_b is the bit energy. To derive the PDF for the SNR utilizing the noise PDF in (3.37), the following expressions are used [74],

- for $y = ax^2$

$$p_y(y) = \frac{1}{2a\sqrt{y/a}} \left[p_x \left(\sqrt{\frac{y}{a}} \right) + p_x \left(-\sqrt{\frac{y}{a}} \right) \right] \quad y > 0, \qquad (4.15)$$

- for $y = \frac{1}{x}$

$$p_y(y) = \frac{1}{y^2} p_x \left(\frac{1}{y} \right). \qquad (4.16)$$

According to that, and by substituting (4.15) and (4.16) based on (4.14), the PDF of the SNR can be written as

$$
\begin{aligned}
p(\gamma_{l,k}) &= \frac{\sqrt{E_b}}{(2\,\gamma_{l,k})^{3/2}} p\left(\alpha_{l,k}^\nu = \sqrt{\frac{E_b}{2\,\gamma_{l,k}}} \right), \\
&= \sum_{n=1}^{N_r} \frac{(N_r + n - 2)!(2N_r - n)!(\frac{\sigma_w}{2\sigma_H})^{N_r}}{2^{N_r+n-1}\Gamma^2(N_r)(N_r - n)!\Gamma(n)} \frac{(\sqrt{E_b})^{N_r-n+1}(\sqrt{2\,|\gamma_{l,k}|})^{n-3-N_r}}{\left(\sqrt{\frac{E_b}{2\,|\gamma_{l,k}|}} + \frac{\sigma_w}{2\sigma_H} \right)^{2N_r-n+1}}.
\end{aligned}
$$

$$(4.17)$$

Fig. 4.2 shows the PDF of the SNR at $N_t = 10$ transmit antennas and $N_r = 160, 180, 200$ receive antennas.

4.2.3 Outage Probability

In communication systems, the probability of not satisfying the required BER at a specific SNR value (γ_{th}), is known as the outage probability [108].

In this section, the outage probability for the massive MIMO-OFDM systems after the ZFE is derived using, $P_{out} = \int_0^{\gamma_{th}} p(\gamma_{l,k}) d\gamma_{l,k}$. However, the direct substitution of (4.17) into this integral results in a very complicated integration that can not be solved. Therefore, the equations (3.35) and (3.36) are substituted into (4.14) to perform the integration of the outage probability as

$$
\begin{aligned}
P_{out} = \int_0^\infty \int_0^{\gamma_{th}} \sum_{n=1}^{N_r} & \frac{\sqrt{E_b}(N_r + n - 2)! \left(\sqrt{\frac{E_b}{2\gamma_{l,k}}} \zeta_{l,k} \right)^{N_r-n}}{\Gamma^2(N_r)(\sqrt{2\gamma_{l,k}})^3 (2\sigma_H^2)^{N_r}} \times \\
& \frac{\zeta_{l,k}^{N_r} \exp\left(-\frac{\zeta_{l,k}}{2\sigma_H^2} \right) \exp\left(-\sqrt{\frac{E_b}{2\gamma_{l,k}}} \frac{\zeta_{l,k}}{\sigma_H \sigma_w} \right)}{(N_r - n)!\, 2^{N_r+n-1}\Gamma(n)(\sigma_w \sigma_H)^{N_r-n-1}} d\gamma_{l,k} d\zeta_{l,k}.
\end{aligned}
$$

$$(4.18)$$
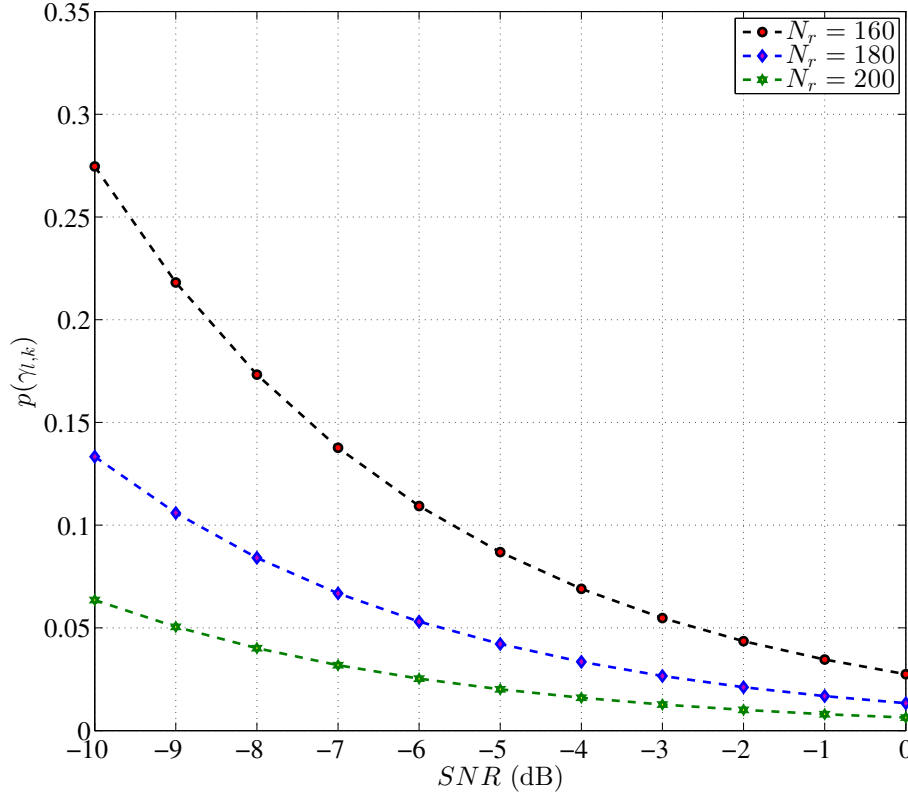
Figure 4.2: PDF of the SNR at the output of the ZFE with $N_t = 10$.

The first part of this integration has the form [107, Eq. (3.351.3)]

$$
\begin{aligned}
I_1 &= \int_0^{\gamma_{th}} \frac{\exp\left(-\frac{\zeta_{l,k}\sqrt{E_b}}{\sigma_H \sigma_w \sqrt{2\gamma_{l,k}}}\right)}{(\sqrt{2\gamma_{l,k}})^{N_r-n+3}} \, d\gamma_{l,k} \\
&= \exp\left(\frac{-\zeta_{l,k}\sqrt{E_b}}{\sigma_w \sigma_H \sqrt{2\gamma_{th}}}\right) \sum_{m=0}^{N_r-n} \frac{(N_r-n)!(\sigma_w \sigma_H)^{N_r-n-m+1}}{m!(\sqrt{2\gamma_{th}})^m(\sqrt{E_b}\zeta_{l,k})^{Nr-n-m+1}} \, .
\end{aligned} \tag{4.19}
$$

Similarly, the second part of (4.18) can be solve as

$$
\begin{aligned}
I_2 &= \int_0^\infty \zeta_{l,k}^{N_r+m-1} \exp\left(-\frac{\sigma_w\sqrt{2\gamma_{th}} + 2\sigma_H\sqrt{E_b}}{2\sigma_H^2 \sigma_w \sqrt{2\gamma_{th}}}\zeta_{l,k}\right) d\zeta_{l,k} \\
&= \frac{(N_r+m-1)!(\sigma_H \sigma_w \sqrt{2\gamma_{th}})^{N_r+m}}{\left(\frac{\sigma_w}{2\sigma_H}\sqrt{2\gamma_{th}} + \sqrt{E_b}\right)^{N_r+m}} \, .
\end{aligned} \tag{4.20}
$$

Hence, the outage probability can be written as

$$
P_{out} = \sum_{n=0}^{N_r} \sum_{m=0}^{N_r-n} \frac{(N_r+n-2)!(N_r+m-1)!(\frac{\sigma_w}{2\sigma_H})^{N_r}(\sqrt{2\gamma_{th}})^{N_r}(\sqrt{E_b})^m}{\Gamma^2(N_r)\Gamma(n)m!2^{N_r+n-2}(\sqrt{E_b} + \sqrt{2\gamma_{th}}\frac{\sigma_w}{2\sigma_H})^{N_r+m}} \, . \tag{4.21}
$$

The outage probability of massive MIMO-OFDM systems is demonstrated in Figs. 4.4 and 4.5 at $N_t = 4, 10$ and $N_r = 100, 200$ for BPSK and 16-QAM schemes, respectively.

4.2.4   Channel Capacity

The channel capacity using ZFE and the effective noise PDF for the investigated massive MIMO-OFDM system can be derived using [109]

$$C = \int_0^\infty \log_2(1 + \gamma_{l,k}) p(\gamma_{l,k}) d\gamma_{l,k}. \tag{4.22}$$

An explicit solution to this integration using the available integration methods is not feasible. Alternatively, an exact solution that is numerically evaluated based on the trapezoidal numerical integration method is applied to determine the solution of this integral. To obtain a closed-form solution, three approximations are introduced to bound the exact capacity at low and at high SNR, respectively.

4.2.4.1   At Low SNR (LB1)

At low SNR, the term $\log_2(1 + \gamma_{l,k})$ can be approximated to $(\sqrt{\gamma_{l,k}})$, and the capacity is calculated using

$$C = \int_0^\infty \sqrt{\gamma_{l,k}} \, p(\gamma_{l,k}) d\gamma_{l,k} . \tag{4.23}$$

The solution for this integration involves the following step [107, Eq. (3.351.3)]

$$I_3 = \int_0^\infty x^N \exp(-\eta x) dx = \frac{N!}{\eta^{N+1}} . \tag{4.24}$$

Thus, the lower bound on the capacity can be written as

$$C = \sum_{n=1}^{N_r - 1} \frac{\sqrt{E_b}(N_r + n - 2)!(N_r - n - 1)!(N_r)!}{\Gamma(N_r)\Gamma(n)(N_r - n)!2^{N_r + n - 0.5}(\sigma_H \sigma_w)} . \tag{4.25}$$

4.2.4.2   At Low SNR (LB2)

Another approximation at low SNR can be made when the term $\log_2(1 + \gamma_{l,k})$ is approximated to $\frac{1}{\log_e(2)}(\gamma_{l,k} - \frac{(\gamma_{l,k})^2}{2})$, and the capacity can be calculated as

$$C = \frac{1}{\log_e(2)} \int_0^\infty (\gamma_{l,k} \, p(\gamma_{l,k}) - \frac{(\gamma_{l,k})^2}{2} \, p(\gamma_{l,k})) d\gamma_{l,k} . \tag{4.26}$$

For simplicity, I_4 and I_5 are defined as

$$I_4 = \frac{1}{\log_e(2)} \int_0^\infty \gamma_{l,k}\, p(\gamma_{l,k})d\gamma_{l,k}\ ,$$

$$I_5 = \frac{1}{\log_e(2)} \int_0^\infty \frac{(\gamma_{l,k})^2}{2}\, p(\gamma_{l,k})d\gamma_{l,k}\ , \tag{4.27}$$

which represent the decomposition of (4.26). This integration can be solved using (4.24) and the result has the form

$$I_4 = \sum_{n=1}^{N_r-2} \frac{\sqrt{E_b}(N_r+n-2)!(N_r-n-2)!(N_r+1)!(\frac{2\sigma_H}{\sigma_w})^2}{\Gamma^2(N_r)\Gamma(n)(N_r-n)!2^{N_r+n}\log_e(2)}\ , \tag{4.28}$$

and

$$I_5 = \sum_{n=1}^{N_r-4} \frac{\sqrt{E_b}(N_r+n-2)!(N_r-n-4)!(N_r+3)!(\frac{2\sigma_H}{\sigma_w})^4}{\Gamma^2(N_r)\Gamma(n)(N_r-n)!2^{N_r+n+2}\log_e(2)}\ . \tag{4.29}$$

Thus, the capacity bound at low SNR can be calculated using $C = I_4 - I_5$.

4.2.4.3 At High SNR (UB)

At high SNR, the term $\log_2(1 + \gamma_{l,k})$ can be approximated to $\log_2(\gamma_{l,k})$. Thus, the integration in (4.22) can be written as

$$C \approx \int_0^\infty \log_2(\gamma_{l,k})p(\gamma_{l,k})d\gamma_{l,k}\ . \tag{4.30}$$

This integration can be solved in two steps, each of which requires the following integration [107, Eq. (4.352.1)]

$$I_6 = \int_0^\infty \log_e(x)x^{N-1}\exp(-\eta x)dx\ ,$$

$$= \frac{\Gamma(N)}{\eta^N}[\psi(N) - \log_e(\eta)]\ , \tag{4.31}$$

where $\psi(N) = \frac{d}{dN}\log_e(\Gamma(N))$ [107, Eq. (8.360)]. Hence, the upper bound of the channel capacity (4.30) can be written as

$$C = \sum_{n=1}^{N_r} \frac{(N_r + n - 2)!}{\log_e(2)\Gamma(N_r)\Gamma(n)2^{N_r+n-1}}(2\psi(N_r) - 2\psi(N_r - n + 1)+$$

$$2\log_e(\frac{\sigma_H}{\sigma_w}) + \log_e(E_b)) \ . \tag{4.32}$$

In the next section, the PEP and the upper bound for the convolutionally coded and turbo coded massive MIMO-OFDM systems will be calculated.

4.3 Bounds for Coded Massive MIMO-OFDM Systems

In this section, the PEP between any two different code words will be derived based on the noise distribution after the ZFE shown in (3.37). Then, an upper-bound for the convolutionally coded massive MIMO-OFDM systems is obtained by combining this PEP with the error weights listed in [96, 97]. In addition, an average-bound for turbo coded massive MIMO-OFDM systems is derived using the method introduced in [102].

4.3.1 Pairwise Error Probability

The probability of incorrectly decoding the code word $\mathbf{s}_2$ instead of the code word $\mathbf{s}_1$ is known as the PEP. Based on (3.3) and the noise distribution of (3.37), the PEP can be written as

$$P_{\mathbf{s}_1 \to \mathbf{s}_2} = p(||\hat{\mathbf{s}} - \mathbf{s}_2||^2 \leq ||\hat{\mathbf{s}} - \mathbf{s}_1||^2) \ ,$$
$$= p(||\mathbf{s}_1 + \hat{\mathbf{n}} - \mathbf{s}_2||^2 \leq ||\mathbf{s}_1 + \hat{\mathbf{n}} - \mathbf{s}_1||^2) \ ,$$
$$= p(\hat{\mathbf{n}} \leq \frac{||\mathbf{s}_2 - \mathbf{s}_1||}{2}) \ , \tag{4.33}$$

where $P_{\mathbf{s}_1 \to \mathbf{s}_2}$ is the PEP. Next, by substituting $||\mathbf{s}_2 - \mathbf{s}_1|| = 2\sqrt{E_c d}$, where, d is the hamming distance for the code words, and E_c is the coded bit energy. Thus, the PEP can be written as

$$P_{\mathbf{s}_1 \to \mathbf{s}_2} = \int_{\sqrt{E_c d}}^{\infty} p(\alpha_{l,k}^{\nu})d\alpha_{l,k}^{\nu} \ . \tag{4.34}$$

The result of this integration can be written in the form

$$P_{\mathbf{s}_1 \to \mathbf{s}_2} = \frac{\left(\frac{\sigma_w}{2\sigma_H}\right)^{N_r}}{2^{N_r-1}\Gamma^2(N_r)} \sum_{n=1}^{N_r} \sum_{m=0}^{N_r-n} \frac{2^{-n}(N_r+n-2)!\Gamma(N_r+m)}{m!\,\Gamma(n)(1+\frac{\sigma_w}{2\sigma_H\sqrt{E_c d}})^{N_r+m}(E_c d)^{\frac{N_r}{2}}}. \tag{4.35}$$

4.3.2 Upper-Bounds for Convolutionally Coded Massive MIMO-OFDM Systems

According to [96, 97], the upper- bound for the convolutionally coded systems has been shown to have the form

$$P_b < \sum_{d=d_{free}}^{\infty} c_d P_{\mathbf{s}_1 \to \mathbf{s}_2}(d), \tag{4.36}$$

where c_d is the sum of error events for each d. In this work, the PEP for the massive MIMO-OFDM systems can be described using (4.35). Thus, the upper-bound equation for the coded massive MIMO-OFDM systems can be written as

$$P_b < \sum_{d=d_{free}}^{\infty} \frac{c_d\left(\frac{\sigma_w}{2\sigma_H}\right)^{N_r}}{2^{N_r-1}\Gamma^2(N_r)} \sum_{n=1}^{N_r} \sum_{m=0}^{N_r-n} \frac{2^{-n}(N_r+n-2)!\Gamma(N_r+m)}{m!\,\Gamma(n)(1+\frac{\sigma_w}{2\sigma_H\sqrt{d}})^{N_r+m}d^{\frac{N_r}{2}}}. \tag{4.37}$$

In Appendix A, the number of error events c_d are listed in a tables for different code generators and for code rates $1/2, 1/3$ and $1/4$, respectively [96, 97].

4.3.3 Asymptotic Upper-Bounds for the Turbo Coded Massive MIMO-OFDM Systems

The excellent performance of turbo codes in wireless communication systems has attracted much attention. However, deriving the bounds for these codes is more complicated than for convolutional codes as they consist typically of two PCCCs separated by an interleaver. Serial concatenation is common too. An average-bound has been derived in [102] using the input-redundancy weight enumerating function (IRWEF) for the combination of two convolutional codes involved in the construction of the turbo code. First, the conditional weight enumerating function (CWEF) is derived from the transfer function of each code, then an average CWEF ($A_{\iota j,\delta\varrho}^{C_p}(\omega, Z)$) is calculated using

$$A_{\iota j,\delta\varrho}^{C_p}(\omega, Z) = \frac{A_{\iota\delta}^{C_1}(\omega, Z) \cdot A_{j\varrho}^{C_2}(\omega, Z)}{\binom{N_\iota}{\omega}}, \tag{4.38}$$

where $A_{\iota\delta}^{C_1}(\omega, Z)$ and $A_{j\varrho}^{C_2}(\omega, Z)$ are the CWEFs of the first and the second convolutional codes, denoted C_1 and C_2, respectively; ω is the Hamming weight of the input information, N_ι is the interleaver length, and finally, $\binom{N_\iota}{\omega}$ is the binomial distribution of the parameters N_ι and ω. Hence, the IRWEF can be obtained using the average CWEF as follows,

$$A^C(W, Z) = \sum_{\iota j, \delta\varrho} W^{\iota j, \delta\varrho} \, A_{\iota j, \delta\varrho}^{Cp}(\omega, Z). \tag{4.39}$$

The average bound of the turbo coded system has the form

$$P_b \approx \sum_d D_d P_{\mathbf{s}_1 \to \mathbf{s}_2}(d), \tag{4.40}$$

where D_d factors are listed in Table 4.3 for different interleaver lengths [102] and can be calculated using

$$D_d = \sum_{f+\omega=d} \frac{\omega}{d} A_{\omega,f}, \tag{4.41}$$

where f is the Hamming weight of the parity bits.

4.4 Simulation and Results

The simulations obtained in this section are discussed here to verify the accuracy of the derived equations. The system under consideration is massive MIMO-OFDM systems with $N_r >> N_t$, and uncorrelated frequency-selective Rayleigh fading channels. For the simulation purposes, the number of receive antennas were selected as $N_r = 100, 200, 500$ and the transmit antennas were $N_t = 4, 10$. In Section 4.2.1, the PDF of the effective noise that is presented in (3.37) is used to derive the BER equation for the uncoded massive MIMO-OFDM systems with different modulation types. The theoretical BER performance of the BPSK/4-QAM and the 16-QAM schemes are derived in Section 4.2.1 and the results are presented in (4.8), (4.9), (4.10), and (4.12). These BER equations are further compared to the Monte-Carlo simulations with different receive and transmit antennas to verify their accuracy and the results are presented in Figs. 4.3a) and 4.3b). Inspecting these results at $N_t = 4, 10$ and $N_r = 100, 200$ reveal the accuracy of the derived equations compared to the Monte-Carlo simulations, which shows close match between the empirical and the theoretical plots especially at high SNR for the 16-QAM scheme.

In Section 4.2.2, the PDF of the SNR after the MIMO detector at the receiver side is derived based on the effective noise PDF that is derived in the previous chapter. Then
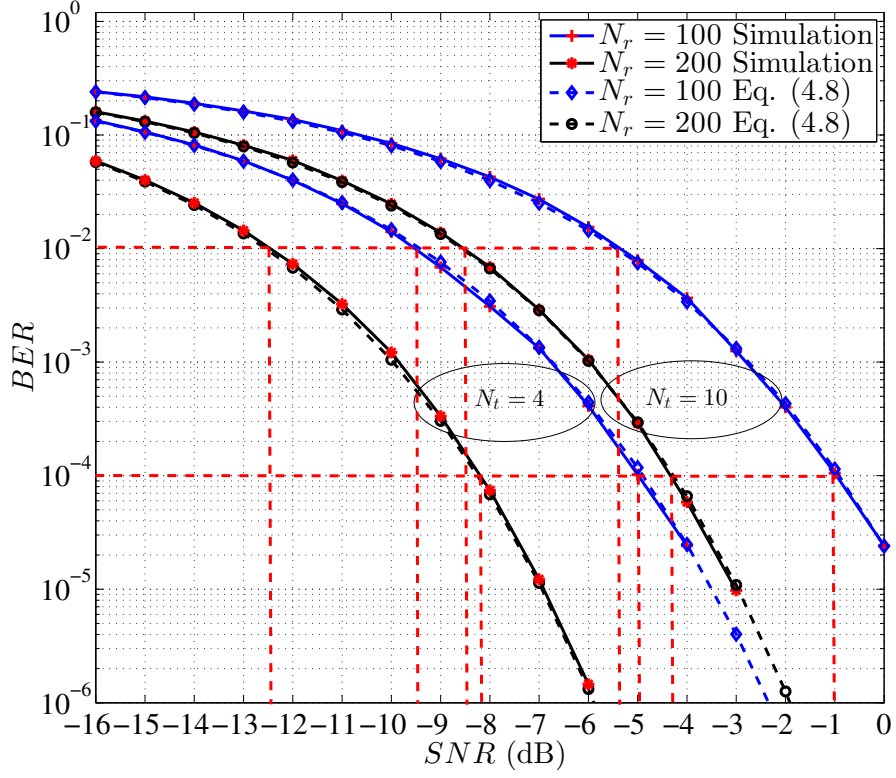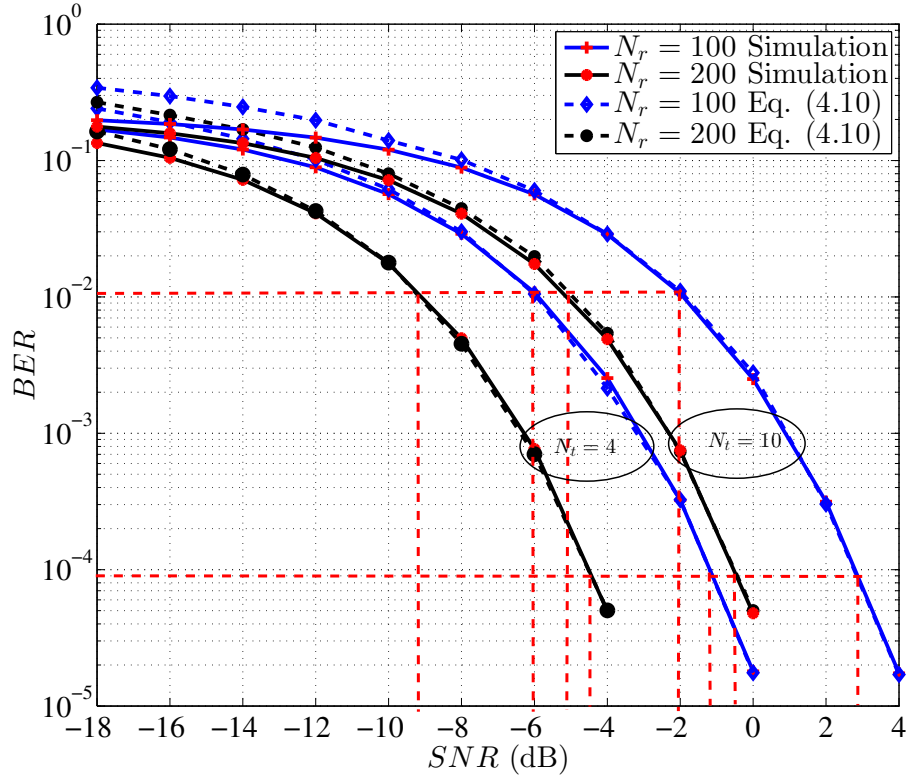
(a) $N_t = 4, 10$ and $N_r = 100, 200$ for BPSK/4-QAM.

(b) $N_t = 4, 10$ and $N_r = 100, 200$ for 16-QAM.

Figure 4.3: BER performance for massive MIMO-OFDM system with $N_t = 4, 10$ and $N_r = 100, 200$, and for (a) BPSK/4-QAM and, (b) 16-QAM. The dotted red lines indicate the target BER that is equivalent to γ_{th}.

the SNR PDF of (4.17) is further used to derive the outage probability for the massive MMO-OFDM system as shown in (4.21). In addition, the BER simulations of Fig. 4.3 is used to obtain the target SNR (γ_{th}) that is equivalent to the target error performance. The simulation of the outage probability derived in (4.21) is depicted in Figs. 4.4 and 4.5 at $BER = 10^{-2}$ and 10^{-4} for BPSK modulation and 16-QAM scheme, respectively. The equivalent target SNR for these modulations and for the selected N_t, N_r combinations of these figures can be listed for the BPSK modulated system as $\gamma_{th} = -5, -9.5, -8.25, -12.5$ for $N_t = 4$ and $\gamma_{th} = -1, -5.5, -4.25, -8.5$ for $N_t = 10$. While for the 16-QAM scheme, the equivalent target SNRs are $\gamma_{th} = -1, -6, -4.5, -9$ for $N_t = 4$ and $\gamma_{th} = 3, -1.5, -0.5, -4.5$ for $N_t = 10$, respectively.

To illustrate, the target SNR for the BPSK modulated system of $N_t = 10$ and $N_r = 100$ at BER=10^{-2} is $\gamma_{th} = -5.5$ dB, and at BER = 10^{-4} the target SNR is $\gamma_{th} = -1$. Similarly, based on the selected target BER, the target SNR can be achieved at any N_t, N_r antenna configuration for the desired massive MIMO-OFDM systems. Inspecting the results at $SNR = -10\ dB$ show that the outage probability $P_{out} = 0.28$ for the case of $N_t = 10, N_r = 100$ at BER=10^{-2}, while $P_{out} = 0.06$ when the BER=10^{-4} as shown in Fig. 4.4 b).

In addition, the simulation of the outage probability for 16-QAM scheme is depicted in Fig. 4.5 at $BER = 10^{-2}$ and 10^{-4}, respectively. The equivalent target SNR for this modulation and for the selected N_t, N_r combination of this figure can be listed as $\gamma_{th} = -1, -4.5, -6, -9$ for $N_t = 4$ and $\gamma_{th} = 3, -0.5, -1.5, -4.5$ for $N_t = 10$, respectively. The results of Fig. 4.5 are obtained by substituting these γ_{th} values in (4.21) for 16-QAM scheme. Similarly, the case of $N_t = 10$ and $N_r = 100$ is depicted in Fig. 4.5 b) at $BER = 10^{-2}$ with $\gamma_{th} = -1.5$ dB, and at BER = 10^{-4} with $\gamma_{th} = 3$. Inspecting these results at $SNR = -5$ dB show that the outage probability $P_{out} = 0.2$ when the BER=10^{-2}, while $P_{out} = 0.04$ when the BER=10^{-4}. The result of Figs. 4.4 and 4.5 is summarized in Table 4.1 for the selected γ parameters at BER = 10^{-2} and 10^{-4}, respectively.

The simulation of the exact capacity and its upper and lower bounds derived in Section 4.2.4 are presented in Figs 4.6 and 4.7 for BPSK modulation, and in Figs 4.8 and 4.9 for 16-QAM scheme. The number of receive and transmit antennas for the test bed was $N_r = 100, 200$ and $N_t = 4, 10$, respectively. These figures demonstrate the increase in the data throughput when the number of transmit and receive antennas are increased and for different modulation types.

In Figs. 4.6 and 4.7, it is observed that the capacity bounds approach the exact closed-
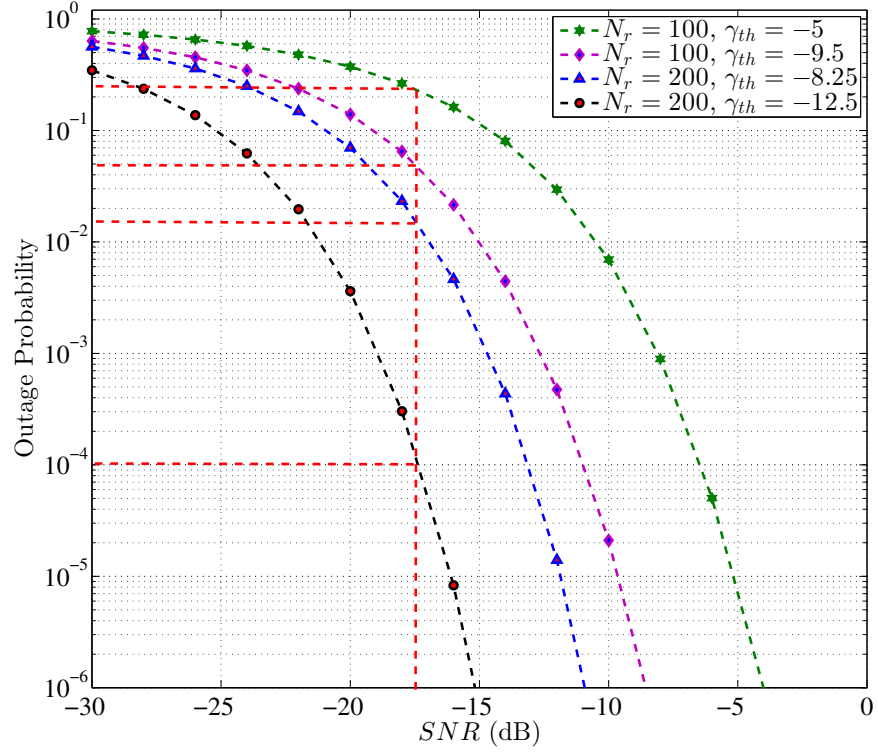
(a) $N_t = 4$ and $N_r = 100, 200$ at $\gamma_{th} = -5, -9.5, -8.25, -12.5$ dB.
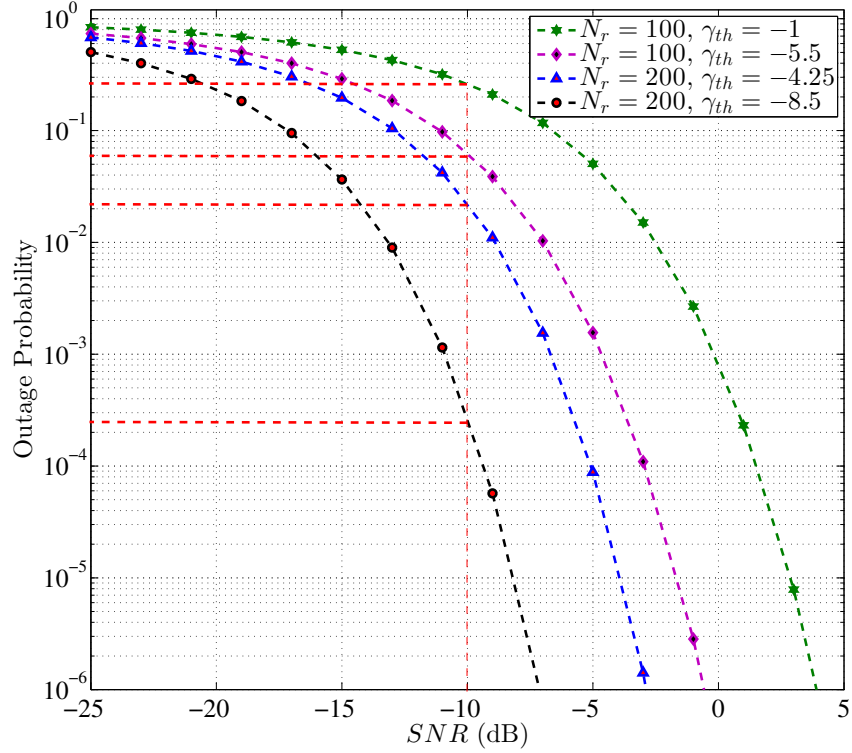
(b) $N_t = 10$ and $N_r = 100, 200$ at $\gamma_{th} = -1, -5.5, -4.25, -8.5$ dB.

Figure 4.4: The outage probability for massive MIMO-OFDM systems at $N_r = 100, 200$ and (a) $N_t = 4$ (b) $N_t = 10$, at BPSK modulation.
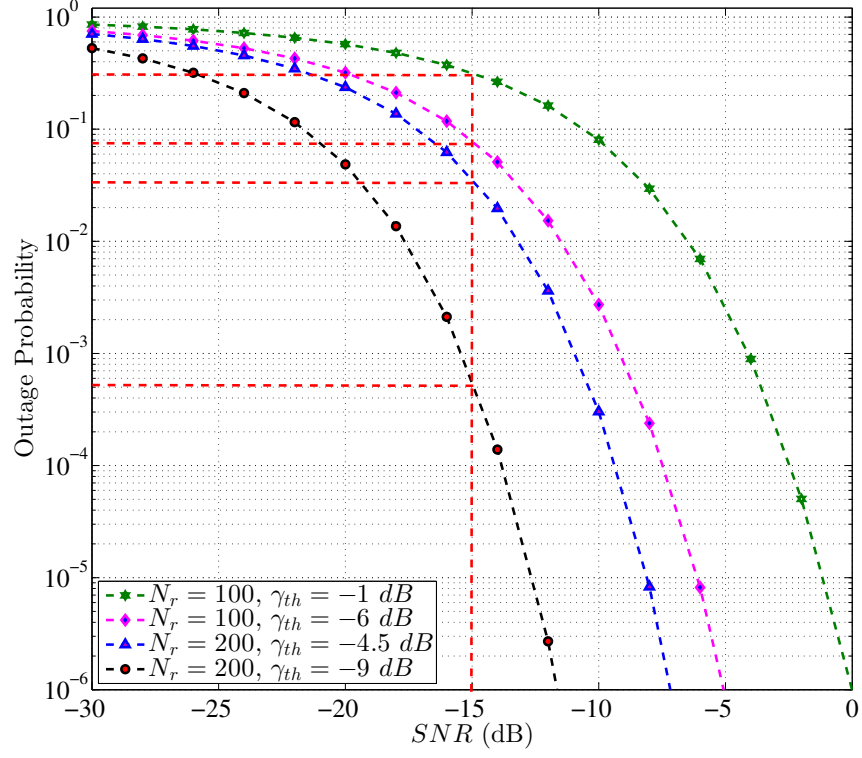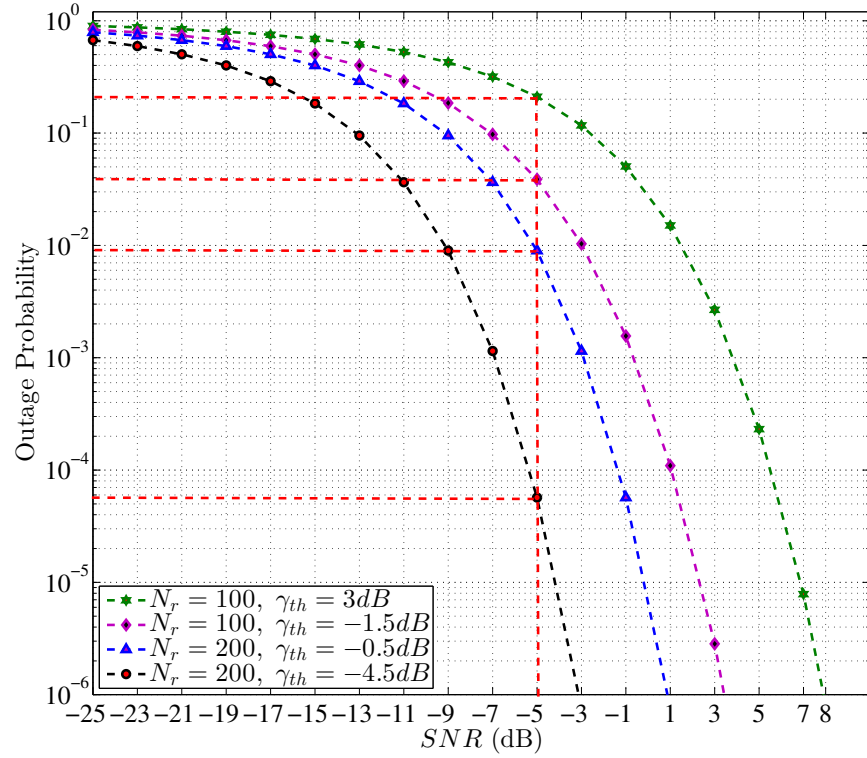
(a) $N_t = 4$ and $N_r = 100, 200$ at $\gamma_{th} = -1, -6, -4.5, -9$ dB.

(b) $N_t = 10$ and $N_r = 100, 200$ at $\gamma_{th} = 3, -1.5, -0.5, -4.5$ dB.

Figure 4.5: The outage probability for massive MIMO-OFDM systems at $N_r = 100, 200$ and (a) $N_t = 4$ (b) $N_t = 10$, at 16-QAM scheme.

Table 4.1: The outage probability of the selected system of Figs. 4.4 and 4.5 for BPSK and 16-QAM schemes, respectively.

	N_t	N_r	BER=10^{-2}		BER=10^{-4}	
			γ_{th}	P_{out}	γ_{th}	P_{out}
BPSK	4	100	-5	0.25	-9.5	0.05
	4	200	-8.25	0.017	-12.5	10^{-4}
	10	100	-1	0.25	-5.5	0.06
	10	200	-4.25	0.22	-8.5	2.5×10^{-4}
16-QAM	4	100	-1	0.3	-6	0.07
	4	200	-4.5	0.03	-9	5.5×10^{-3}
	10	100	3	0.2	-1.5	0.04
	10	200	-0.5	0.009	-4.5	6×10^{-5}

form capacity for the selected SNR range. First, at SNR values higher than -10 dB for $N_t = 4, N_r = 100$, the upper bound of (4.32) become almost identical with the exact capacity, while the lower bounds of (4.25) and (4.29) are approaching the exact closed-form capacity for SNR values less than -27 and -18 dB, respectively.

Similarly, the exact closed-form capacity and its bounds for the 16-QAM scheme are presented in Figs. 4.8 and 4.9. The upper bound of (4.32) approaches the exact capacity for $N_t = 4, N_r = 100$ and $SNR > 0$, while the lower bounds of (4.25) and (4.29) are approaching the exact closed-form capacity for SNR values less than -15 and -8 dB, respectively.

The range of SNR values that result in convergence to the capacity bounds for the selected system of Figs. 4.6 to 4.9 are presented in Table 4.2. Furthermore, it is observed that the derived capacity bounds have better convergence at lower modulations, such as BPSK and 4-QAM.

Table 4.2: Capacity bounds convergence.

	N_t	N_r	Upper Bound	Lower Bound 1	Lower Bound 2
BPSK	4	100	SNR > -10 dB	SNR < -10 dB	SNR < -20 dB
	4	200	SNR > -15 dB	SNR < -15 dB	SNR < -25 dB
	10	100	SNR > -8 dB	SNR < -7 dB	SNR < -16 dB
	10	200	SNR > -10 dB	SNR < -12 dB	SNR < -22 dB
16-QAM	4	100	SNR > -4 dB	SNR < -9 dB	SNR < -15 dB
	4	200	SNR > -5 dB	SNR < -11 dB	SNR < -22 dB
	10	100	SNR > 0 dB	SNR < -6 dB	SNR < -12 dB
	10	200	SNR > -4 dB	SNR < -10 dB	SNR < -16 dB

In Section 4.3.1, the PEP for the coded massive MIMO-OFDM systems is derived based on the noise PDF after the ZFE to be used in the performance estimation of the coded systems. In Section 4.3.2, an upper-bound to the convolutionally coded massive

(a) $N_t = 4$ and $N_r = 100$.

(b) $N_t = 10$ and $N_r = 100$.

Figure 4.6: The Ergodic Capacity for massive MIMO-OFDM systems with BPSK modulation at $N_t = 4, 10$ and $N_r = 100$.

(a) $N_t = 4$ and $N_r = 200$.

(b) $N_t = 10$ and $N_r = 200$.

Figure 4.7: The Ergodic Capacity for massive MIMO-OFDM systems with BPSK modulation at $N_t = 4, 10$ and $N_r = 200$.
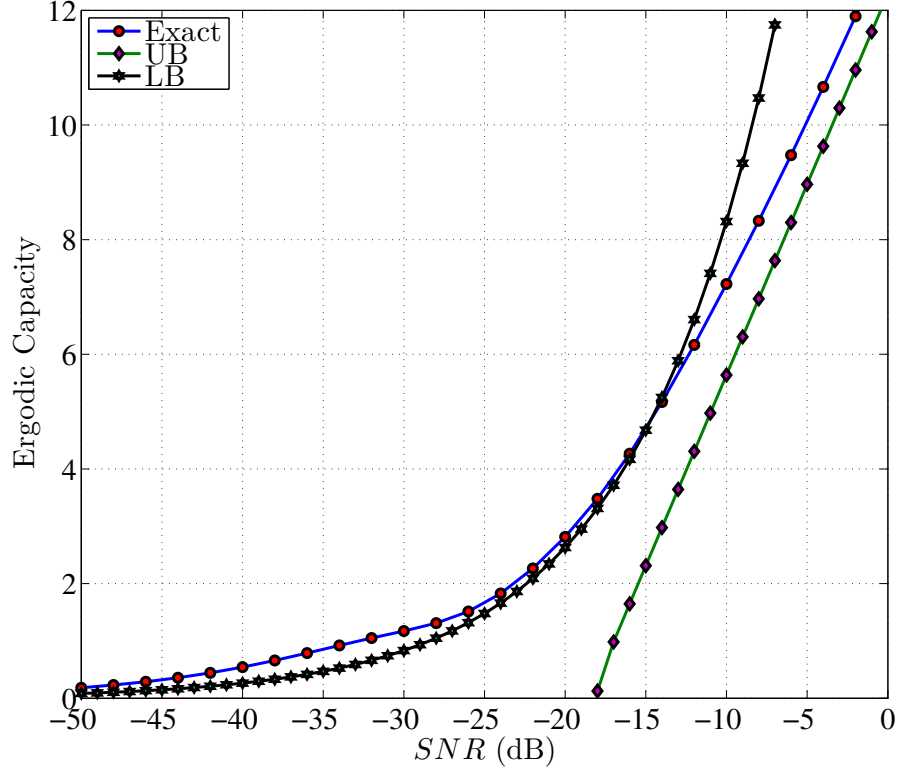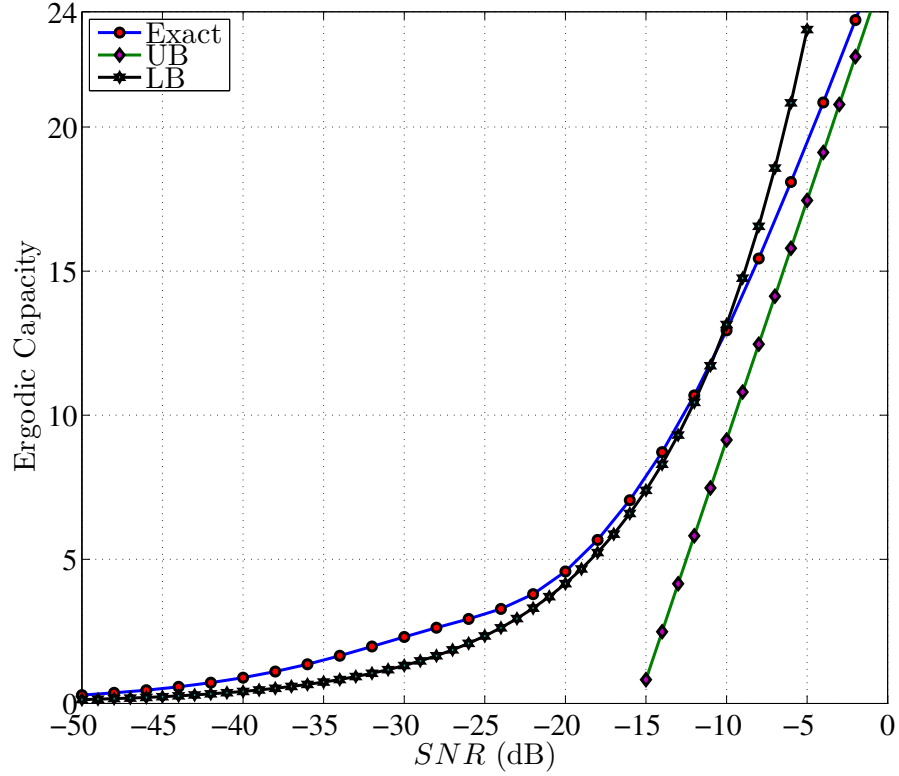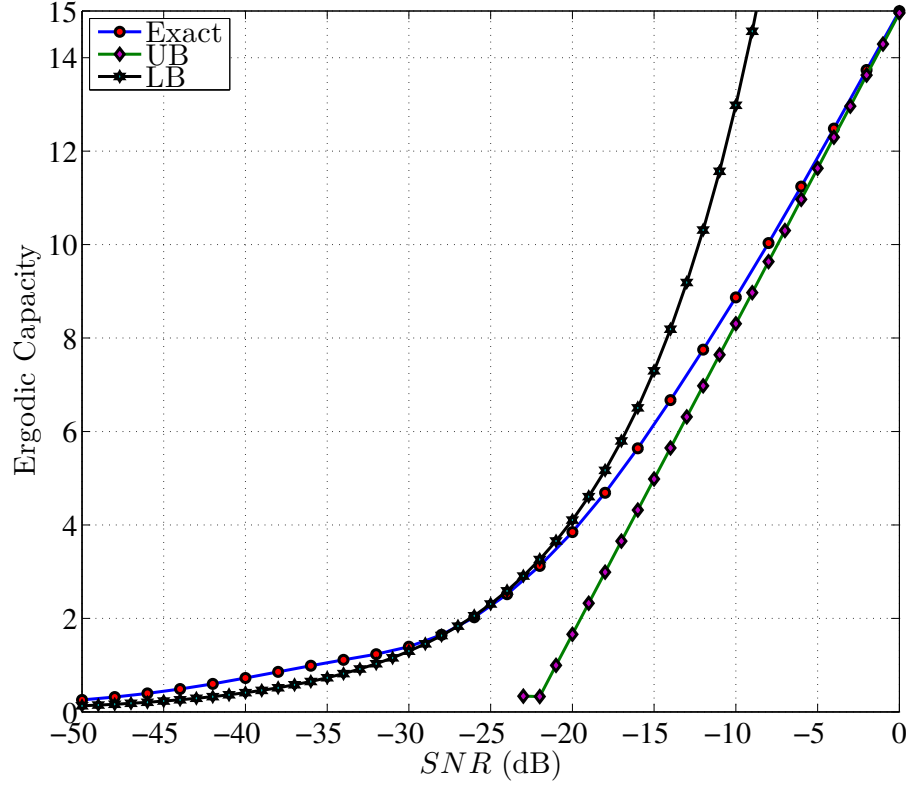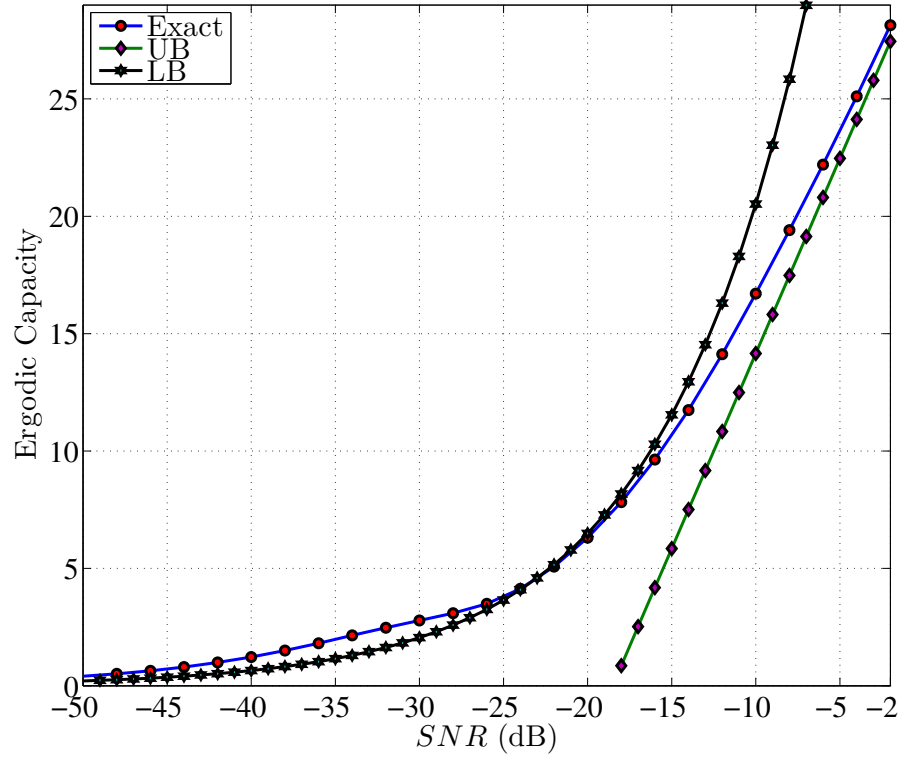
(a) $N_t = 4$ and $N_r = 100$.

(b) $N_t = 10$ and $N_r = 100$.

Figure 4.8: The Ergodic Capacity for massive MIMO-OFDM systems with 16-QAM scheme at $N_t = 4, 10$ and $N_r = 100$.
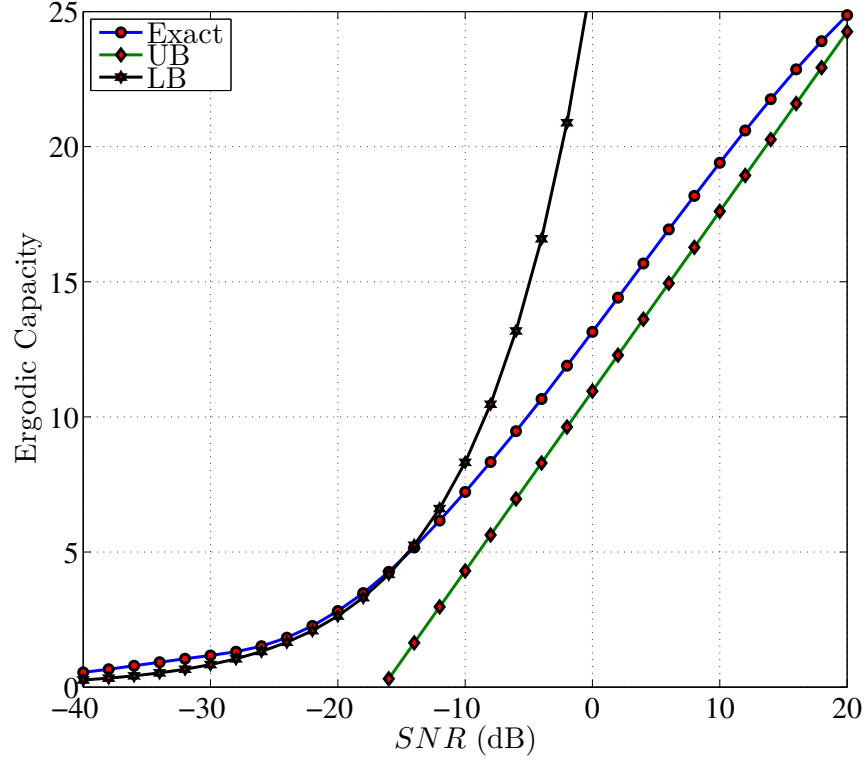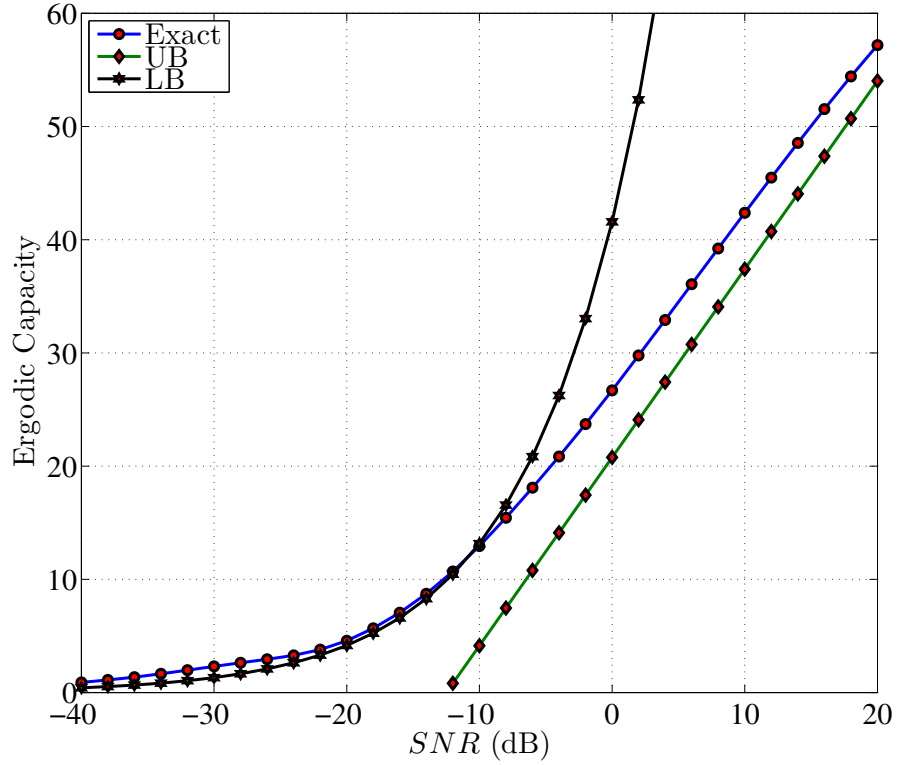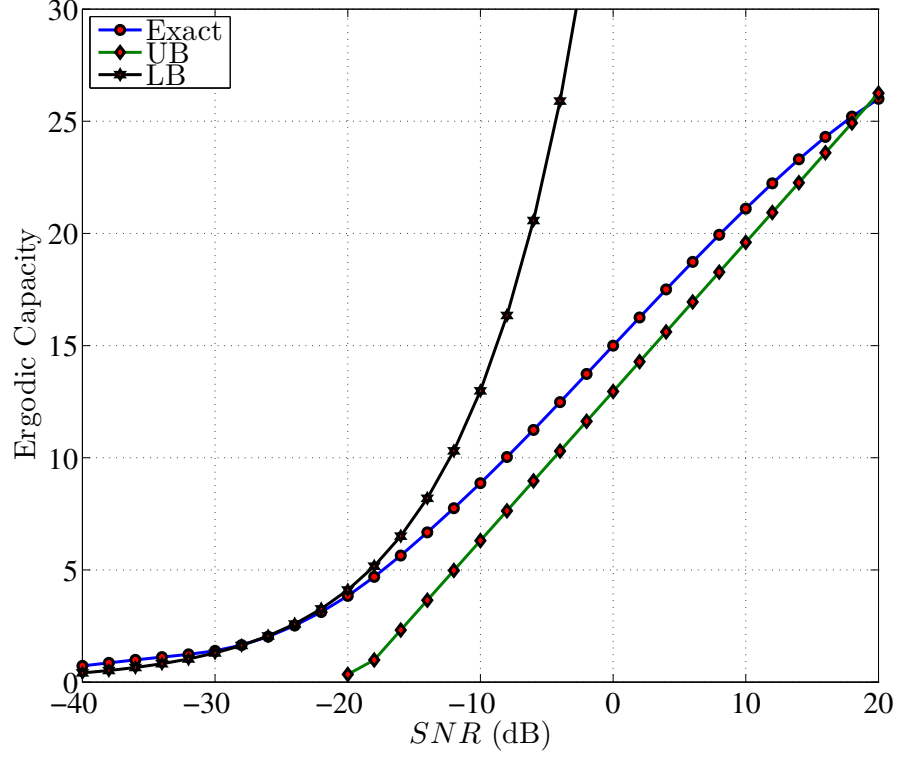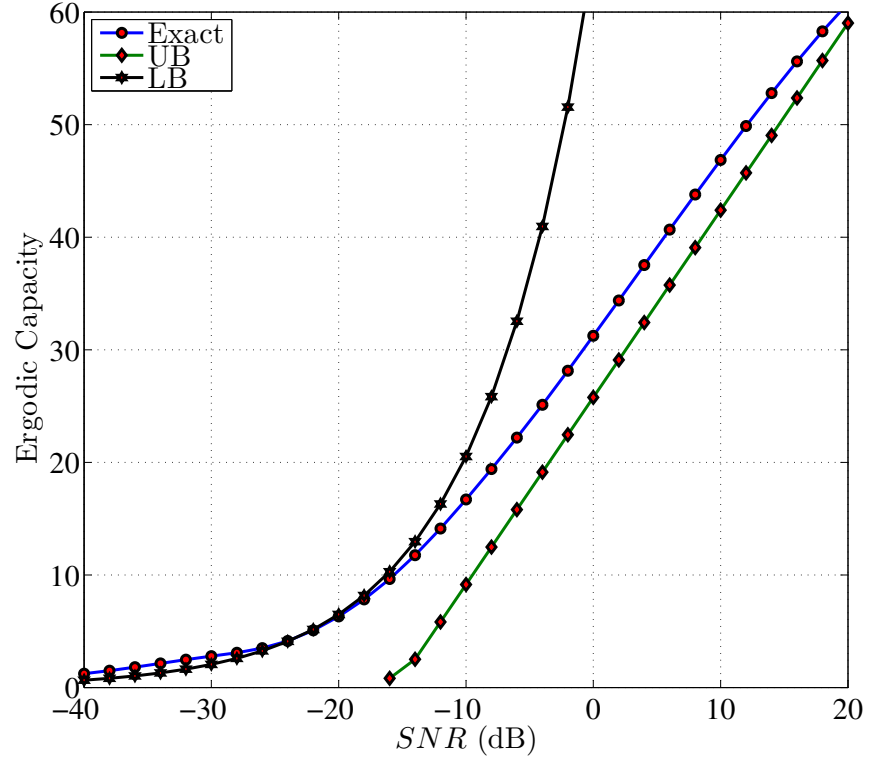
(a) $N_t = 4$ and $N_r = 200$.

(b) $N_t = 10$ and $N_r = 200$.

Figure 4.9: The Ergodic Capacity for massive MIMO-OFDM systems with 16-QAM scheme at $N_t = 4, 10$ and $N_r = 200$.

MIMO-OFDM systems has been derived by adopting this PEP to the error weights derived from the transfer function of the desired convolutional code [96, 97]. It is observed that the upper-bounds in Figs. 4.10 and 4.11 are controlled by the index of c_d in Table A.1 as will be explained next.

First, the performance of Fig. 4.10 is for the convolutional coded massive MIMO-OFDM system with $N_r = 200$ and $N_t = 4$ and 10, respectively. The simulation of this figure shows that when the index of c_d is higher than 10 a divergence in upper-bound performance is occurred that tends to be a straight line to bound the simulation. However, reducing this index will result in a tighter bound that depends on the constraint length of the desired convolutional code. For instance, the $(23, 35)_8$ code has an index of 4, while the $(247, 371)_8$ code has an index of 6.

Second, the performance of Fig. 4.11 is performed to observe the effect of changing the number of receive antennas on the accuracy of the upper bound. In this part, the number of receive antennas is selected as $N_r = 500$ with $N_t = 4, 10$. As a result, the impact of increasing N_r on the upper-bound can be observed in Fig. 4.11b) as a small increase in the index from 6 to 7. However, there is no major change in the performance for the other plots.

In Section 4.3.3, an asymptotic upper-bound to the performance of the turbo coded massive MIMO-OFDM systems is estimated based on the CWEF method described in [103, 102]. The earlier derived PEP is used along with the D_m factors that are derived using the IRWEF and listed in Table 4.3 for the $(5, 7)_8$ PCCC and for different interleaver lengths. The results shown in Figs. 4.12 and 4.13 demonstrate the bound for the turbo coded systems with $N_r = 200, 500$ and $N_t = 4, 10$, respectively. The upper-bound in these figures shows a close match to the highest iteration of the turbo coded massive MIMO-OFDM system with less than 0.15 dB difference in BER performance. It is observed that when the number of transmitting and receiving antennas has been changed, there is no major effect on the performance of the upper-bound. It is also observed that the highest iteration approaches the upper-bound near the 10^{-3} region and stay within that bound, while the other iterations are approaching that limit at different BER.

(a) $(23, 35)_8$.

(b) $(247, 371)_8$

Figure 4.10: Upper-bound for convolutionally coded massive MIMO-OFDM system with $N_t = 4, 10, \ N_r = 200$ for (a) $(23, 35)_8$ (b) $(247, 371)_8$.
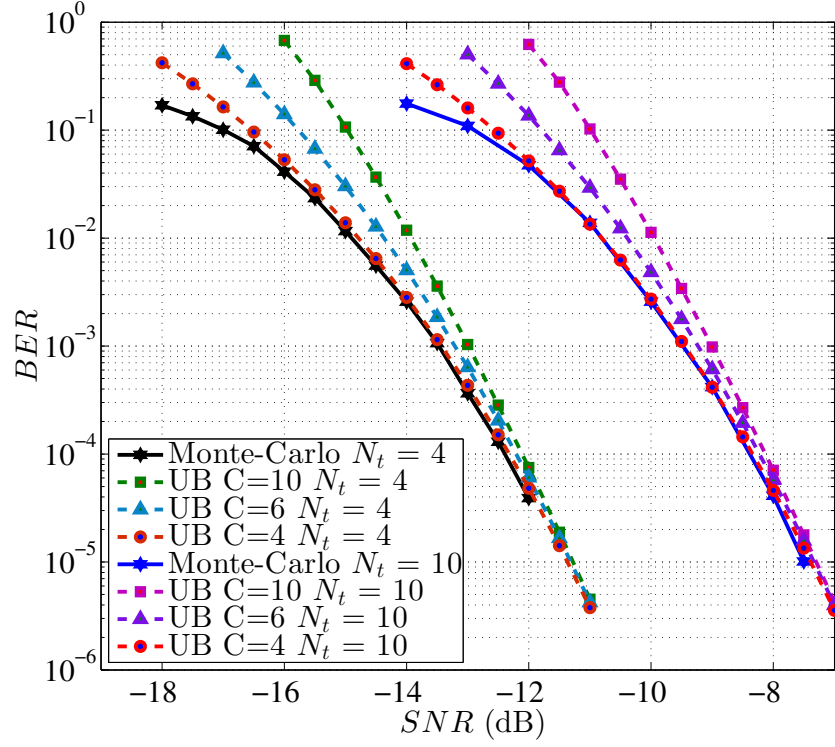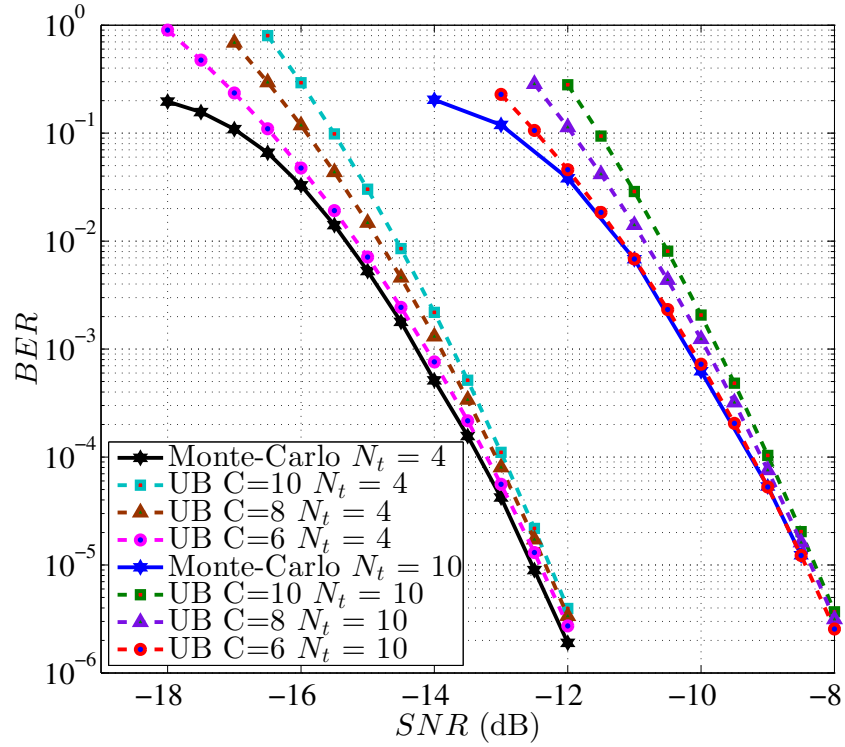
89
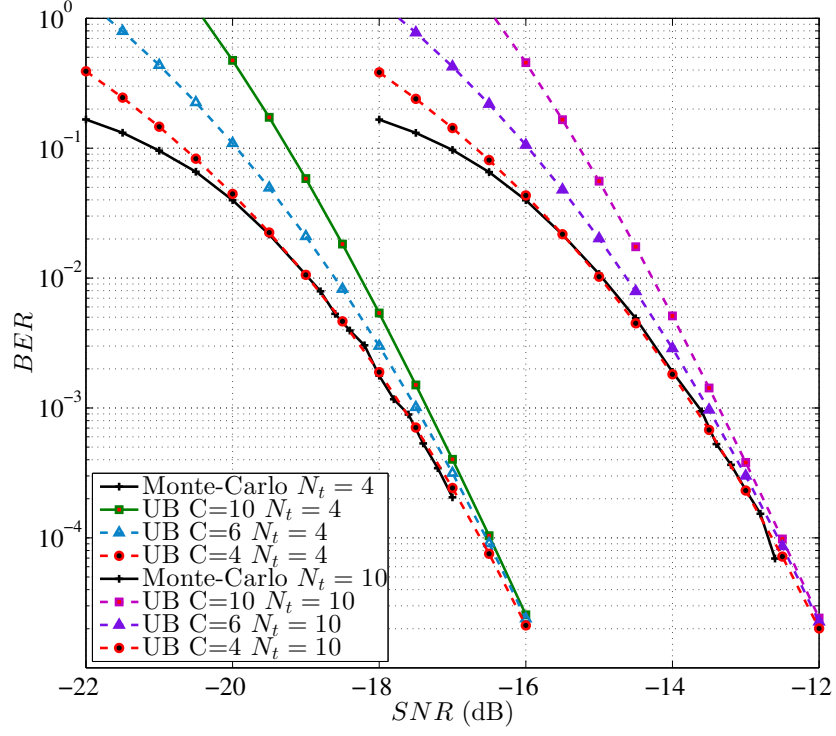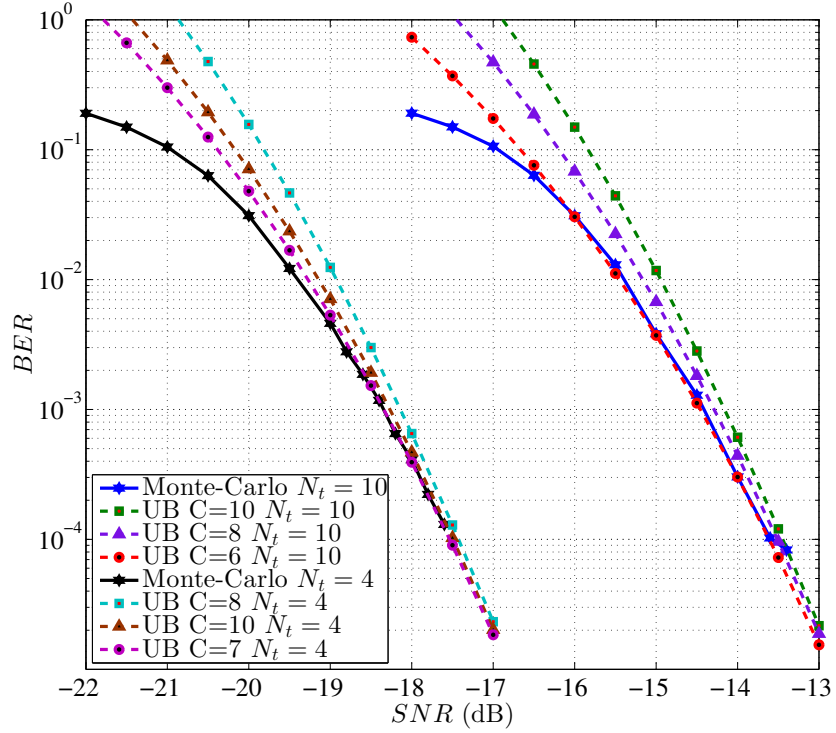
(a) $(23, 35)_8$.

(b) $(247, 371)_8$

Figure 4.11: Upper-bound for convolutionally coded massive MIMO-OFDM system with $N_t = 4, 10$, $N_r = 500$ for (a) $(23, 35)_8$ (b) $(247, 371)_8$.

Table 4.3: D_m coefficients for the BER evaluation of the PCCC [102].

Hamming distance	N_π		
	100	1000	10000
8	3.8900 E-02	3.9881 E-03	3.9988 E-04
9	7.6590 E-02	7.9605 E-03	7.9960 E-04
10	0.1136	1.1918 E-02	1.1991 E-03
11	0.1508	1.5861 E-02	1.5985 E-03
12	0.1986	1.9887 E-02	1.9987 E-03
13	0.2756	2.4188 E-02	2.4017 E-03
14	0.4079	2.9048 E-02	2.8102 E-03
15	0.6292	3.4846 E-02	3.2281 E-03
16	1.197	6.5768 E-02	6.0575 E-03
17	2.359	0.1457	1.3697 E-02
18	4.383	0.2984	2.8543 E-02
19	7.599	0.5472	5.2989 E-02
20	12.58	0.9171	8.9441 E-02
21	20.46	1.437	0.1403
22	33.31	2.144	0.2082
23	54.65	3.090	0.2957
24	91.23	4.465	0.4177
25	154.9	6.716	0.6133
26	265.5	10.67	0.9577
27	455.6	17.65	1.574
28	779	29.61	2.646
29	1327	49.31	4.430
30	2257	80.57	7.267
31	3842	128.6	11.60
32	6556	201.3	18.04
33	11221	311.5	27.57
34	19261	481.2	41.88
35	33143	748.8	63.94

4.5   Chapter Summary

In this chapter, the BER for massive MIMO-OFDM systems is derived by using the effective noise PDF after the ZFE in (3.37) for different modulation types. This BER is verified using the Monte-Carlo simulations of different transmit and receive antenna combinations and the results have shown a close match between the empirical and theoretical plots.

In addition, the PDF of the SNR after the ZFE is obtained using the noise PDF derived in (3.37). Then this PDF is used to derive the outage probability and the channel capacity for the massive MIMO-OFDM systems. In addition, an upper and two lower bounds were derived for the channel capacity based on different assumptions and their performance were compared to the exact capacity. The simulation results verified the accuracy of the derived equations, and the upper bounds have successfully approached the exact capacity
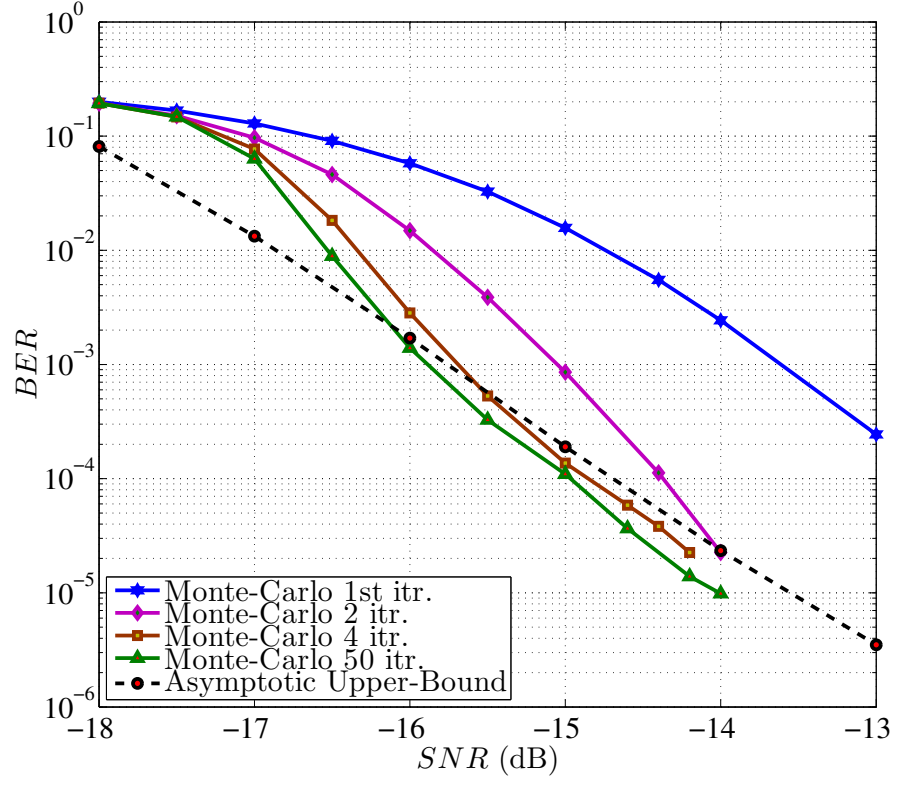
(a) $N_t = 4$, $N_r = 200$
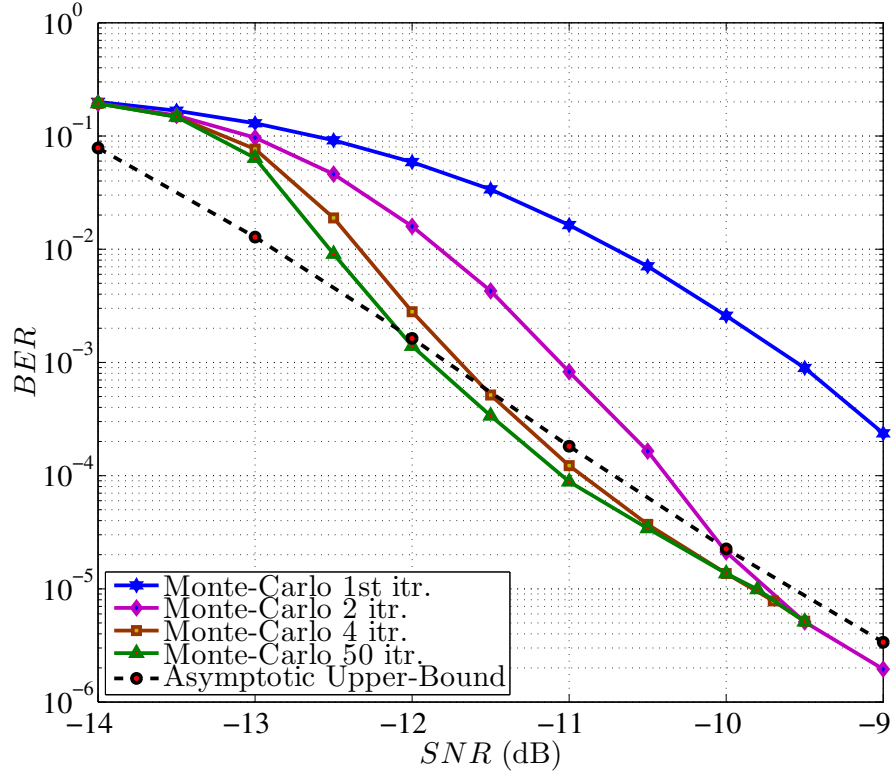
(b) $N_t = 10$, $N_r = 200$

Figure 4.12: Asymptotic Upper-Bound turbo coded massive MIMO-OFDM system with $(5, 7)_8$ generator and $N_r = 200$ for (a) $N_t = 4$ (b) $N_t = 10$.
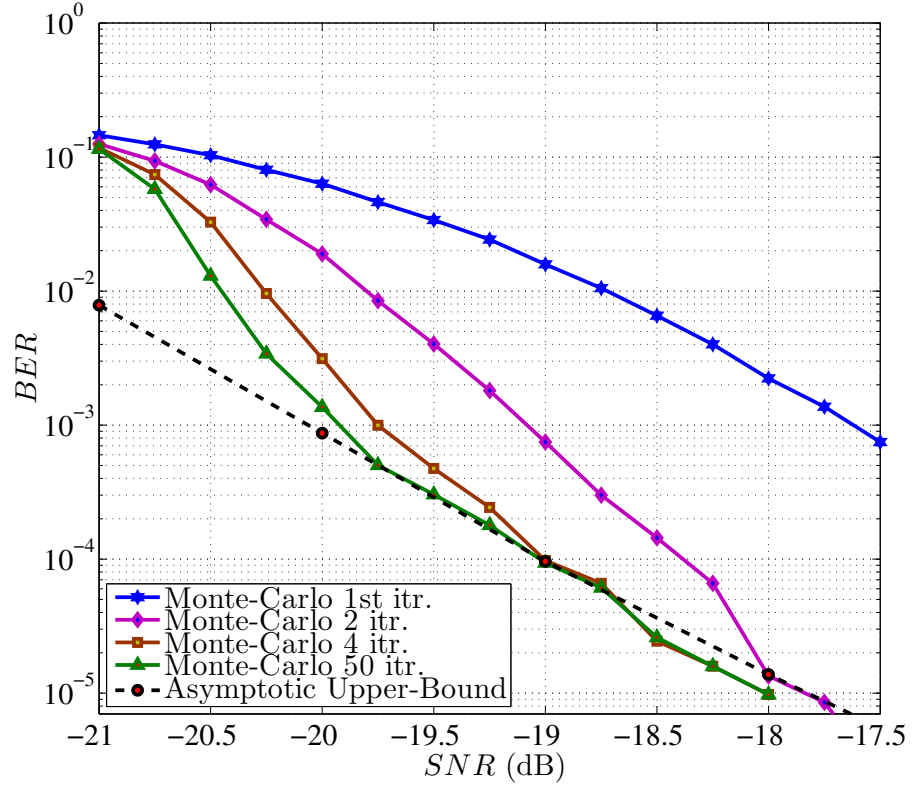
(a) $N_t = 4,\ N_r = 500$
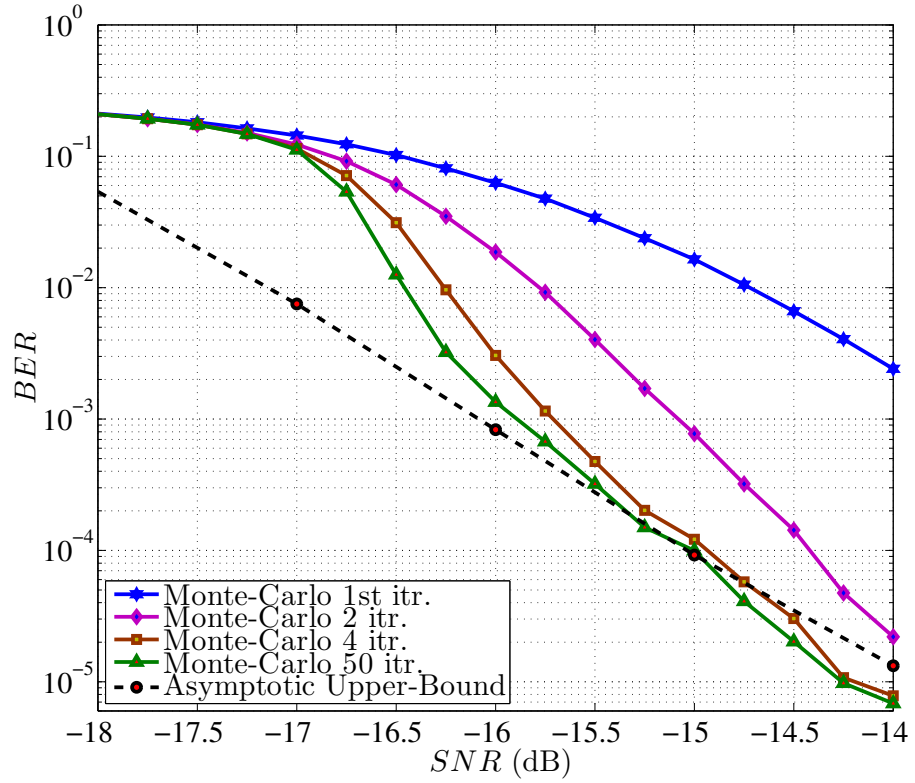
(b) $N_t = 10,\ N_r = 500$

Figure 4.13: Asymptotic Upper-Bound turbo coded massive MIMO-OFDM system with $(5, 7)_8$ generator and $N_r = 500$ for (a) $N_t = 4$ (b) $N_t = 10$.

within the selected range.

The PEP is derived for the coded system and used to obtain an upper-bound for convolutionally encoded massive MIMO-OFDM systems. The results have bounded the performance for different error weight values and indices, and the upper-bound performance became very tight for the two selected codes. In addition, the turbo coded system is bounded within 0.15 dB of the Monte-Carlo simulations by using the derived PEP and the D_m terms given for the $(5, 7)_8$ PCCC using BPSK/4-QAM modulation.

Chapter 5

Fixed-Point Arithmetic Detectors for Massive MIMO-OFDM Systems

5.1   Introduction

Massive MIMO systems have become a key technology for future generations of wireless communications. Research in such systems is fuelled by the increased data rate requirements of modern multimedia applications. One of the major challenges in massive MIMO transmission is the increase in the computational complexity at the receiver due to the high number of receiving antennas, especially when using sophisticated non-linear demodulation schemes such as successive interference cancellation and sphere detectors. On the other hand, linear detectors require fewer operations without significantly compromising performance. Past researches [110, 111] have been conducted to show the behaviour of the MIMO system with few antennas at both sides (4x4) using MMSE utilizing a QR decomposition (QRD) detector in a coded system with a hardware implementation. On the other hand, a QRD based Vertical-Bell Laboratories Layered Space-Time (V-BLAST) detector has been implemented in [112], which takes the fixed point very large scale integration (VLSI) implementation into consideration with 4 antennas at both the transmitter and receiver. In other papers, [113] implemented the SD without using any decomposition scheme, while [114, 115] used fixed point arithmetic with QRD and Cholesky decomposition. Furthermore, in [116, 117], different techniques have been used with fixed point arithmetic to implement the MIMO system as FPGA system or as VLSI. Finally, a large scale implementation for the massive MIMO receiver with fixed point representation [67] has used on FPGA system with reduced complexity Neumann series expansion to reduce the implementation complexity. The MIMO detector for the coded massive MIMO-OFDM system in Chapters 3 and 4 of this thesis was ZFE with soft modulation that is derived based on Neumann matrix inversion method.

The contribution of this chapter can be summarized in the following points,

- Different decomposition schemes are used for detection in a massive MIMO-OFDM system with fixed point arithmetic to simulate the hardware implementation.

- The standard IEEE 754 double and half precision with a word length of 64 and 16 bits are used in the simulations in addition to a user-defined precision of 12 and 10 bits to verify the ability of each detector. In addition, the complexity required by each detector are estimated and tabulated.
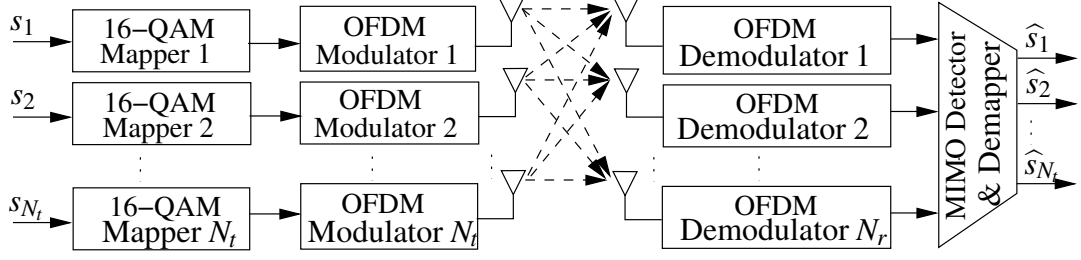
Figure 5.1: Massive MIMO-OFDM Transceiver.

5.2 System Model

In this chapter, the uplink $N_r \times N_t$ MIMO-OFDM system depicted in Fig. 5.1 is considered, where N_t and N_r represent the number of transmitting and receiving antennas, respectively, with $N_r >> N_t$. After OFDM demodulation, i.e. removing the CP and performing the FFT operation, the received signal can be given as

$$\mathbf{x}_k = \mathbf{H}_k\mathbf{s}_k + \mathbf{W}_k, \tag{5.1}$$

where $\mathbf{x}_k \in \mathbb{C}^{N_r \times 1}$ are the received signal samples in frequency domain, $\mathbf{s}_k \in \mathbb{C}^{N_t \times 1}$ are the transmitted information symbols that are modulated using M-QAM scheme, $\mathbf{H}_k \in \mathbb{C}^{N_r \times N_t}$ is the channel matrix in frequency domain for the k-th FFT sub-carrier, where $k = 1, 2, \cdots, K$, and finally, $\mathbf{W}_k \in \mathbb{C}^{N_r \times 1}$ is the FFT of the additive white Gaussian noise (AWGN) samples in time domain. The detected information symbols are obtained using

$$\hat{\mathbf{s}}_k = \mathbf{H}_k^{\dagger}\mathbf{x}_k, \tag{5.2}$$

where $\mathbf{H}^{\dagger}$ denotes the pseudoinverse of $\mathbf{H}$ if $N_r \neq N_t$ and $\mathbf{H}^{\dagger} = \mathbf{H}^{-1}$ if $N_r = N_t$. It is worth noting that the index k will be removed from the subsequent equations to maintain simplicity. It is assumed that signals propagate through frequency selective fading channels that are not time selective over the OFDM symbol duration.

5.3 MIMO Detectors

The aim of the MIMO detector is to recover the transmitted symbols, $\hat{\mathbf{s}}$, with the lowest probability of error by utilizing the lowest level of precision in the receiver using different decomposition schemes. This has been motivated by the need to reduce the number of bit representations required in the detection of the massive MIMO system in order to reduce

the hardware implementation and power consumption requirements. The number of operations required by these detectors can be very large and their computational complexity cost will be very high if implemented with double or single precision representation.

5.3.1 ZFE Detector

The matrix inversion method used here is the iterative Moore-Penrose pseudo inverse method [118] that has the advantage of reduced complexity detection compared to other types of MIMO detectors. This procedure is illustrated in Algorithm 3 and depends on successive steps to calculate the inverse of rank $N-1$ to the matrix of rank N. This, in turn, reduces the complexity of calculations as described later in this chapter. The general ZFE equation can be written as

$$\mathbf{H}_{ZFE}^{-1} = (\mathbf{H}^H \mathbf{H})^{-1} \mathbf{H}^H, \tag{5.3}$$

where the term $(\mathbf{H}^H \mathbf{H})$ represents the Gram matrix, which is a symmetrical positive definite square matrix. Accordingly, Cholesky, LU and LDLT factorization can be used to implement the inverse of these matrices in addition to a Neumann approximation.

Algorithm 3 : Iterative ZFE Detector

1: **procedure** $A_{inv} = pinv(A)$
2:     $set \ \ k = 1$
3:       $A_k = a_k$
4:       $A_k^\dagger = (A_k^H A_k)^{-1} A_k^H$
5:   **for** $k \leftarrow 2 \ \ to \ \ N$ **do**
6:       $c_k = (I - A_{k-1} A_{k-1}^\dagger) a_k$
7:       $\gamma_k = a_k^H (A_{k-1}^H)^\dagger A_{k-1}^\dagger a_k$
8:       $b_k = \begin{cases} c_k^\dagger, & \text{if } \ c_k \neq 0, \\ (1+\gamma)^{-1} a_k^H (A_{k-1}^H)^\dagger A_{k-1}^\dagger, & \text{if } \ x = 0. \end{cases}$
9:       $A_k^\dagger = \begin{bmatrix} A_{k-1}^\dagger - A_{k-1}^\dagger a_k b_k \\ b_k \end{bmatrix}$
10:   **end for**
11:     $A_{inv} \leftarrow A_k^\dagger$

The implementation of the ZFE and MMSE detectors can be achieved based on different decomposition techniques utilizing Gram matrix, that is

$$\mathbf{A} = \begin{cases} (\mathbf{H}^H \mathbf{H}) & \text{for} \quad ZFE, \\ (\mathbf{H}^H \mathbf{H} + \sigma^2 \mathbf{I}_N) & \text{for} \quad MMSE. \end{cases} \tag{5.4}$$

According to that, Cholesky, LU and LDLT factorization can be applied to implement the

inverse for these matrices as will be illustrated next.

5.3.2 Cholesky Factorization Based Detector

Each positive definite symmetric matrix has a special factorization that exploits its definite and symmetry which called Cholesky factorization [40, 119]. This factorization can be applied to $\mathbf{A}$ matrix to get

$$\mathbf{A} = \mathbf{L}\mathbf{L}^H, \tag{5.5}$$

where $\mathbf{L}$ is a lower triangular matrix. The inverse of this decomposition can be calculated using

$$\mathbf{A}^{-1} = (\mathbf{L}^H)^{-1}\mathbf{L}^{-1} = (\mathbf{L}^{-1})^H\mathbf{L}^{-1}, \tag{5.6}$$

which will require calculating the inverse of a lower triangular matrix $\mathbf{L}$ once. The efficient way to implement the inverse of this matrix is to use the block matrix inversion method shown below

$$\mathbf{L}^{-1} = \begin{bmatrix} \mathbf{L}_{11} & \mathbf{0} \\ \mathbf{L}_{21} & \mathbf{L}_{22} \end{bmatrix}^{-1} = \begin{bmatrix} \mathbf{L}_{11}^{-1} & \mathbf{0} \\ -\mathbf{L}_{11}^{-1}\mathbf{L}_{21}\mathbf{L}_{22}^{-1} & \mathbf{L}_{22}^{-1} \end{bmatrix}. \tag{5.7}$$

According to this, only two matrix inversions with size $N/2$ are required to find the inverse of the lower triangle matrix. This inversion technique is applied here to the relevant decomposition schemes such as the LU and the pivoted LDLT factorization to reduced the complexity of inversion. Algorithm 4 demonstrates the procedure of calculating the lower and upper triangular matrix inversion.

Algorithm 4 Triangular matrix inverse

    procedure $F_{inv} = Tri\_inv(F, \,'option')$
        if $(Lower \leftarrow option)$ **then**
$$\mathbf{F} = \begin{bmatrix} \mathbf{F}_{11} & \mathbf{0} \\ \mathbf{F}_{21} & \mathbf{F22} \end{bmatrix},$$
$$\mathbf{F}_{inv} = \begin{bmatrix} \mathbf{F}_{11}^{-1} & \mathbf{0} \\ -\mathbf{F}_{11}^{-1}\mathbf{F}_{21}\mathbf{F22}^{-1} & \mathbf{F22}^{-1} \end{bmatrix}.$$
        else if $(Upper \leftarrow option)$ **then**
$$\mathbf{F} = \begin{bmatrix} \mathbf{F}_{11} & \mathbf{F}_{12} \\ \mathbf{0} & \mathbf{F}_{22} \end{bmatrix},$$
$$\mathbf{F}_{inv} = \begin{bmatrix} \mathbf{F}_{11}^{-1} & -\mathbf{F}_{22}^{-1}\mathbf{F}_{12}\mathbf{F}_{11}^{-1} \\ \mathbf{0} & \mathbf{F}_{22}^{-1} \end{bmatrix}.$$
        end if
        Return $\mathbf{F}_{inv}$

5.3.3   LU Factorization Based Detector

Linear system solutions can be made easier if it involves triangular matrix in its design. LU factorization is a method that can be used to rewrite the matrix $\mathbf{A}_i$ in a (Lower-Upper) triangular matrix form. This decomposition method is limited to the square matrices and it is applied here to the Gram matrix shown in (5.4) such that

$$\mathbf{A} = \mathbf{LU} \,, \tag{5.8}$$

where $\mathbf{L}$ and $\mathbf{U}$ are the lower and upper matrices of LU decomposition. Block matrix inversion method is used here to find the upper and the lower triangular matrix inverse. The inverse of the lower matrix $\mathbf{L}$ can be obtained using (5.7) while the upper triangular matrix $\mathbf{U}$ can be calculated using

$$\mathbf{U}^{-1} = \begin{bmatrix} \mathbf{U}_{11} & \mathbf{U}_{12} \\ \mathbf{0} & \mathbf{U}_{22} \end{bmatrix} = \begin{bmatrix} \mathbf{U}_{11}^{-1} & -\mathbf{U}_{22}^{-1}\mathbf{U}_{12}\mathbf{U}_{11}^{-1} \\ \mathbf{0} & \mathbf{U}_{22}^{-1} \end{bmatrix} , \tag{5.9}$$

and the matrix inversion using LU factorization for Gram matrix can be calculated using

$$\mathbf{A_i}^{-1} = \mathbf{U_i}^{-1}\mathbf{L_i}^{-1} \,. \tag{5.10}$$

5.3.4   LDLT Factorization with Symmetric Pivoting Based Detector

This factorization consists of a lower triangular matrix $\mathbf{L}$ and a diagonal $\mathbf{D}$ matrix with matrix pivoting $\mathbf{P}$ to ensure the symmetric positive definite condition of Gram matrix $\mathbf{A}$ as [40, 120]

$$\mathbf{A} = \mathbf{PLDL}^H\mathbf{P}^H \,, \tag{5.11}$$

where, $\mathbf{P}, \mathbf{L}$ and $\mathbf{D}$ are the permutation orthonormal matrix, the lower triangular matrix and the diagonal matrix of LDLT decomposition of $\mathbf{A}$. Calculating the matrix inversion based on this factorization has the form

$$\mathbf{A}^{-1} = \mathbf{P}^H(\mathbf{L}^{-1})^H\mathbf{D}^{-1}\mathbf{L}^{-1}\mathbf{P} \,. \tag{5.12}$$

The lower matrix inversion can be calculated once again using (5.7) and the rest of the operations are only a sparse matrix multiplication. The main purpose of using the orthonormal permutation matrices in this equation is to maintain the matrix symmetry and

positively defined.

5.3.5 Gram Matrix Based Detector

In this MIMO detector, the LU, Cholesky, and LDLT factorization techniques are used to calculate the Gram matrix inverse. This detector will be used to investigate the effect of these decomposition schemes on the performance of the fixed point MIMO detector. Algorithm 5 was used in the simulation with fixed point design to compare the performance of these detectors. Since all of these detectors involve a triangular matrix inverse, a block matrix inverse procedure (Tri_inv) was used to reduce the complexity of inversion to the one-half of the full matrix inversion complexity as shown in Algorithm 4.

Algorithm 5 : Gram matrix inverse

   procedure $A_{inv} = Gram\_inv(\mathbf{A}, \,'option')$
      if $(LU \leftarrow option)$ **then**
         $\mathbf{A} = \mathbf{LU}$,
         $\mathbf{L}_{inv} = Tri\_inv(\mathbf{L}, \,'Lower')$,
         $\mathbf{U}_{inv} = Tri\_inv(\mathbf{U}, \,'Upper')$,
         $A_{inv} = \mathbf{U_{inv}L_{inv}}$,
      else if $(Cholesky \leftarrow option)$ **then**
         $\mathbf{A} = \mathbf{LL^H}$,
         $\mathbf{L}_{inv} = Tri\_inv(\mathbf{L}, \,'Lower')$,
         $A_{inv} = \mathbf{(L_{inv})^H L_{inv}}$,
      else if $(LDLT \leftarrow option)$ **then**
         $\mathbf{A} = \mathbf{PLDL^H P^H}$,
         $\mathbf{L}_{inv} = Tri\_inv(\mathbf{L}, \,'Lower')$,
         $\mathbf{D}_{inv} = diag(1./diag(\mathbf{D}))$,
         $A_{inv} = \mathbf{P^H L_{inv}^H D_{inv} L_{inv} P}$,
      end if
      Return $\mathbf{A_{inv}}$

5.3.6 Neumann-Series Approximation

This method has been demonstrated previously in Section 3.4. The results obtained here are based on previous studies [5, 67, 121], that used n limit as $n = 1, 2$, and 3 with large matrix size. The increase in the receiver diversity in the aforementioned system improves the system performance at low values of n. The procedure that is used to simulate this detector is illustrated in Algorithm 6 for the channel matrix $\mathbf{H}$ and for n limit. Based on Neumann approximation method, the number of columns and rows have to be $N_r \geq N_t$. However, if this condition has not satisfied, then step 6 will solve this issue by calculating

Gram matrix for the transpose of $\mathbf{H}$. This algorithm depends mainly on the diagonal dependent property of the Gram matrix when the number of columns is higher than the number of rows.

Algorithm 6 : Neumann Approximation

1: **procedure** $\mathbf{H}_{inv} = Neu\_inv(\mathbf{H}, n)$
2:   $[N_r, N_t] = size(\mathbf{H})$
3:   **if** $N_r \geq N_t$ **then**
4:     $\mathbf{B} = \mathbf{H}^H \mathbf{H}$,
5:   **else if** $N_r < N_t$ **then**
6:     $\mathbf{C} = \mathbf{H}^T, \mathbf{B} = \mathbf{C}^H \mathbf{C}$,
7:   **end if**
8:   $\mathbf{D} = diag(\mathbf{B})$,
9:   $\mathbf{E} = \mathbf{B} - \mathbf{D}$,
10:   $\mathbf{D}_{inv} = 1/\mathbf{D}$,
11:   **Initialization:**
12:   $\mathbf{Sum} = \mathbf{D}_{inv}, \mathbf{Mul} = -\mathbf{D}_{inv} \cdot \mathbf{E}$,
13:   **For** $k = 1$ **to** n
14:   $\mathbf{Sum} = \mathbf{Sum} + \mathbf{Mul} \cdot \mathbf{D}_{inv}$,
15:   $\mathbf{Mul} = (-\mathbf{D}_{inv} \cdot \mathbf{E}) \cdot \mathbf{Mul}$,
16:   **end for**
17:   **if** $N_r \geq N_t$ **then**
18:     $\mathbf{H}_{inv} = \mathbf{Sum} \cdot \mathbf{H}^H$,
19:   **else if** $N_r < N_t$ **then**
20:     $\mathbf{C}_{inv} = \mathbf{Sum} \cdot \mathbf{C}^H$,
21:     $\mathbf{H}_{inv} = \mathbf{C}_{inv}^T$
22:   **end if**
23:   **Return** $\mathbf{H}_{inv}$.

5.3.7   QR Factorization Based Detector (QRD)

The QRD is used here as a SIC with the MGS procedure as demonstrated in Section 2.4.3.1, in which matrix $\mathbf{Q} \in \mathbb{C}^{N_r \times N_t}$ and the upper triangular matrix $\mathbf{R} \in \mathbb{C}^{N_t \times N_t}$[122] are the QR-factorization of $\mathbf{H}$. The transmitted signal here can be recovered by using Algorithm 7 which will first multiply the received signal by the Hermitian of the orthonormal matrix $\mathbf{Q}$. Then, the back substitution procedure reconstructs the transmitted streams completely in N_t steps.

5.4   Fixed Point Representation

The aim of this chapter is to show the performance of different decomposition schemes used in MIMO detectors to equalize the channel effects. The fixed point calculations are applied to the output of the FFT of the channel matrix and the received signal in addition

---

Algorithm 7 : QRD-SIC

1: **procedure** $\tilde{s} = SIC(\mathbf{H}, \mathbf{x})$
2: $\quad$ $\mathbf{QR} \leftarrow \mathbf{H}$
3: $\quad$ $\mathbf{y} = \mathbf{Q}^{\mathbf{H}}\mathbf{x} = \mathbf{Rs} + \mathbf{Q}^{\mathbf{H}}\mathbf{n}$
4: $\quad$ $\begin{bmatrix} y_1 \\ y_2 \\ \vdots \\ y_{N_t} \end{bmatrix} \cong \begin{bmatrix} r_{11} & r_{12} & \cdots & r_{1N_t} \\ 0 & r_{22} & \cdots & r_{2N_t} \\ \vdots & \vdots & \ddots & \\ 0 & 0 & \cdots & r_{N_t N_t} \end{bmatrix} \begin{bmatrix} s_1 \\ s_2 \\ \vdots \\ s_{N_t} \end{bmatrix},$
5: $\quad$ $\tilde{s}_{N_t} = \dfrac{y_{N_t}}{r_{N_t N_t}},$
6: $\quad$ $\tilde{s}_{N_t - 1} = \dfrac{y_{N_t - 1} - r_{N_t - 1 N_t} \tilde{s}_{N_t}}{r_{N_t - 1 N_t - 1}},$
7: $\quad$ $\vdots$
8: $\quad$ $\tilde{s}_1 = \dfrac{y_1 - \cdots - r_{1N_t} \tilde{s}_{N_t}}{r_{11}}.$
9: $\quad$ **Return** $\tilde{s}$.
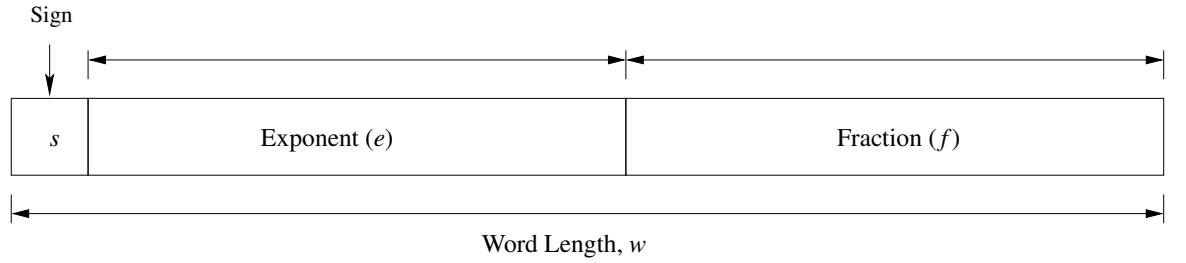
Figure 5.2: Numbers representation with fixed point arithmetic.

to the decomposition schemes above to simulate the behavior of the implemented MIMO detector.

The standard IEEE 754 precision can be divided according to Fig. 5.2 into half, single, double and quadruple precision [123]. The first three of the latter are the most popular types and can be represented using

$$X = (-1)^s (1 + \sum_{i=1}^{f} b_{f-i} 2^{-i}) 2^{e-z} , \qquad (5.13)$$

where s is the sign, and e, f and z are the exponent, fraction length and the zero-offset for that number, respectively. The zero-offset equals to $z = 2^{e-1} - 1$, which is 1023 and 15 for double and half precision, respectively. The user-defined precision enables the use of different levels of accuracy depending on the required word length to be used. A word length of 12 bits and 10 bits were used to verify the performance of each detector at a reduced precision detection.

The effect of reducing the precision on the mathematical calculations can be illustrated

using matrix $\mathbf{A}$ with 4×2 dimensions such that

$$\mathbf{A} = \begin{bmatrix} 0.5377 & 0.3188 \\ 1.8339 & -1.3077 \\ -2.2588 & -0.4336 \\ 0.8622 & 0.3426 \end{bmatrix}.$$

Calculating the pseudo-inverse of this matrix with double precision format results in

$$\mathbf{B} = \begin{bmatrix} 0.0751 & 0.1374 & -0.2705 & 0.1120 \\ 0.1843 & -0.5559 & -0.3265 & 0.2122 \end{bmatrix},$$

while at half precision, the pseudo-inverse can be written as

$$\tilde{\mathbf{B}} = \begin{bmatrix} 0.0752 & 0.1377 & -0.2715 & 0.1123 \\ 0.1846 & -0.5557 & -0.3262 & 0.2119 \end{bmatrix}.$$

To observe the effect of precision reduction on these calculations, the element-wise absolute error can be calculated using $|\mathbf{B} - \tilde{\mathbf{B}}|$, such that

$$\mathbf{E} = \begin{bmatrix} 0.1117 & 0.3314 & 0.9400 & 0.2599 \\ 0.2385 & 0.2624 & 0.2886 & 0.3075 \end{bmatrix} * 10^{-3}.$$

The impact of precision reduction on the performance of the massive MIMO-OFDM systems using several detectors and with different precision formats are further studied in this chapter and the results are discussed in Section 5.6.

5.5 Complexity Analysis

An approximate calculation that depends on *gaxpy* algorithm [40] is introduced here to calculate the complexity required by each MIMO detector. According to this algorithm, the number of operations is a general expression used to identify any mathematical operation.

Referring back to the methods of MIMO detection illustrated in Section 5.3, the implementation of the ZFE detector used in this work has a complexity of $O(9N_r + 2N_r N_t(N_t - 4))$ operations, which is a reduced complexity approach to find the Moore-Penrose matrix inversion compared to the traditional ZFE implementation. The MIMO detector based on
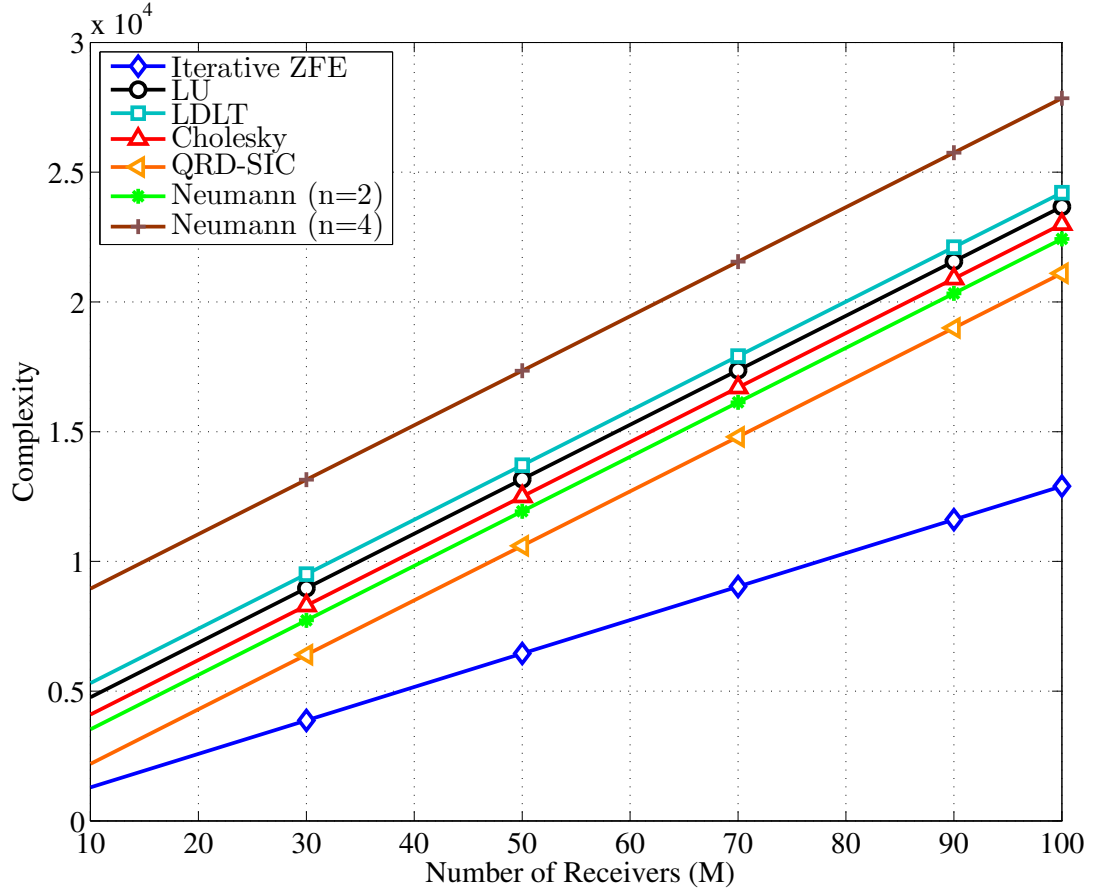
Figure 5.3: Complexity calculations required by each method.

the Gram matrix inverse were implemented using three different decomposition schemes to compare their individual performance.

Method	$N_r = 20$	$N_r = 50$	$N_r = 100$
Iterative ZFE	2580	6450	12900
Cholesky	6200	12500	23000
LDLT	7410	13710	24210
LU	6867	13167	23667
QRD-SIC	4300	10600	21100
Neumann, $n = 2$	5630	11930	22430
Neumann, $n = 4$	11050	17350	27850

Table 5.1: Table of operations required by each method at $N_t = 10$ transmitters and $N_r = 20$, 50 and 100 receivers.

Firstly, the Cholesky implementation requires in total $O(2N_t^2 N_r + 2N_t^3 + N_t N_r)$ operations to implement the MIMO detector including calculations of the triangular matrix inverse. The second is the LDLT-based MIMO detector requiring $O(N_t^2(2N_r + 2) +$

$N_t(N_r + 1) + 3N_t^3)$ operations to be implemented as it requires a diagonal matrix inverse in addition to the lower triangular inverse. The third Gram matrix-based MIMO detector is LU-factorization, which requires calculating the triangular inverse twice and takes $O(N_t^2(2N_r + 16N_t/6) + N_t N_r)$ operations. The QRD has been used as a successive interference cancellation procedure with backward substitution, and this requires $O(N_t^2(2N_r + 1) + N_t N_r)$ operations. Finally, matrix inversion with the Neumann series expansion needs $O(N_t(3+N_r)+2N_t^2(2+N_r)+N_t^3)$ operations, when $n = 2$ and requires $O(5N + 8N^2 + 6N^3 + 2N^2 N_r + N N_r)$ operations for $n = 4$. The numbers of operations required in the simulations are presented in Table. 5.1 and Fig. 5.3 with different receive antennas and at $N_t = 10$ transmitters.

5.6 Simulation and Results

The performance of the MIMO detectors will be affected by the level of error resulting from calculating the matrix inversion in the methods above with reduced precision. This will result in degradation in the BER with respect to the SNR as the precision decreases. It is worth noting that Neumann detector used in the simulation of this chapter refers to the detector used in [67] which is different than the ZFE detector used in the coded massive MIMO system of the previous chapters.

The simulations here assume $N_t = 4, 10$ transmitting and $N_r = 100, 200$ receiving antennas as shown in Figs. 5.4, 5.5, 5.6 and 5.7 for 4-QAM modulated system and in Figs. 5.8, 5.9, 5.10 and 5.11 for 16-QAM scheme to simulate the massive MIMO scenarios. Comparing the performance of these detectors at double and single precision will give similar performance since the error resulting from the calculations remains small. As the precision of the calculations decreases to half precision, the performance of the Neumann approximation will start to diverge and can not be considered in the detection at half precision. The performance of the LU detector will degrade enormously due to the large number of operations required by this detector. In comparison, the other detectors have no major effect on the performance at half precision detection, as illustrated in part (a) of the Figs. 5.8, 5.9, 5.10 and 5.11. Group-A detectors represent, Neumann (n=4,2)(64,11,52), Cholesky (64,11,52), Cholesky (16,5,10), QRD-SIC (64,11,52), QRD-SIC (16,5,10), ZFE (64,11,52), LDLT (64,11,52), LDLT (16,5,10) and LU (64,11,52), and they are exhibit similar performance.

To fulfill the requirements of hardware implementation, the calculations of each detector are made at below the standard IEEE 754 representation in order to minimize the required bit representation. In part (b) of Figs. 5.4 - 5.11 for both modulation types, the performance of the best detectors is presented utilizing user-defined representations with word length $w = 12$ and $w = 10$. Reducing the word length to $w = 12$ has negligible effect on the performance of the QRD-SIC and LDLT detectors, while it degraded the performance of the ZFE and the Cholesky detectors. Further reduction in the word length to $w = 10$ has resulted in a degradation to the performance of these two detectors.

According to this simulation, the QRD-SIC detectors exhibit the best performance compared to the other detectors, followed by the LDLT detector. By comparing part (b) of the Figs. 5.4 - 5.11, it is observed that the increase in the number of transmitting and receiving elements have negative effect on the performance of the best two detectors. In

Fig. 5.9, the effect of reducing the word length from $w = 12$ to $w = 10$ is trivial and can be ignored. However, as shown in Fig. 5.11a), the degradation was 2 dB for the QRD-SIC detectors and it was 3.5 dB for the LDLT detectors.

The ZFE detector exhibits good performance at half precision detection with reduced complexity. Employing this detector with the soft demodulation of the coded system as presented in Chapters 3 and 4 will result in a reduced complexity detection with improved performance.

Based on the results shown in Figs 5.4 - 5.11, the degradation in the BER performance for the different MIMO detectors at different modulation index and precision have suggested that the increase in the number of mathematical operations required by each detector can affect the accuracy of the calculations at reduced precision, which results in an accumulated errors that reduce the detection ability of that detector. As an example, the performance of the LU factorization based detector have enormously degraded at half precision detection as a result of the operations required by the LU factorization and the matrix inversion. It is worth noting that in the legend, the triplet (w, e, f) indicates the word length, exponent, and fraction, respectively.
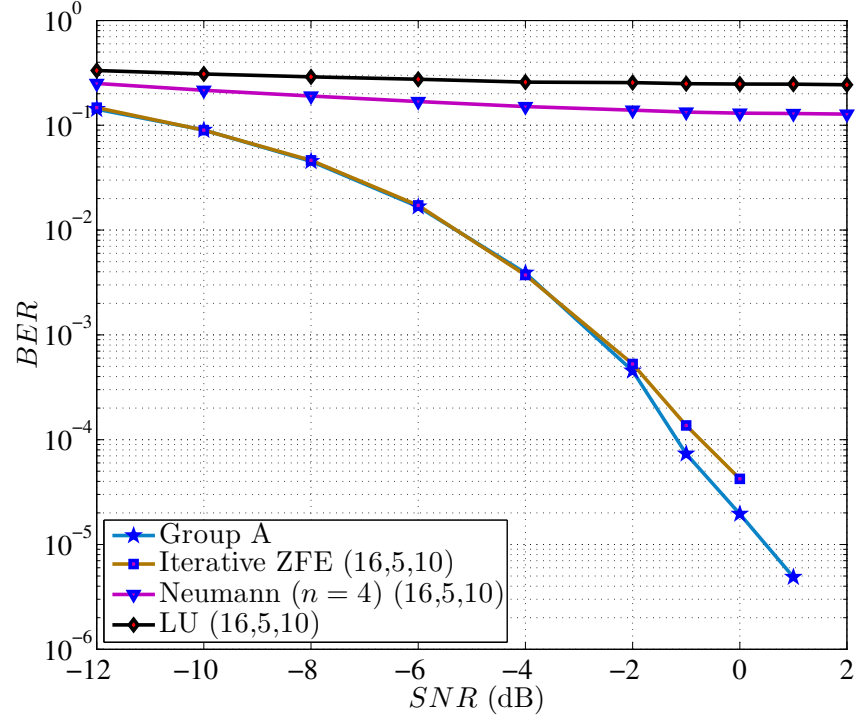
(a) Full and half precision

(b) At selected precision

Figure 5.4: Performance of massive MIMO-OFDM systems with $N_r = 100$, $N_t = 10$ and 4-QAM scheme at (a) Full and half precision. (b) Selected precision. Group-A refers to the following detectors, Neumann (n=4,2)(64,11,52), Cholesky (64,11,52), Cholesky (16,5,10), QRD-SIC (64,11,52), QRD-SIC (16,5,10), Iterative ZFE (64,11,52), LDLT (64,11,52), LDLT (16,5,10) and LU (64,11,52).
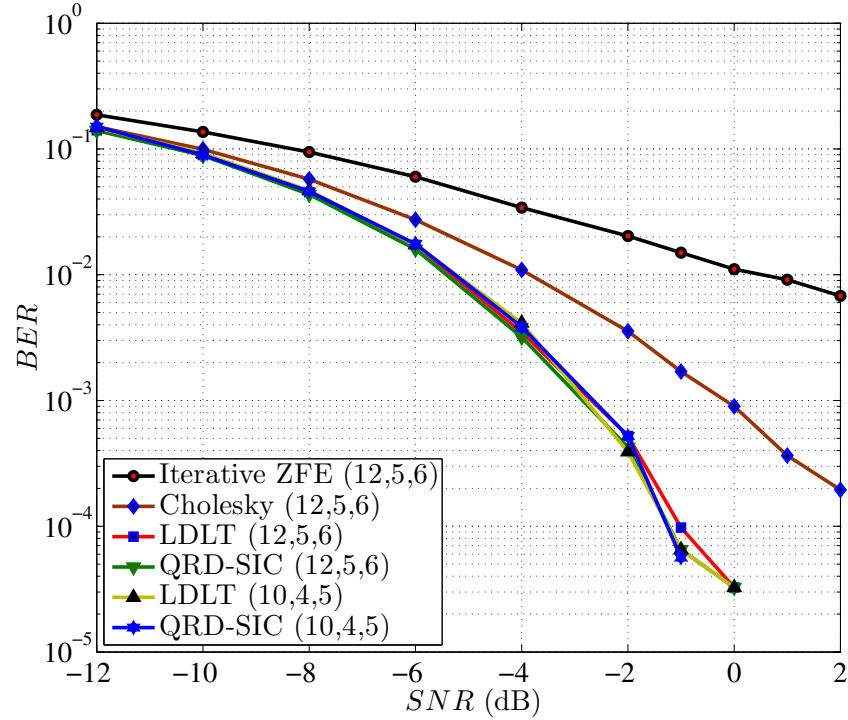
(a) Full and half precision

(b) At selected precision

Figure 5.5: Performance of massive MIMO-OFDM systems with $N_r = 100$, $N_t = 4$ and 4-QAM scheme at (a) Full and half precision. (b) Selected precision. Group-A refers to the following detectors, Neumann (n=4,2)(64,11,52), Cholesky (64,11,52), Cholesky (16,5,10), QRD-SIC (64,11,52), QRD-SIC (16,5,10), Iterative ZFE (64,11,52), LDLT (64,11,52), LDLT (16,5,10) and LU (64,11,52).

(a) Full and half precision

(b) At selected precision

Figure 5.6: Performance of massive MIMO-OFDM systems with $N_r = 200$, $N_t = 4$ and 4-QAM scheme at (a) Full and half precision. (b) Selected precision. Group-A refers to the following detectors, Neumann (n=4,2)(64,11,52), Cholesky (64,11,52), Cholesky (16,5,10), QRD-SIC (64,11,52), QRD-SIC (16,5,10), Iterative ZFE (64,11,52), LDLT (64,11,52), LDLT (16,5,10) and LU (64,11,52).
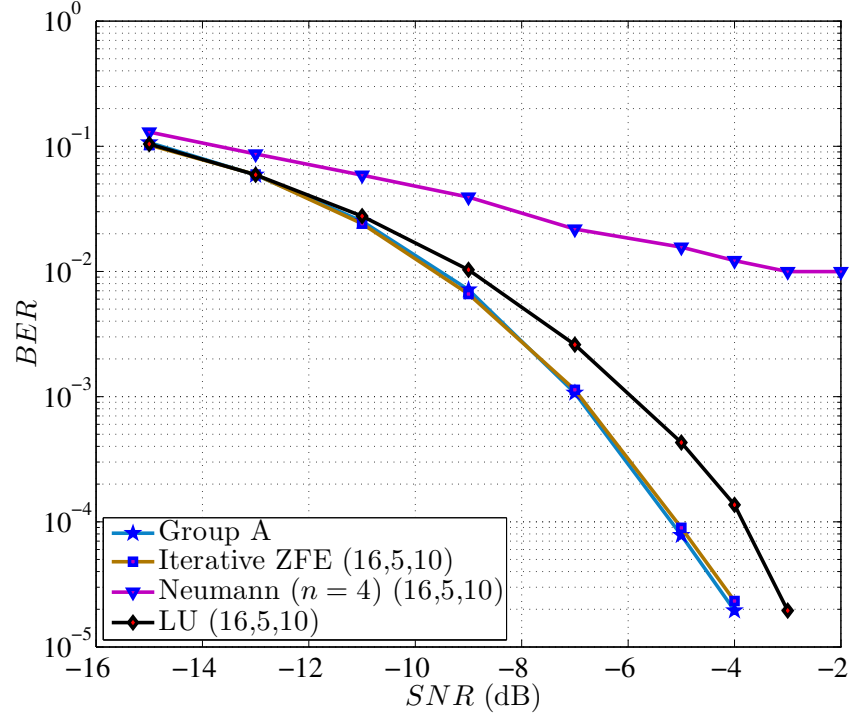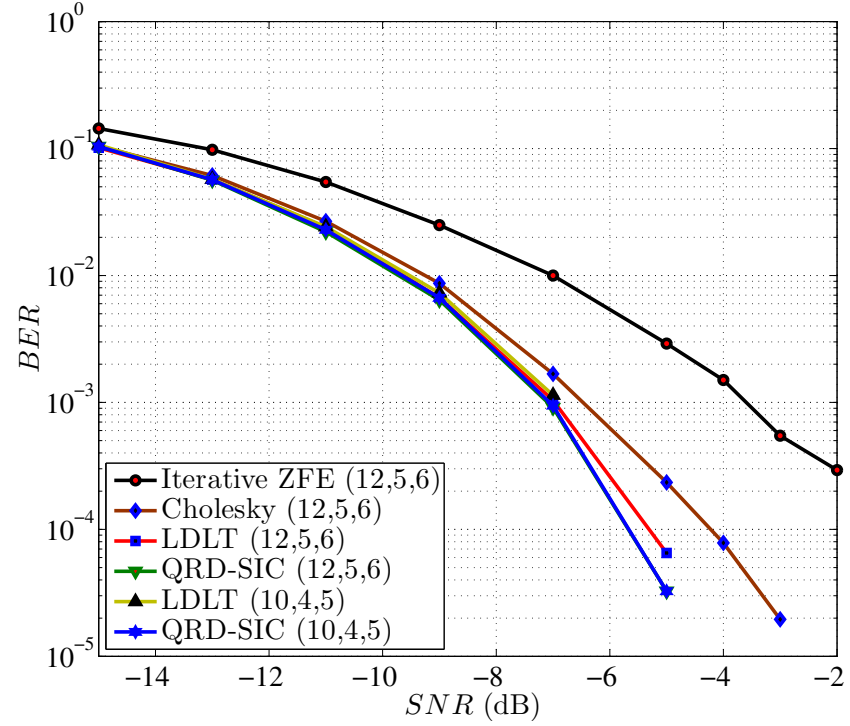
(a) Full and half precision

(b) At selected precision

Figure 5.7: Performance of massive MIMO-OFDM systems with $N_r = 200$, $N_t = 10$ and 4-QAM scheme at (a) Full and half precision. (b) Selected precision. Group-A refers to the following detectors, Neumann (n=4,2)(64,11,52), Cholesky (64,11,52), Cholesky (16,5,10), QRD-SIC (64,11,52), QRD-SIC (16,5,10), Iterative ZFE (64,11,52), LDLT (64,11,52), LDLT (16,5,10) and LU (64,11,52).
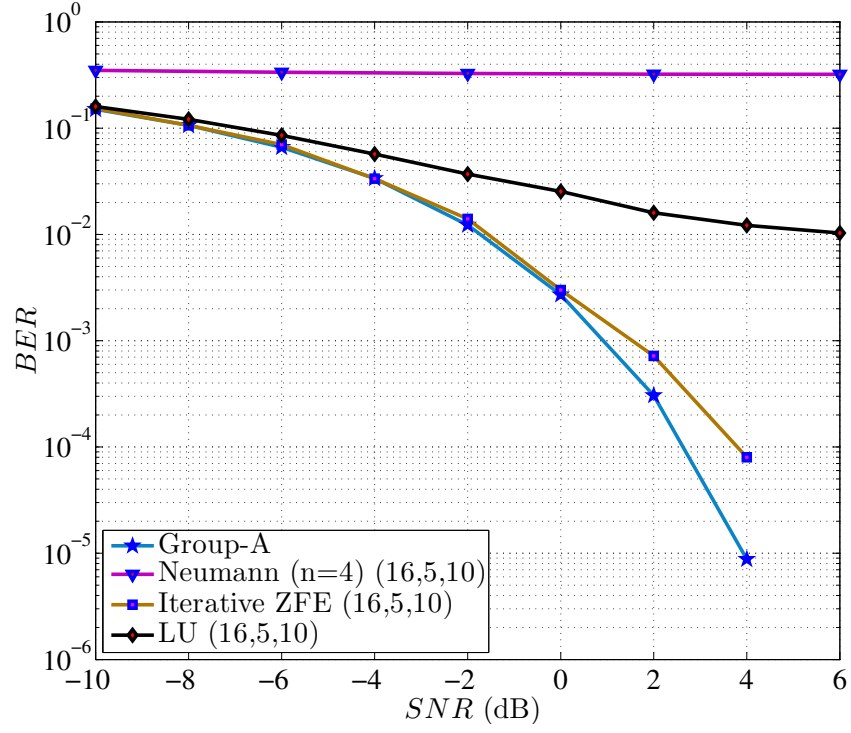
(a) Full and half precision
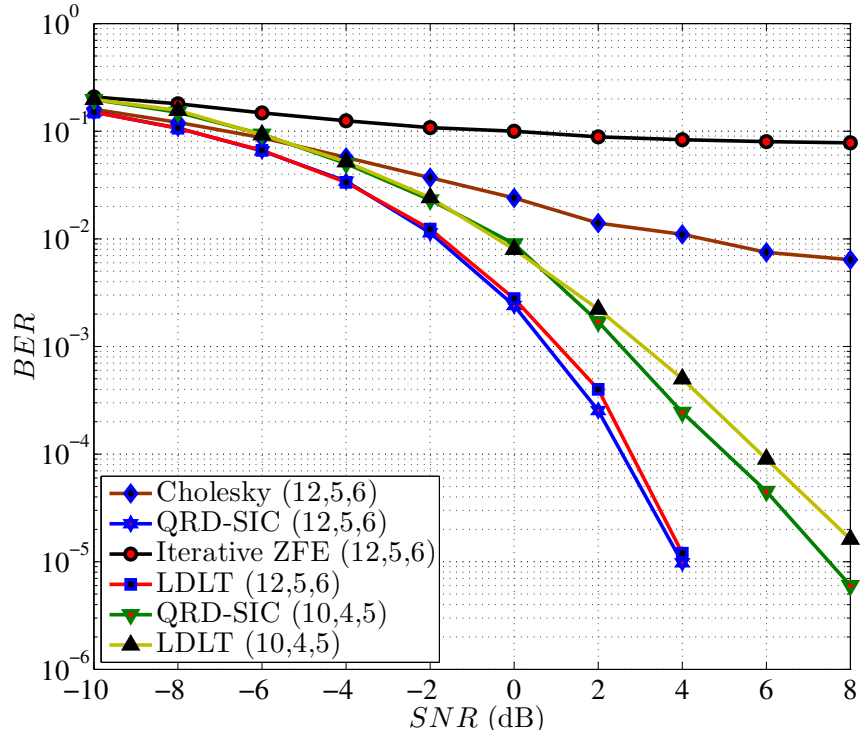
(b) At selected precision

Figure 5.8: Performance of massive MIMO-OFDM systems with $N_r = 100$, $N_t = 10$ and 16-QAM scheme at (a) Full and half precision. (b) Selected precision. Group-A refers to the following detectors, Neumann (n=4,2)(64,11,52), Cholesky (64,11,52), Cholesky (16,5,10), QRD-SIC (64,11,52), QRD-SIC (16,5,10), Iterative ZFE (64,11,52), LDLT (64,11,52), LDLT (16,5,10) and LU (64,11,52).
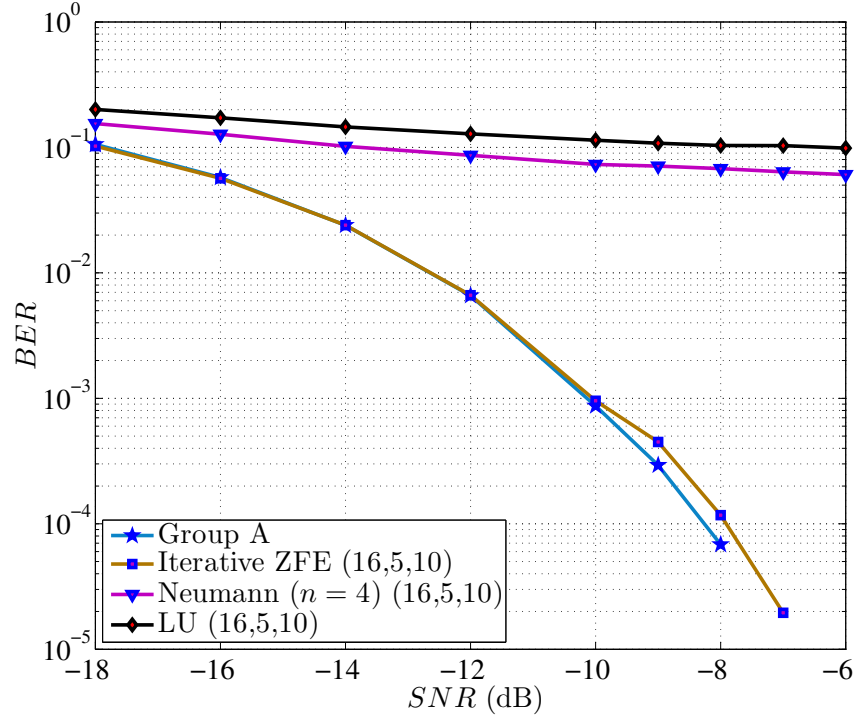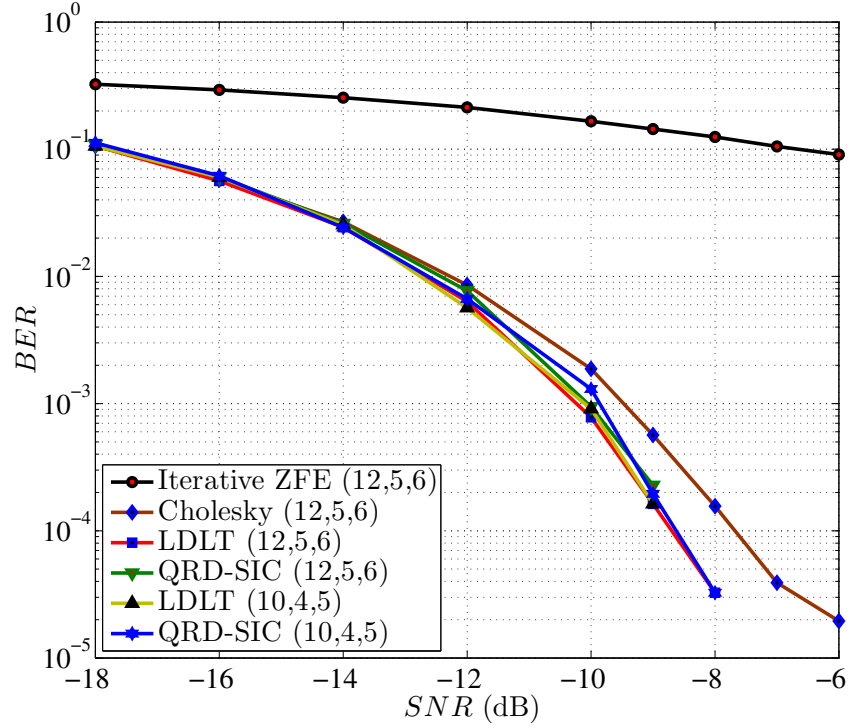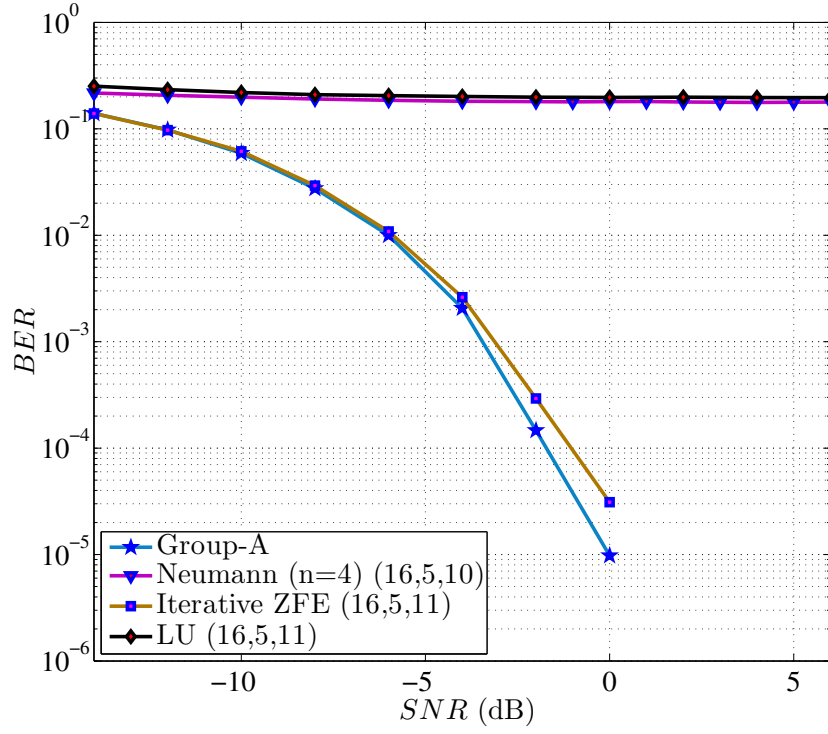
(a) Full and half precision
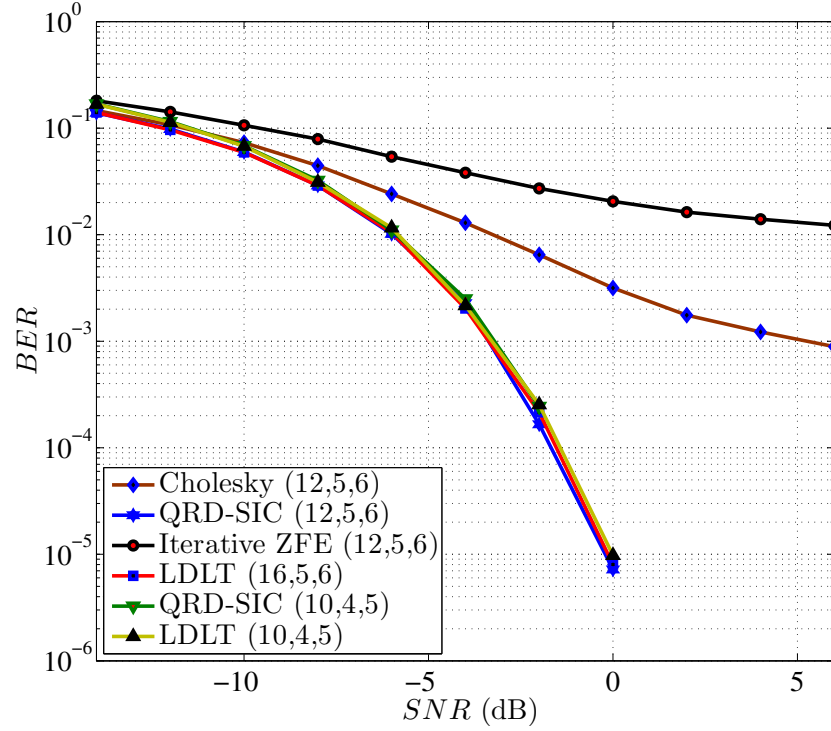
(b) At selected precision

Figure 5.9: Performance of massive MIMO-OFDM systems with $N_r = 100$, $N_t = 4$ and 16-QAM scheme at (a) Full and half precision. (b) Selected precision. Group-A refers to the following detectors, Neumann (n=4,2)(64,11,52), Cholesky (64,11,52), Cholesky (16,5,10), QRD-SIC (64,11,52), QRD-SIC (16,5,10), Iterative ZFE (64,11,52), LDLT (64,11,52), LDLT (16,5,10) and LU (64,11,52).
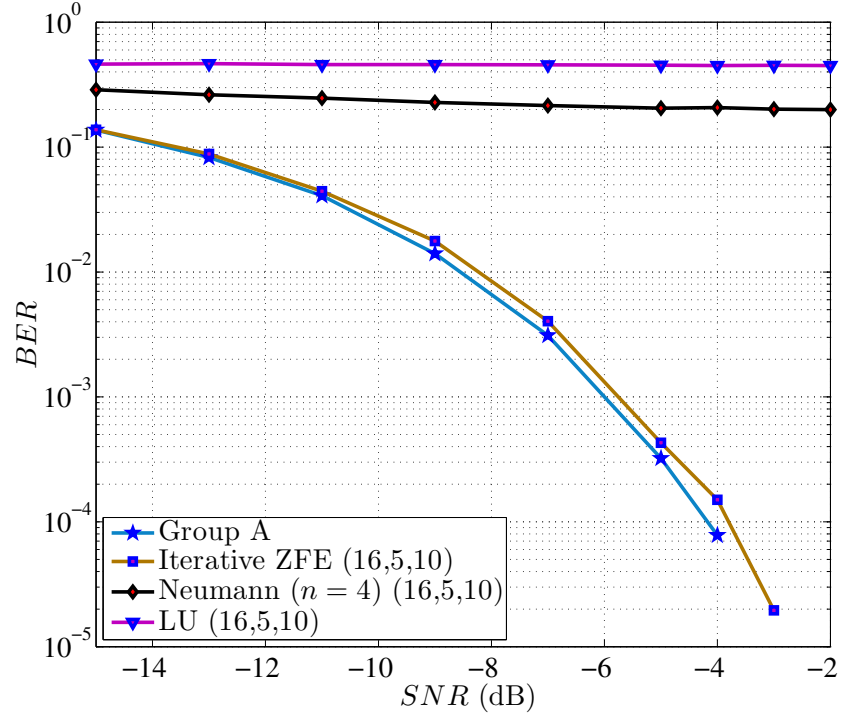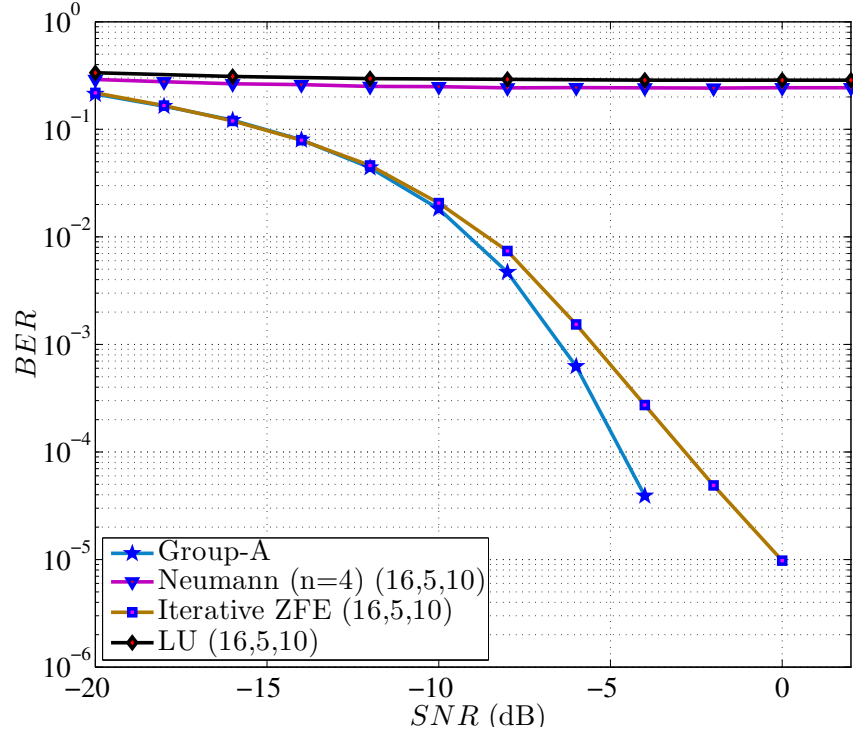
(a) Full and half precision
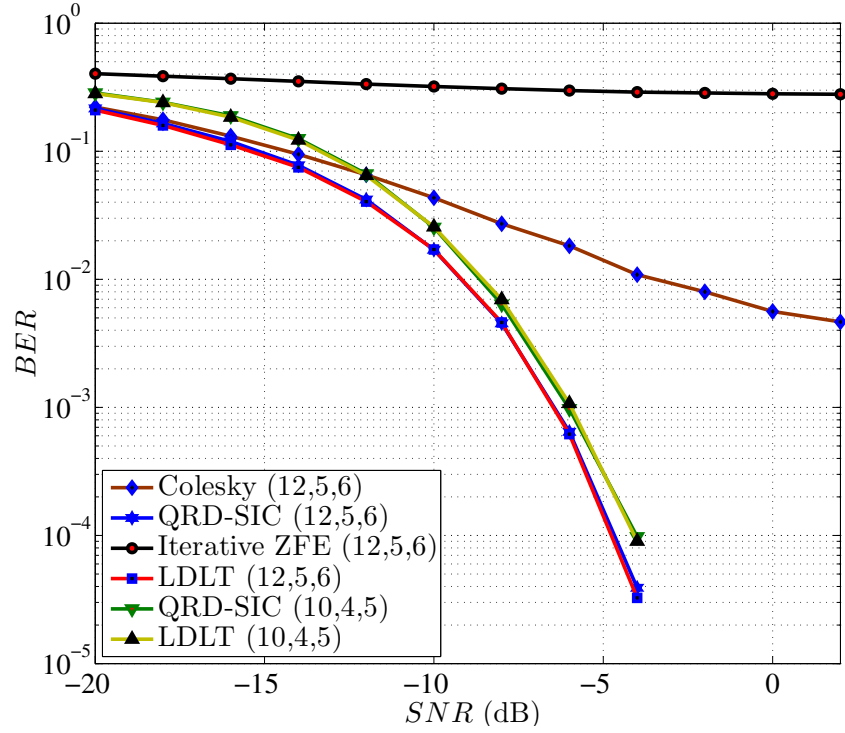
(b) At selected precision

Figure 5.10: Performance of massive MIMO-OFDM systems with $N_r = 200$, $N_t = 4$ and 16-QAM scheme at (a) Full and half precision. (b) Selected precision. Group-A refers to the following detectors, Neumann (n=4,2)(64,11,52), Cholesky (64,11,52), Cholesky (16,5,10), QRD-SIC (64,11,52), QRD-SIC (16,5,10), Iterative ZFE (64,11,52), LDLT (64,11,52), LDLT (16,5,10) and LU (64,11,52).
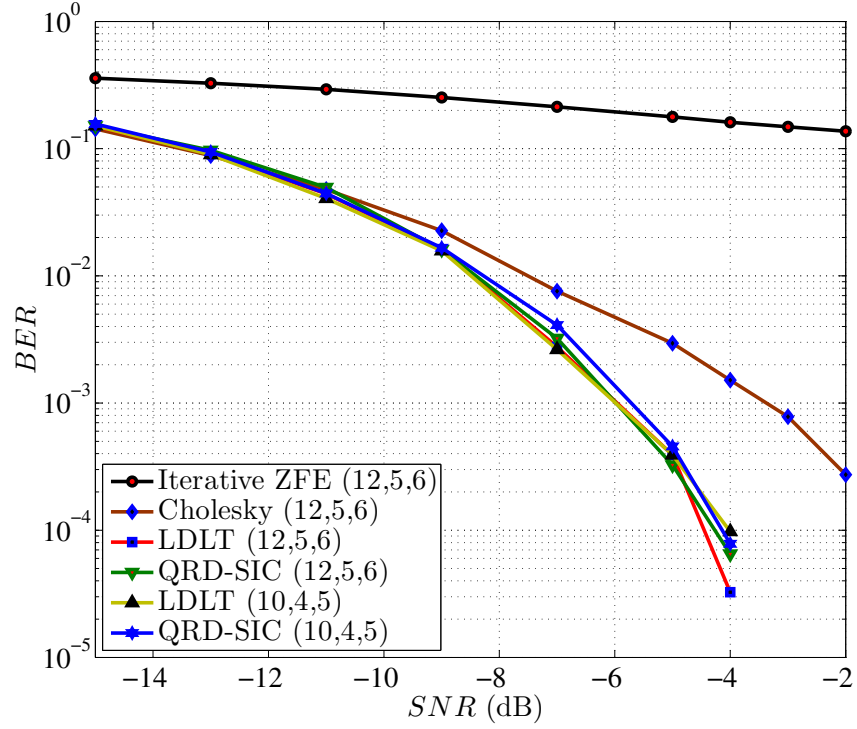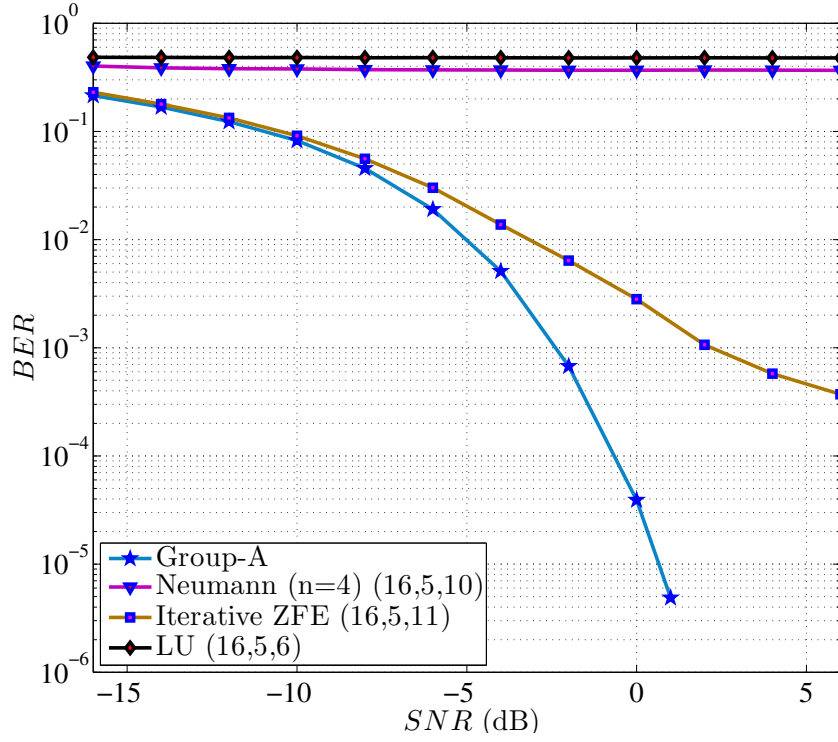
(a) Full and half precision
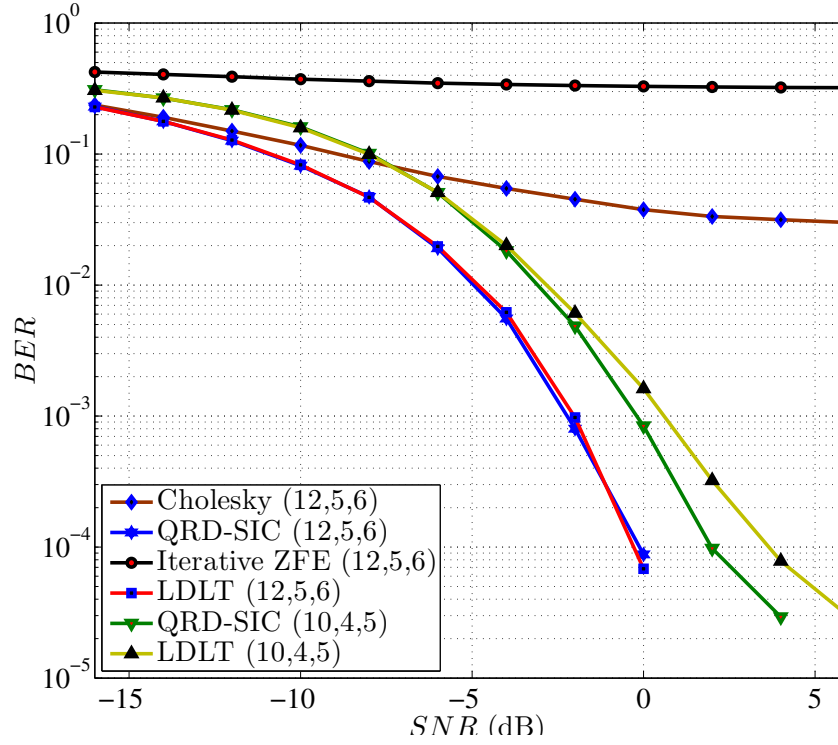
(b) At selected precision

Figure 5.11: Performance of massive MIMO-OFDM systems with $N_r = 200$, $N_t = 10$ and 16-QAM scheme at (a) Full and half precision. (b) Selected precision. Group-A refers to the following detectors, Neumann (n=4,2)(64,11,52), Cholesky (64,11,52), Cholesky (16,5,10), QRD-SIC (64,11,52), QRD-SIC (16,5,10), Iterative ZFE (64,11,52), LDLT (64,11,52), LDLT (16,5,10) and LU (64,11,52).

5.7   Chapter Summary

This chapter presented a comparison between different linear massive MIMO detectors implemented using matrix decomposition schemes. The simulation results have suggested that the performance of the ZFE, Cholesky, LDLT and QRD-SIC detectors have shown to have good performance at half precision detection compared to the other MIMO detectors. However, at reduced precision with word length less than 12 bits, the performance of QRD and LDLT detectors outperform that of the other schemes. In addition, the increase in the number of receive and transmitted antennas have negatively affected the performance of the detectors and cause a degradation to the BER performance of the QRD-SIC and the LDLT detectors. By comparing the complexity of implementation, it is observed that the ZFE detectors has the lowest complexity of implementation compared to the other detectors followed by the QRD-SIC, Numann, Cholesky, LU and LDLT detectors.

Chapter 6

Conclusion and Future Work

Massive MIMO communication systems are the key technology for the next generation wireless communication systems. The main features of these systems are the high data throughput and the improved transmission reliability compared to the conventional communication systems. However, several challenges have emerged as a result of the high number of antennas at the base station such as the receiver complexity, channel estimation, pilot contamination, hardware impairment, and many other challenges.

The motivation behind this research was to investigate the performance of the spatially multiplexed massive MIMO-OFDM systems in the uplink mode of transmission and to design a reduced complexity detector for the coded system with improved performance. The contribution of this thesis can be divided into three parts; (a) deriving the noise distribution after the ZFE and designing the receiver for the massive MIM-OFDM systems based on that PDF, (b) analyzing the performance for the coded and the uncoded massive MIMO-OFDM systems, (c) comparing the performance of various massive MIMO detectors based on the fixed point arithmetic to examine their effectiveness for the hardware implementation below the standard IEEE 754 half precision representation.

As the literature review suggested, the search for a reduced complexity receiver for the massive MIMO systems is essential especially when the number of receive antennas at the BS is very high. Accordingly, the PDF for the random variable of the noise after the ZFE has been derived based on the ratio distribution utilizing Neumann matrix inversion. This PDF is subsequently used to calculate the LLRs of the received signals to be used in the decoding of the LDPC and turbo decoders. To verify the accuracy of the newly derived PDF, the experimentally obtained histogram plots from Monte-Carlo simulations have shown a close match to the theoretically derived PDF. In addition, different statistical

tests, such as the KS test of independence and Chi-square test, have been applied on the derived PDF to verify the accuracy of this assumption. The BER performance of the simulation for the LDPC and turbo coded massive MIMO-OFDM systems has been investigated for the derived LLRs and compared to the Gaussian based LLRs. As a result, the BER performance in the simulations has improved by 2 dB at 10^{-4} for the LDPC coded system, and 0.8 dB for the turbo coded system, compared to Gaussian distribution using the ZFE. Consequently, the required number of receive antennas has reduced by 75 elements at an SNR of -16.3 dB for the system having $N_r = 500$ and $N_t = 4$, which implies that a reduction in the required physical space and to the cost of the hardware equipment required for the implementation.

Further analysis revealed that this new PDF has increased the computational complexity of LLR calculations, thus, increasing the overall receiver complexity. To reduce this complexity and to maintain good performance, an equivalent LLR equation has been suggested with a low complexity design using Newton polynomial interpolation. The performance of this approximated LLR equation demonstrated a close match to the exact LLR with negligible complexity. However, the approximated LLRs for the LDPC coded system required 3rd order polynomial to perform close to the exact BER simulations, while the LLRs for the turbo coded systems required 1st order polynomial for the BPSK/4-QAM modulated systems.

The selection of the system parameters is affected by different factors such as the OFDM block length, the interleaver block length, and the CP length. These parameters have been addressed as shown in Figs. 3.12 and 3.13, and based on that, the lengths of the OFDM and the interleaver were selected as 1024 to achieve good performance with reduced complexity. The complexity and the performance of the coded system can be greatly affected by the length of the interlever. In practice, the higher the interleaver length is the higher the required complexity for better performance and vise-versa. The effect of CP length on the performance of the coded and uncoded system has also been investigated as shown in Fig. 3.13 and hence, the CP was selected as 128 to completely remove the effect of the ISI and IBI.

The second part of the contribution of this thesis was to analyze the performance of the coded and the uncoded massive MIMO-OFDM systems. The BER performance for massive MIMO-OFDM systems was derived using the approximate effective noise PDF after the ZFE. The derived BER has been verified using the Monte-Carlo simulations of different transmit and receive antenna combinations and the results have shown a close

match between the theoretical and empirical plots.

In addition, the effective noise PDF after the ZFE has been utilized to derive the PDF of the SNR. Then this PDF is used to derive the outage probability and the channel capacity for the investigated massive MIMO-OFDM system. In addition, an upper and two lower bounds were derived for the channel capacity based on different assumptions and their performance was compared to the exact capacity. The simulation results verified the accuracy of the derived equations, and the bounds have successfully approached the exact capacity within the selected range.

The derived PEP in Section 4.3.1 was used to obtain an upper-bound for convolutionally encoded massive MIMO-OFDM systems. The results have bounded the performance for different error weight values and indices, and the upper-bound performance became very tight for the two selected codes. In addition, the turbo coded system was bounded within 0.15 dB of the Monte-Carlo simulations by using the derived PEP and the D_m terms given for the $(5, 7)_8$ PCCC using BPSK/4-QAM modulation.

The third part of the contribution of this thesis was to investigate the hardware implications of the massive MIMO receivers, which can be regarded as one of the massive MIMO system challenges as been suggested by the literature. A comparison of different linear massive MIMO detectors was implemented using matrix decomposition schemes. The simulation results have suggested that at the reduced precision with word length less than 12 bits, the performance of QRD and LDLT decomposition outperform those of other schemes such as Cholesky, LU, and ZFE techniques. Finally, matrix inversion using the Neumann expansion has a limited application in fixed point expression since it shows reduced performance at IEEE 754 half precision and below.

Future Work

The main focus of this thesis was on the single user, point-to-point uplink transmission of massive MIMO-OFDM communication systems. However, different massive MIMO system configurations can be considered in the future work, some of these suggested topics include,

- One of the main challenges to the massive MIMO-OFDM communication systems is the interference between the pilots of different receivers or cells that affect the channel estimation which is known as pilot contamination. Different techniques

have been used to eliminate this issue, however, this direction requires more analysis to completely remove the effect of the pilots interference especially when the number of antennas is in thousands.

- Most of the researches on the massive MIMO systems assume uncorrelated Rayleigh fading channels as a propagation medium. However, this assumption can be misleading in practical systems especially for very large number of antennas. The correlation can significantly affect the performance of the massive MIMO communication systems and contribute to the degradation of the BER. Therefore, for more accurate analysis and design, it is recommended to take the effect of the correlation between the fading channels into consideration rather than the i.i.d assumption.

- Precoding techniques and the transceiver design can be considered to reduce the complexity of the detection at the receiver and to improve the system performance. Several precoding techniques have been used with the massive MIMO systems, which utilize the channel information, while other precoders have been optimized based on the SINR or the signal to leakage noise ratio (SLNR).

- Hardware implementation is a very important topic towards the adoption of the massive MIMO communication systems. This issue has been addressed in several publications but mostly in the view of the signal processing with limited actual implementation due to the high cost. Therefore, further analysis is desired to tackle the challenges of hardware implementation in reality.

- Millimeter waves (MMW) is a 5G technology that improves the spectral efficiency and the capacity. This technology utilizes the unoccupied frequency bands above 30 GHz. The adaptation of the MMW technology to the massive MIMO systems can improve the performance of both systems and results in a reduction in the size of the antenna array and subsequently, the cost of implementation.

- One of the trends to reduce the complexity of the receiver and to reduce the power consumption for the massive MIMO systems is to select a subset of the receive antennas instead of using the whole set in the detection. The selection of the optimal subset requires solving an optimization problem that depends on the specific selection criteria.

Appendix A

Tables of weight spectra and minimum asymptotic rate of growth.

Table A.1: Weight spectra and minimum asymptotic rate of growth of the weights in the incorrect subset for the best rate (1/2) convolutional codes up to constraint length 14 [96].

m	generators (octal)	df	$(a_{df+l}), l = 0, 1, \ldots 17$ $[c_{df+l}], l = 0, 1, \ldots 17$	d_0
2	$(5, 7)_8$	5	(1,2,4,8,16,32,64,128,256,512,1024,2048,4096,8192,16384,32768,65536,131072) [1,4,12,32,80,192,448,1024,2304,5120,11264,24576,53248,114688,245760,524288,1114112,2359296]	1/2
3	$(15, 17)_8$	6	(1,3,5,11,25,55,121,267,589,1299,2865,6319,13937,30739,67797,149531,329801,727399) [2,7,18,49,130,333,836,2069,5060,12255,29444,70267,166726,393635,925334,2166925,5057286,11767305]	1/2
4	$(23, 35)_8$	7	(2,3,4,16,37,68,176,432,925,2156,5153, 11696,26868,62885, 145085,334024,774966,1793363) [4,12,20,72,225,500,1324,3680,8967,22270,57403,142234,348830,887106,2134239,5205290,12724352,31022962]	4/11
5	$(53, 75)_8$	8	(1, 8,7,12,48,95,281,605,1272,3334,7615,18131,43197,99210,237248,559238,1312675,3108350) [2,36,32,62,332,701,2342,5503,12506,36234,88576,225685,574994,1400192,3554210, 8845154,21841106,54350946]	8/23
6	$(133, 171)_8$	10	(11,0,38,0,193.0,1331,0,7275,0,40406,0,234969,0,1337714,0,7594819,0) [36,0,211,0,1404,0,11633,0,77433,0,502690,0,3322763,0,21292910,0,134365911,0]	4/18
7	$(247, 371)_8$	10	(1,6,12,26,52,132,317,730,1823,4446,10739,25358,60773,146396,350399,842174,2021290,4853474) [2,22,60,148,340,1008,2642,6748,18312,48478, 126364,320062,821350, 2102864,5335734,13549068,34254388,86441848]	5/16
8	$(561, 753)_8$	12	(11,0,50,0,286,0,1630, 0,9639,0,55152,0,320782,0,1859184,0,10777264 ,0) [33,0,281,0,2179,0,15035,0,105166,0,692330,0,4580007,0,29692894,0,190453145,0]	8/27
9	$(1167, 1545)_8$	12	(2,8,15,35,68,170,458,1084,2574,6177,14939,36200,86856,208847,504561,1217706,2933502,7066863) [14,26,74,257,496,1378,4122,10832,27988,72209,186920,483102,1234736,3149395,8033048,20419644,51688436,130527021]	1/4
10	$(2335, 3661)_8$	14	(21,0,74,0,454,0,2687,0,15629,0,90518,0,526556,0,3067758,0,17845415,0) [94,0,463,0,3783,0,26711,0,181571,0, 1207474,0,7919894,0,51390913,0,329342619,0]	2/15
11	$(4335, 5723)_8$	15	(16,31,44,129,309,697,1713,4175,10158,24508,58600,141960,343347,826478,1996843,4820534,11619637, 28039590) [76,180,374,1142,2783,6836,18709,49242,128178,329408,836478,2151230,5497355,13931276,35357451,89485786,225656685,568414202]	14/53
12	$(10533, 17661)_8$	16	(33,0,111,0,779,0,4128,0,24173,0,142500,0,828402,0,4829478,0,28122349,0) [152,0,971,0,6933,0,45436,0,303435,0,2036131,0,13256560,0,85514159,0,546034284,0]	8/33
13	$(21675, 27123)_8$	16	(4,17,35,76,193,454, 1047,2624,6138,14944,36179,86640, 210568,508233, 1225765, 2960696,7146740, 17245991) [22,99,218,608,1724,4404,11108,30438,75942,196714,507232,1289364,3311290,8425785,21377872,54168142, 136847122,344912207]	27/103

Table A.2: Weight spectra and minimum asymptotic rate of growth of the weights in the incorrect subset for the best rate (1/3) convolutional codes up to constraint length 14 [96].

m	generators (octal)	df	(a_{df+l}), $l = 0, 1, \ldots 17$ $[c_{df+l}]$, $l = 0, 1, \ldots 17$	d_0
2	$(5, 7, 7)_8$	8	(2,0,5,0,13,0,34,0,69,0,233,0,610,0,1597,0,4181,0) [3,0,15,0,58,0,201,0,655,0,2052,0,6255,0,18687,0,54974,0]	2/3
3	$(13, 15, 17)_8$	10	(3,0,2,0,15,0,24,0,87,0,188,0,557,0,1354,0,3713,0) [6,0,6,0,58,0,118,0,507,0,1284,0,4323,0,11846,0,36009,0]	4/5
4	$(25, 33, 37)_8$	12	(5,0,3,0,13,0,62,0,108,0,328,0,1051,0,2544,0,7197,0) [12,0,12,0,56,0,320,0,693,0,2324,0,8380,0,23009,0,71016,0]	2/3
5	$(47, 53, 75)_8$	13	(1,3,6,4,5,12,14,33,66,106,179,317,513,766,1297,2251,3964,6721) [1,8,26,20,19,62,86,204,420,710,1345,2606,4343,6790,12305,22356,41090,72820]	8/13
6	$(133, 145, 175)_8$	15	(3,5,5,6,11,15,25,54,92,164,274,450,758,1290,2142,3567,6089,10403) [11,16,19,28,55,96,169,338,636,1276,2172,3628,6580,12048,20820,36358,65009,115368]	2/3
7	$(225, 331, 367)_8$	16	(1,0,8,0,24,0,51,0,133,0,405,0,1129,0,3532,0,9754,0) [1,0,24,0,113,0,287,0,898,0,3020,0,9436,0,32644,0,98472,0]	24/37
8	$(557, 663, 711)_8$	18	(5,0,7,0,36,0,85,0,204,0,636,0,1927,0,5416,0,15769,0) [11,0,32,0,195,0,564,0,1473,0,5129,0,17434,0,54092,0,171117,0]	10/17
9	$(1117, 1365, 1633)_8$	20	(8,0,18,0,41,0,132,0,395,0,981,0,2991,0,8843,0,25590,0) [29,0,91,0,246,0,954,0,3138,0,8775,0,29185,0,94164,0,295578,0]	5/9
10	$(2353, 2671, 3175)_8$	22	(14,0,18,0,59,0,160,0,463,0,1458,0,3971,0,11578,0,34023,0) [53,0,92,0,347,0,1104,0,3644,0,12692,0,38407,0,122297,0,389889,0]	14/29
11	$(4767, 5723, 6265)_8$	24	(21,0,9,0,103,0,202,0,615,0,1811,0,5234,0,15358,0,43782,0) [80,0,58,0,607,0,1563,0,5008,16474,0,52106,0,166791,0,515426,0]	22/39
12	$(10533, 10675, 17661)_8$	24	(10,0,14,0,46,0,121,0,372,0,1055,0,6129,0,8848,0,26336,0) [27,0,74,0,228,0,794,0,2757,0,8531,0,28250,0,88579,0,286193,0]	20/37
13	$(21645, 35661, 37133)_8$	26	(12,0,32,0,54,0,167,0,506,0,1552,0,4404,0,12456,0,36522,0) [41,0,165,0,319,0,1156,0,3937,0,13208,0,42284,0,129918,0,413986,0]	4/7

Table A.3: Weight spectra and minimum asymptotic rate of growth of the weights in the incorrect subset for the best rate (1/4) convolutional codes up to constraint length 14 [96].

m	generators (octal)	df	$(a_{df+l}), l = 0, 1, \ldots 17$ $[c_{df+l}], l = 0, 1, \ldots 17$	d_0
2	$(5, 7, 7, 7)_8$	10	(1,1,1,3,2,5,7,8,16,19,30,46,61,98,137,201,303,429) [2,1,4,9,8,25,32,52,100,131,240,366,554,930,1368,2187,3398,5141]	2/3
3	$(13, 15, 15, 17)_8$	13	(2,1,0,3,1,4,8,4,15,16,18,45,40,73,119,122,244,313) [4,2,0,10,3,16,34,18,77,84,106,280,256,514,865,934,1988,2620]	1
4	$(25, 27, 33, 37)_8$	16	(4,0,2,0,4,0,15,0,30,0,54,0,115,0,252,0,511,0) [8,0,7,0,17,0,60,0,140,0,301,0,707,0,1675,0,3739,0]	6/5
5	$(53, 67, 71, 75)_8$	18	(3,0,5,0,6,0,12,0,23,0,67,0,157,0,283,0,610,0) [6,0,17,0,24,0,60,0,118,0,367,0,991,0,1980,0,4716,0]	10/9
6	$(135, 135, 147, 163)_8$	20	(10,0,0,0,19,0,0,0,117,0,0,0,711,0,0,0,3084,0) [37,0,0,0,94,0,0,0,768,0,0,0,5558,0,0,0,28349,0]	4/5
7	$(235, 275, 313, 357)_8$	22	(1,4,3,2,3,3,11,14,13,24,39,60,72,100,168,254,414,535) [2,10,10,8,10,11,54,64,68,140,218,382,478,660,1174,1846,3100,4139]	1
8	$(363, 535, 733, 745)_8$	24	(2,0,6,0,10,0,18,0,37,0,95,0,179,0,358,0,810,0) [4,0,22,0,38,0,103,0,237,0,587,0,1251,0,2765,0,6666,0]	16/17
9	$(1117, 1365, 1633, 1653)_8$	27	(4,4,4,8,5,14,22,17,33,46,75,112,168,248,317,501,703,1022) [12,12,18,44,31,72,120,108,221,320,545,786,1284,2054,2587,4272,6407,9376]	1
10	$(2327, 2353, 2671, 3175)_8$	29	(5,6,4,6,7,7,10,22,33,46,85,118,162,243,341,487,690,1053) [13,24,18,22,35,34,56,108,187,292,531,784,1158,1828,2631,3896,5792,9048]	49/51
11	$(4767, 5723, 6265, 7455)_8$	32	(14,0,10,0,14,0,47,0,105,0,180,0,452,0,973,0,1988,0) [49,0,40,0,82,0,267,0,640,0,1247,0,3362,0,8000,0,17453,0]	26/27
12	$(11145, 12477, 15573, 16727)_8$	33	(5,5,3,9,7,8,22,23,28,53,79,116,165,224,346,537,809,1112) [19,16,15,46,29,48,124,140,174,336,555,830,1219,1764,2826,4626,7123,10022]	6/7
13	$(21113, 23175, 35527, 35537)_8$	36	(19,0,16,0,30,0,83,0,153,0,333,0,736,0,1614,0,3298,0) [74,0,80,0,177,0,493,0,1098,0,2519,0,5872,0,13878,0,30678,0]	22/25

References

[1] E. Biglieri, R. Calderbank, A. Constantinides, A. Goldsmith, A. Paulraj, and H. V. Poor, *MIMO wireless communications*. Cambridge university press, 2007.

[2] S. Younis, A. Al-Dweik, C. C. Tsimenidis, B. S. Sharif, and A. Hazmi, "Robust early-late gate system for symbol timing recovery in MIMO-OFDM systems," in *Proc. IEEE 7th Int. Conf. Wireless Mobile Comput. Netw. commun. (WiMob)*, 2011.

[3] A. F. Molisch, *Wireless Communications*, 2nd ed. John Wiley & Sons, 2011.

[4] L. Dai, Z. Wang, and Z. Yang, "Spectrally efficient time-frequency training OFDM for mobile large-scale MIMO systems," *IEEE J. Sel. Areas Commun.*, vol. 31, no. 2, pp. 251–263, 2013.

[5] L. Bai and J. Choi, *Low complexity MIMO detection*. Springer Science & Business Media, 2012.

[6] Y. S. Cho, J. Kim, W. Y. Yang, and C. G. Kang, *MIMO-OFDM wireless communications with MATLAB*. John Wiley & Sons, 2010.

[7] L. Lu, G. Li, A. Swindlehurst, A. Ashikhmin, and R. Zhang, "An Overview of Massive MIMO: Benefits and Challenges," *IEEE J. Sel. Topics Signal Process.*, vol. 8, no. 5, pp. 742–758, 2014.

[8] A. Younis, S. Sinanovic, M. D. Renzo, R. Mesleh, and H. Haas, "Generalised sphere decoding for spatial modulation," *IEEE Trans. Commun.*, vol. 61, no. 7, pp. 2805–2815, 2013.

[9] N. Srinidhi, T. Datta, A. Chockalingam, and B. S. Rajan, "Layered Tabu search algorithm for large-MIMO detection and a lower bound on ML performance," *IEEE Trans. Commun.*, vol. 59, no. 11, pp. 2955–2963, 2011.

[10] P. Li and R. D. Murch, "Multiple output selection-LAS algorithm in large MIMO systems," *IEEE Commun. Lett.*, vol. 14, no. 5, pp. 399–401, 2010.

[11] P. va, F. Meyer, E. Riegler, and F. Hlawatsch, "Soft-heuristic detectors for large MIMO systems," *IEEE Trans. Signal Process.*, vol. 61, no. 18, pp. 4573–4586, 2013.

[12] Q. Zhou and X. Ma, "Element-based lattice reduction algorithms for large MIMO detection," *IEEE J. Sel. Areas Commun.*, vol. 31, no. 2, pp. 274–286, 2013.

[13] O. H. Toma and M. El-Hajjar, "Element-based Lattice Reduction aided K-Best detector for large-scale MIMO systems," in *Proc. IEEE 17th International Workshop on Signal Process. Adv. Wireless Commun. (SPAWC)*, 2016.

[14] J. Tong, P. J. Schreier, and S. R. Weller, "Design and analysis of large MIMO systems with Krylov subspace receivers," *IEEE Trans. Signal Process.*, vol. 60, no. 5, pp. 2482–2493, 2012.

[15] X. Gao, L. Dai, Y. Ma, and Z. Wang, "Low-complexity near-optimal signal detection for uplink large-scale MIMO systems," *Elect. Lett.*, vol. 50, no. 18, pp. 1326–1328, 2014.

[16] A. Kumar, S. Chandrasekaran, A. Chockalingam, and B. S. Rajan, "Near-optimal large-MIMO detection using randomized MCMC and randomized search algorithms," in *Proc. IEEE Int. Conf. Commun. (ICC)*, 2011.

[17] M. Wu, B. Yin, A. Vosoughi, C. Studer, J. R. Cavallaro, and C. Dick, "Approximate matrix inversion for high-throughput data detection in the large-scale MIMO uplink," in *Proc. IEEE Int. Sympo. Circuits Syst. (ISCAS2013)*, 2013.

[18] B. Yin, M. Wu, C. Studer, J. R. Cavallaro, and C. Dick, "Implementation trade-offs for linear detection in large-scale MIMO systems," in *Proc. IEEE Int. Conf. Acoust., Speech, Signal Process.*, 2013.

[19] M. Wu, B. Yin, G. Wang, C. Dick, J. R. Cavallaro, and C. Studer, "Large-scale MIMO detection for 3GPP LTE: algorithms and FPGA implementations," *IEEE J. Sel. Topics Signal Process.*, vol. 8, no. 5, pp. 916–929, 2014.

[20] U. Gustavsson, C. Sanchz-Perez, T. Eriksson, F. Athley, G. Durisi, P. Landin, K. Hausmair, C. Fager, and L. Svensson, "On the impact of hardware impairments on massive MIMO," in *Proc. IEEE Globecom Workshops*, 2014.

[21] X. Xia, D. Zhang, K. Xu, W. Ma, and Y. Xu, "Hardware impairments aware transceiver for full-duplex massive MIMO relaying," *IEEE Trans. Signal Process.*, vol. 63, no. 24, pp. 6565–6580, 2015.

[22] F. Athley, G. Durisi, and U. Gustavsson, "Analysis of Massive MIMO with hardware impairments and different channel models," in *Proc. 9th European Conf. Antennas Propag. (EuCAP)*, 2015.

[23] E. Bjrnson, M. Matthaiou, A. Pitarokoilis, and E. G. Larsson, "Distributed massive MIMO in cellular networks: Impact of imperfect hardware and number of oscillators," in *Proc. 23rd European Signal Process. Conf. (EUSIPCO)*, 2015.

[24] D. L. Colon, F. H. Gregorio, and J. Cousseau, "Linear precoding in multi-user massive MIMO systems with imperfect channel state information," in *Proc. XVI Workshop Info. Process. Control (RPIC)*, 2015.

[25] S. Zarei, W. Gerstacker, and R. Schober, "Uplink/downlink duality in massive MIMO systems with hardware impairments," in *Proc. IEEE Int. Conf. Commun. (ICC)*, 2016.

[26] B. Liu, Y. Cheng, and X. Yuan, "Pilot contamination elimination precoding in multi-cell massive MIMO systems," in *Proc. IEEE 26th Annual Int. Sympo. Personal Indoor Mobile Radio Commun. (PIMRC)*, 2015.

[27] L. S. Muppirisetty, H. Wymeersch, J. Karout, and G. Fodor, "Location-aided pilot contamination elimination for massive MIMO systems," in *Proc. IEEE Global Commun. Conf. (GLOBECOM)*, 2015.

[28] A. Zaib, M. Masood, A. Ali, W. Xu, and T. Y. Al-Naffouri, "Distributed channel estimation and pilot contamination analysis for massive MIMO-OFDM systems," *IEEE Trans. Commun.*, vol. 64, no. 11, pp. 4607–4621, 2016.

[29] A. H. Alqahtani, A. I. Sulyman, and A. Alsanie, "Rateless space-time block code for mitigating pilot contamination effects in multi-cell massive MIMO system with lossy links," *IET Commun.*, vol. 10, no. 16, pp. 2252–2259, 2016.

[30] S. K. Yuvaraja and S. Tale, "Pilot contamination evolved scale linearity for investigating the impact of inter-user resistivity in massive MIMO with non-ideal hardware," in *Proc. IEEE Int. Conf. Recent Trends Electron., Info. Commun. Technol. (RTEICT)*, 2016.

[31] J. Proakis and M. Salehi, *Digital Communications*, 5th ed. McGraw-Hill, 2008.

[32] M. K. Simon and M.-S. Alouini., *Digital Communication Over Fading Channels*. John Wiley & Sons, 2000.

[33] H. Schulze and C. Lüders, *Theory and Applications of OFDM and CDMA: Wideband Wireless Communications*. John Wiley & Sons, 2005.

[34] P. Weitkemper, J. Bazzi, K. Kusume, A. Benjebbour, and Y. Kishiyama, "Adaptive filtered OFDM with regular resource grid," in *Proc. IEEE Int. Conf. on Commun. Workshop. (ICC)*, 2016.

[35] A. Tom, A. ahin, and H. Arslan, "Suppressing alignment: An approach for out-of-band interference reduction in OFDM systems," in *Proc. IEEE Int. Conf. Commun. (ICC)*, 2015.

[36] R. W. Bauml, R. F. H. Fischer, and J. B. Huber, "Reducing the peak-to-average power ratio of multicarrier modulation by selected mapping," *Elect. Lett.*, vol. 32, no. 22, pp. 2056–2057, 1996.

[37] L. J. Cimini and N. R. Sollenberger, "Peak-to-average power ratio reduction of an OFDM signal using partial transmit sequences," *IEEE Commun. Lett.*, vol. 4, no. 3, pp. 86–88, 2000.

[38] J. Urban and R. Marsalek, "OFDM PAPR reduction by combination of Interleaving with repeated clipping and filtering," in *Proc. 14th Int. Workshop Syst., Signal Image Process. and 6th EURASIP Conf. focused Speech Image Process., Multimedia Commun. Services*, 2007.

[39] A. Chockalingam and B. S. Rajan, *Large MIMO systems*. Cambridge University Press, 2014.

[40] G. H. Golub and C. F. Van Loan, *Matrix computations*, 4th ed. JHU Press, 2013.

[41] C. E. Shannon, "A mathematical theory of communication," *The Bell Syst. Tech. J.*, vol. 27, no. 4, pp. 623–656, Oct 1948.

[42] W. C. Huffman and V. Pless, *Fundamentals of Error-Correcting Codes*. Cambridge university press, 2010.

[43] V. Pless, *Introduction to the Theory of Error-Correcting Codes*, 3rd ed. John Wiley & Sons, 1998.

[44] A. Glavieux, *Channel Coding in Communication Networks: from Theory to Turbocodes*. John Wiley & Sons, 2013.

[45] R. H. Morelos-Zaragoza, *The Art of Error Correcting Coding*. John Wiley & Sons, 2006.

[46] J. Adamek, *Foundations of Coding: Theory and Spplications of Error-Correcting Codes with an Introduction to Cryptography and Information Theory*. John Wiley & Sons, 2011.

[47] S. J. Johnson, *Iterative Error Correction: Turbo, Low-Density Parity-Check and Repeat-Accumulate Codes*. Cambridge University Press, 2009.

[48] P. G. Farrell and J. Moreira, *Essentials of Error-Control Coding*. John Wiley & Sons, 2006.

[49] B. Monica, *Fundamentals in Information Theory and Coding*. Springer, 2011.

[50] K. Moon Todd, *Error Correction Coding, Mathematical Methods and Algorithms*. John Wiley & Sons, Ltd, 2005.

[51] L. Hanzo, T. H. Liew, and B. L. Yeap, *Turbo Coding, Turbo Equalisation and Space-Time Coding*. John Wiley & Sons, 2002.

[52] R. A. Carrasco and M. Johnston, *Non-Binary Error Control Coding for Wireless Communication and Data Storage*. John Wiley & Sons, 2008.

[53] J. Erfanian, S. Pasupathy, and G. Gulak, "Reduced complexity symbol detectors with parallel structure for ISI channels," *IEEE Trans. Commun.*, vol. 42, no. 234, pp. 1661–1671, 1994.

[54] N. Görtz, "A generalised framework for iterative source-channel decoding," in *Turbo Codes: Error-correcting Codes of Widening Application*, R. Pyndiah and M. Jezequel, Eds. Kogan Page Science, 2002.

[55] T. M. Duman and A. Ghrayeb, *Coding for MIMO Communication Systems*. Wiley Online Library, 2007.

[56] V. Tarokh, *New Directions in Wireless Communications Research*. Springer, 2009.

[57] R. Gallager, "Low-density parity-check codes," *IEEE Trans. Inf. Theory*, vol. 8, no. 1, pp. 21–28, 1962.

[58] R. Tanner, "A recursive approach to low complexity codes," *IEEE Trans. Inf. Theory*, vol. 27, no. 5, pp. 533–547, 1981.

[59] D. J. MacKay and R. M. Neal, "Good codes based on very sparse matrices," in *Proc. IMA Int. Conf. Crypto. Cod.* Springer, 1995.

[60] X. Zhao, Y. Li, J. Zhong, M. Zhao, and C. Zheng, "Low-complexity layered joint detection and decoding for LDPC coded large-MIMO systems," in *Proc. Int. Conf. Wireless Commun. Signal Process. (WCSP),*, Oct 2013.

[61] K. Wang, H. Shen, W. Wu, and Z. Ding, "Joint Detection and Decoding in LDPC-Based Space-Time Coded MIMO-OFDM Systems via Linear Programming," *IEEE Trans. Signal Process.*, vol. 63, no. 13, pp. 3411–3424, July 2015.

[62] S. ten Brink, G. Kramer, and A. Ashikhmin, "Design of low-density parity-check codes for modulation and detection," *IEEE Trans. Commun.*, vol. 52, no. 4, pp. 670–678, April 2004.

[63] P. Suthisopapan, K. Kasai, V. Imtawil, and A. Meesomboon, "Approaching capacity of large MIMO systems by non-binary LDPC codes and MMSE detection," in *Proc. IEEE Int. Sympo. Inf. Theory (ISIT),*, July 2012.

[64] J. Zhou, Y. Ye, and J. Hu, "Biased MMSE soft-output detection based on Jacobi method in massive MIMO," in *Proc. IEEE Int. Conf. Commun. Problem-Solving (ICCP),*, Dec 2014.

[65] S. Barbarossa, *Multiantenna Wireless Communications Systems*. Artech House Publishers, 2005.

[66] G. Stewart, *Matrix Algorithms: Volume 1, Basic Decompositions*, 1st ed. Cambridge University Press, 1998.

[67] M. Wu, B. Yin, G. Wang, C. Dick, J. Cavallaro, and C. Studer, "Large-Scale MIMO Detection for 3GPP LTE: Algorithms and FPGA Implementations," *IEEE J. Sel. Topics Signal Process.*, vol. 8, no. 5, pp. 916–929, Oct 2014.

[68] A. Al-Askery, C. C. Tsimenidis, S. Boussakta, and J. A. Chambers, "Improved coded massive MIMO OFDM detection using LLRs derived from complex ratio distributions," in *Proc. IEEE 20th Int. Workshop Comput. -Aided Modelling. Design of commun. Links Netw. (CAMAD)*, Sep. 2015.

[69] E. W. M. Coladarci Theodore, Casey D. Cobb and R. C. Clarke, *Fundamentals of Statistical Reasoning in Education*. John Wiley & Sons, 2010.

[70] M. Chiani, D. Dardari, and M. K. Simon, "New exponential bounds and approximations for the computation of error probability in fading channels," *IEEE Trans. Wireless Commun.*, vol. 2, no. 4, pp. 840–845, July 2003.

[71] K. Keith, *Mathematical Statistics*. USA: CHAPMAN & HALL/CRC, 2000.

[72] J. J. S. R. A. S. Spiegel, Murray R. and M. LeVan, *Probability and Statistics*. New York, USA: Mcgraw-hill, 2009.

[73] F. A. G. Alexander McFarlane Mood and D. C. Boes, *Introduction to the Theory of Statistics*, 3rd ed. McGraw-Hill, 1974.

[74] A. Papoulis and S. U. Pillai, *Probability, Random Variables, and Stochastic Processes*, 3rd ed. McGraw-Hill Education, 1991.

[75] J. Kiusalaas, *Numerical methods in engineering with Python*, 2nd ed. Cambridge University Press, 2010.

[76] R. L. Burden and J. D. Faires, *Numerical analysis*, 9th ed. Brooks/Cole, USA, 2011.

[77] J. H. Mathews and K. D. Fink, *Numerical methods using MATLAB*, 3rd ed. Prentice hall Upper Saddle River, NJ, 1999.

[78] J. G. Andrews, S. Buzzi, W. Choi, S. V. Hanly, A. Lozano, A. C. K. Soong, and J. C. Zhang, "What Will 5G Be?" *IEEE J. Sel. Areas Commun.*, vol. 32, no. 6, pp. 1065–1082, 2014.

[79] S. Yang and L. Hanzo, "Fifty Years of MIMO Detection: The Road to Large-Scale MIMOs," *IEEE Commun. Surveys Tuts.*, vol. 17, no. 4, pp. 1941–1988, 2015.

[80] A. Elghariani and M. Zoltowski, "Low Complexity Detection Algorithms in Large-Scale MIMO Systems," *IEEE Trans. Wireless Commun.*, vol. 15, no. 3, pp. 1689–1702, 2016.

[81] M. I. Asseri, S. Y. L. Goff, C. C. Tsimenidis, and B. S. Sharif, "Efficient Recovery of dSLM in MIMO-OFDM without Side Information," in *Proc. 5th Adv. Int. Conf. Telecommun. (AICT).*, 2009.

[82] E. Baar, "Multiple-Input Multiple-Output OFDM with Index Modulation," *IEEE Signal Process. Lett.*, vol. 22, no. 12, pp. 2259–2263, 2015.

[83] M. B. Uddin, M. Z. I. Sarkar, K. N. Faisal, and M. M. Ali, "Performance analysis of Nakagami-m fading massive MIMO channels with linear receivers," in *Proc. 17th Int. Conf. Comput. Info. Technol. (ICCIT)*, 2014.

[84] X. Li, S. Zhou, E. Bjrnson, and J. Wang, "Capacity Analysis for Spatially Non-Wide Sense Stationary Uplink Massive MIMO Systems," *IEEE Trans. Wireless Commun.*, vol. 14, no. 12, pp. 7044–7056, 2015.

[85] M. S. Zia and S. A. Hassan, "Outage Analysis of Multi-User Massive MIMO Systems Subject to Composite Fading," in *Proc. IEEE 81st Veh. Technol. Conf. (VTC Spring)*, 2015.

[86] Y. Long, Z. Chen, and J. Fang, "Minimum Number of Antennas Required to Satisfy Outage Probability in Massive MIMO Systems," *IEEE Wireless Commun. Lett.*, vol. PP, no. 99, pp. 1–1, 2016.

[87] C. Roth, S. Belfanti, C. Benkeser, and Q. Huang, "Efficient Parallel Turbo-Decoding for High-Throughput Wireless Systems," *IEEE Trans. Circuits Syst. I*, vol. 61, no. 6, pp. 1824–1835, 2014.

[88] Y. L. Ueng, C. J. Yeh, and C. L. W. M. C. Lin, "Iterative Detection and Decoding for the Near-Capacity Performance of Turbo Coded MIMO Schemes," in *Proc. IEEE 18th Int. Sympo. Personal Indoor Mobile Radio Commun.*, 2007.

[89] N. Mysore and J. Bajcsy, "Union bound based performance evaluation of turbo-coded uplink MIMO systems," in *Proc. IEEE Military commun. Conf. (MILCOM)*, 2005.

[90] L. Boher, M. Helard, and R. Rabineau, "Turbo-Coded MIMO Iterative Receiver with Bit Per Bit Interference Cancellation for M-QAM Gray Mapping Modulation," in *Proc. IEEE 65th Veh. Technol. Conf. (VTC)*, 2007.

[91] Y. L. Ueng and Y. M. Chen, "A Turbo Coded MIMO Scheme for Noncoherent Fast-Fading Channels," in *Proc. IEEE 66th Veh. Technol. Conf. (VTC)*, 2008.

[92] P. Shang, S. Kim, and K. Choi, "Soft ZF MIMO detection for turbo codes," in *Proc. IEEE 6th Int. Conf. Wireless Mobile Comput. Netw. commun. (WiMob)*, 2010.

[93] P. Shang, S. Kim, and K. Choi, "Soft MMSE receiver for turbo coded MIMO system," in *Proc. IEEE 7th Int. Conf. Wireless Mobile Comput. Netw. commun. (WiMob)*, 2011.

[94] K. J. Kim, T. Reid, and R. A. Iltis, "Iterative soft-QRD-M for turbo coded MIMO-OFDM systems," *IEEE Trans. Commun.*, vol. 56, no. 7, pp. 1043–1046, 2008.

[95] A. Viterbi, "Convolutional Codes and Their Performance in Communication Systems," *IEEE Trans. Commun. Technol.*, vol. 19, no. 5, pp. 751–772, October 1971.

[96] J. Conan, "The Weight Spectra of Some Short Low-Rate Convolutional Codes," *IEEE Trans. Commun.*, vol. 32, no. 9, pp. 1050–1053, 1984.

[97] P. Frenger, P. Orten, and T. Ottosson, "Convolutional codes with optimum distance spectrum," *IEEE Commun. Lett.*, vol. 3, no. 11, pp. 317–319, Nov 1999.

[98] H. Moon and D. Cox, "Improved Performance Upper Bounds for Terminated Convolutional Codes," *IEEE Commun. Lett.*, vol. 11, no. 6, pp. 519–521, June 2007.

[99] N. Kim and H. Park, "Bit error performance of convolutional coded MIMO system with linear MMSE receiver," *IEEE Trans. Wireless Commun.*, vol. 8, no. 7, pp. 3420–3424, July 2009.

[100] Y. Huang and J. Ritcey, "Tight BER bounds for iteratively decoded bit-interleaved space-time coded modulation," *IEEE Commun. Lett.*, vol. 8, no. 3, pp. 153–155, March 2004.

[101] M. McKay and I. Collings, "Capacity and performance of MIMO-BICM with zero-forcing receivers," *IEEE Trans. Commun.*, vol. 53, no. 1, pp. 74–83, Jan 2005.

[102] S. Benedetto and G. Montorsi, "Unveiling turbo codes: some results on parallel concatenated coding schemes," *IEEE Trans. Inf. Theory*, vol. 42, no. 2, pp. 409–428, 1996.

[103] S. Benedetto and G. Montorsi, "Performance evaluation of parallel concatenated codes," in *Proc. IEEE Int. Conf. commun. (ICC)*, vol. 2, 1995.

[104] E. Hall and S. Wilson, "Design and analysis of turbo codes on Rayleigh fading channels," *IEEE J. Sel. Areas Commun.*, vol. 16, no. 2, pp. 160–174, 1998.

[105] N. Mysore and J. Bajcsy, "BER bounding techniques for selected turbo coded MIMO systems in Rayleigh fading," in *Proc. 44th Annual Conf. Inf. Sci. Syst. (CISS)*, 2010.

[106] M. Ahmed, C. Tsimenidis, and S. Le Goff, "Performance analysis of full-duplex MIMO-SVD-SIC based relay in the presence of channel estimation errors," in *Proc. IEEE 10th Int. Conf. Wireless Mobile Comput. Netw. commun. (WiMob)*, Oct 2014.

[107] I. Gradshteyn and I. Ryzhik, *Table of Integrals, Series, and Products*, 7th ed. Elsevier, 2007.

[108] V. KUHU, *Wireless communications over MIMO channels*. John Wiley & Sons Ltd, 2006.

[109] K. S. Ahn, R. W. Heath, and H. K. Baik, "Shannon Capacity and Symbol Error Rate of Space-Time Block Codes in MIMO Rayleigh Channels With Channel estimation Error," *IEEE Trans. Wireless Commun.*, vol. 7, no. 1, pp. 324–333, 2008.

[110] J. Janhunen, T. Pitkanen, O. Silven, and M. Juntti, "Fixed- and Floating-Point Processor Comparison for MIMO-OFDM Detector," *IEEE J. Sel. Topics Signal Process.*, vol. 5, no. 8, pp. 1588–1598, Dec 2011.

[111] J. Janhunen, P. Salmela, O. Silven, and M. Juntti, "Fixed- versus floating-point implementation of MIMO-OFDM detector," in *Proc. IEEE Int. Conf. Acoustics, Speech and Signal Process. (ICASSP)*, May 2011.

[112] F. Sobhanmanesh, S. Nooshabadi, and D. Habibi, "A Robust QR-based Detector for V-BLAST and its Efficient Hardware Implementation," in *Proc. Asia-Pacific Conf. Commun.*, Oct 2005.

[113] N. Tax and B. Lankl, "Fixed effort sphere decoder for MIMO OFDM systems," in *Proc. Int. Conf. Wireless Commun. Signal Process. (WCSP)*, Oct 2013.

[114] L. Davis, "Scaled and decoupled Cholesky and QR decompositions with application to spherical MIMO detection," in *Proc. IEEE Wireless Commun. and Network. Conf. (WCNC)*, vol. 1, March 2003.

[115] T. Schmuland and M. Jamali, "Generation of fixed-point VHDL MIMO-OFDM QR pre-processor for Spherical Detectors," in *Proc. IEEE Int. Sympo. Circuits and Systems (ISCAS)*, June 2014.

[116] M. Mehlhose and S. Schiffermüller, "Efficient Fixed-Point Implementation of Linear Equalization for Cooperative MIMO Systems," in *17th European Signal Process. Conf. (EUSIPCO09)*, 2009.

[117] J. Eilert, D. Wu, and D. Liu, "Implementation of a programmable linear MMSE detector for MIMO-OFDM," in *Proc. IEEE Int. Conf. Acoustics, Speech and Signal Process. (ICASSP)*, March 2008.

[118] R. E. Cline, *Elements of the theory of generalized inverses for matrices*. Springer, 1979.

[119] A. Ben-Israel and T. N. Greville, *Generalized Inverses: Theory and Applications*, 2nd ed. Springer Science & Business Media, 2003.

[120] R. Piziak and P. L. Odell, *Matrix Theory: From Generalized Inverses to Jordan Form*. CRC Press, 2007.

[121] J. K. Lim, "Neumann series expansion of the inverse of a frame operator," *Commun. Korean Math. Soc.*, vol. 13, no. 4, pp. 791–800, 1998.

[122] B. Yin, M. Wu, G. Wang, C. Dick, J. Cavallaro, and C. Studer, "A 3.8Gb/s large-scale MIMO detector for 3GPP LTE-Advanced," in *Proc. IEEE Int. Conf. Acoustics, Speech and Signal Process. (ICASSP)*, May 2014.

[123] V. Ingle and J. Proakis, *Digital signal processing using MATLAB*. Cengage Learning, 2011.

[124] M. Mendicute, L. G. Barbero, G. Landaburu, J. S. Thompson, J. Altuna, and V. Atxa, "Real-time implementation of a sphere decoder-based MIMO wireless system," in *14th European Signal Process. Conf. (EUSIPCO06)*, 2006.